This is to certify that the
thesis entitled

AN ANALYTICAL INVERSE METHOD FOR DETERMINATION OF THICK PLATE MATERIAL PROPERTIES FROM ECHO REDUCTION AND INSERTION LOSS TEST DATA

presented by

MR. GREG J. GARTLAND

has been accepted towards fulfillment
of the requirements for the

M.S. degree in **MECHANICAL ENGINEERING**

Clark Radcliffe
Major Professor's Signature

Aug. 10, 2007
Date

APPLICATION OF AN INVERSE MEHTOD FOR DETERMINATION OF ELASTOMERIC MATERIAL PROPERTIES FROM ACOUSTICAL TEST DATA

By

Greg J. Gartland

A THESIS

Submitted to
Michigan State University
in partial fulfillment of the requirements
for the degree of

MASTER OF SCIENCE

Department of Mechanical Engineering

2007

ABSTRACT

APPLICATION OF AN INVERSE MEHTOD FOR DETERMINATION OF ELASTOMERIC MATERIAL PROPERTIES FROM ACOUSTICAL TEST DATA

By

Greg J. Gartland

The work described in this study develops an inverse method designed to obtain the complex dilatational and complex shear wavespeeds of a material from physical test data. The inverse method is devised from a recently established forward model that explicitly predicts the echo reduction and insertion loss of a material at any wavenumber and frequency given the correct material properties. The forward model has closed-form equations that completely describe the system physics of a submerged material. The inverse method incorporates this model and physical test data into a Newton-Raphson iteration to obtain the complex dilatational and complex shear wavespeeds of a material. The complex wavespeeds are then used to obtain the material Lamé constants. The inverse method developed provides the critical link needed between the test data and analytical modeling.

To my beautiful wife Michelle

ACKNOWLEDGMENTS

There are many people who helped me throughout these last two years. They provided me guidance, encouragement, and most of all never-ending support. Their help made a sometimes seemingly insurmountable goal become a reality. I would like to thank all of them for making these two years of my education enjoyable and rewarding.

First, I would like to thank my academic advisor Dr. Clark Radcliffe and naval mentor Dr. Andrew Hull, for their advice and guidance throughout my graduate work. They were responsible for initiating this work and their vast knowledge accelerated my understanding of the subject. They were always there to answer my questions and made the entire experience more fulfilling. I would also like to specifically thank Dr. Hull for introducing me to the beauty of the Appalachian Mountains and to my new favorite activity; hiking.

Second, I would like to thank my family, for always providing their guidance and encouragement to never give up. Anytime, I needed words of advice, they were always there for me. They would motivate me when things were going wrong, and keep me focused when things were going right. Knowing they were always behind me gave me the confidence to keep going forward.

Finally, I would like to thank my wife Michelle, for her support and understanding through a sometimes stressful two years. She never doubted my abilities even when I questioned them myself. Her constant reassurance was the driving force that kept me going. She has been more than understanding, and has made many sacrifices so I could finish my degree, and for that I am forever grateful.

TABLE OF CONTENTS

LIST OF TABLES

LIST OF FIGURES

INTRODUCTION

Analytical acoustic modeling requires accurate material properties to properly predict the acoustical response of a material. Two of these properties are the complex dilatational and complex shear wavespeeds. Accurately obtaining these two wavespeeds allows for the material Lamé constants to be calculated. Material Lamé constants are responsible for, insertion loss, which describes the amount of acoustical energy transmitted through a material, and echo reduction, which describes the amount of acoustical energy reflected back [Hull, A., (2005)]. Physical testing of material insertion loss and echo reduction has been undertaken for many years and is well understood. However, there is currently not an effective method to acquire the material Lamé constants from this physical test data.

Previous work has been done to estimate the complex material wavespeeds using phase change data and insertion loss tests. These methods utilize four parameters in a least squares analysis to fit a casual theoretical model to phase change and insertion loss data. However, the model used is based on the attenuation affects of the material, and not on a complete physical representation of the system [Piquette, J., (2003); Piquette, J., (2004)]. Recently, a model that completely describes the system physics of a submerged material has been developed [Hull, A., (2005)]. The model has closed-form equations that explicitly predict the echo reduction and insertion loss at any wavenumber and frequency given the correct material properties. Therefore, a reverse estimation based on this model will provide a more accurate representation of the complex dilatational and complex shear wavespeeds of a material. The inverse method developed in this paper provides that reverse estimation, and is the essential link needed between the physical test data and the complex wavespeeds of a material.

The inverse method developed requires insertion loss and echo reduction test data to determine the complex dilatational and complex shear wavespeeds. The test data used in this work was obtained from the United States Naval Undersea Warfare Center (NUWC) Acoustical Test Facility (ATF) located in Newport, RI as shown in Figure 1 [Acoustic Test Facility, (2004)].

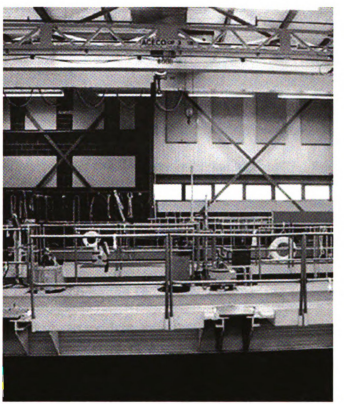

Figure (1) Acoustic Test Facility (Newport, RI); [ATF 2004]

The tests are completed by submerging a thick plate in water and subjecting it to acoustical excitation by means of an incident sound pulse. The resulting reflected and transmitted pulses along with the incident pulse are then used to calculate the echo reduction and insertion loss of the material. The inverse method then compares this test data to the closed-form model that represents the system. A Newton-Raphson iteration is utilized to adjust the complex wavespeeds until the predicted model response matches the test data. When the two match, the complex dilatational and complex shear wavespeeds of the material are known. The

Newton-Raphson iteration can be incorporated into the inverse method because of the closed-form equations produced by the forward model. These equations allow for the calculation of partial derivatives that are required for the inverse method.

The inverse method was first developed for broadside excitation, which reduces the equations and simplifies the analysis. The broadside version was numerically tested with constant parameters to ensure the inverse method produced accurate results. Either the insertion loss or echo reduction equation can be used to determine the complex dilatational wavespeed. Employing the echo reduction equation, the broadside version was then applied to two separate data sets that were obtained from two different materials at the ATF. The complex dilatational wavespeed was calculated for both materials using the developed method and then verified at specific frequencies using wavelength and wavespeed relationships [Miklowitz, J., (1984)].

To acquire the Lamé constants both the complex dilatational and complex shear wavespeeds are required. For this reason, an incident angle was included into the inverse method to allow for the determination of the complex shear wavespeed. The incident angle version requires both the echo reduction and insertion loss equations to be used simultaneously in the calculation of the complex wavespeeds. Unfortunately, the two materials tested in the ATF were acoustically transparent resulting in low magnitude insertion loss data. The resolution of the measurements was equivalent to the insertion loss change and therefore did not produce precise enough results. As both echo reduction and insertion loss data are needed, the incident method could only be numerically tested. However, the numerical tests have shown to accurately estimate the dilatational and shear wavespeeds used to create the insertion loss and echo reduction numerical data. From the numerical wavespeeds, determination of the Lamé constants was demonstrated.

A mechanical shaking device to excite the materials at a lower frequency was also developed at Michigan State University. There were two test setups designed into the device as seen in Figure 2.

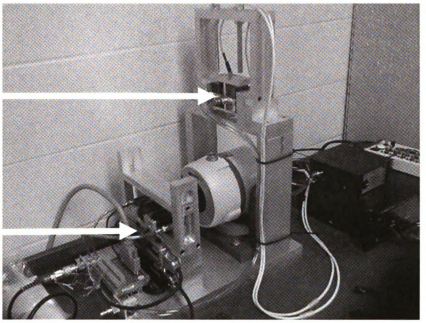

Figure (2) Mechanical Test to Excite Dilatational and Shear Waves

The first test excites the material horizontally, producing a shear response in the material. This test utilizes optical encoders to effectively measure the shear response. The second test excites the material vertically, producing a dilatational response in the material. This test utilizes laser distance sensors to effectively measure the dilatational response. In addition, supporting software to acquire the needed data from these tests has also been developed. The data taken from these tests was used to calculate the dilatational and shear wavespeeds at lower frequencies using a previously developed method [Hull, A., (2003)]. The results were then compared to the results obtained from the high frequency acoustic tests.

SYSTEM MODEL

The system model has been previously developed and is defined as a two-dimensional, infinitely long, thick plate with fluid contact on both sides [Hull, A., (2005)]. The coordinates of the plate are defined as z (m) normal to the plate, and x (m) along the length as shown in Figure 3.

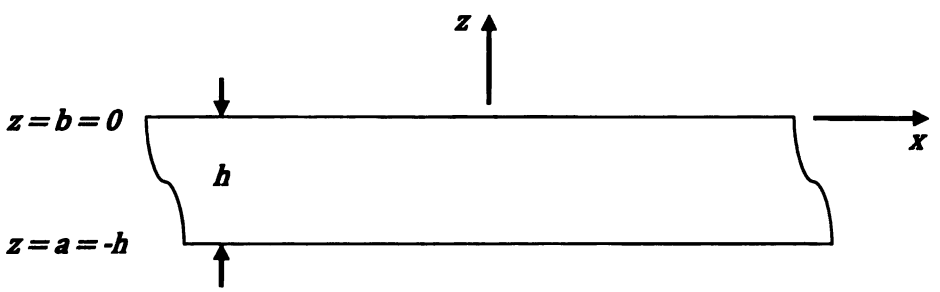

Figure (3) Coordinate System of Thick Plate

The excitation side of the plate is defined to be $z = b = 0$, and the opposite side of the plate is defined as $z = a = -h$ with h being the thickness. The movement of the plate is governed by,

$$\mu\nabla^2\boldsymbol{u} + (\lambda + \mu)\nabla\nabla \bullet \boldsymbol{u} = \rho\frac{\partial^2\boldsymbol{u}}{\partial t^2} \tag{1}$$

where the density of the plate is defined as ρ (kg/m^3), $\mathbf{u}$ is the Cartesian coordinate displacement vector, $\bullet$ denotes a vector dot product, ∇ represents a Laplace operator, and λ and μ (N/m^2) are the Lamé constants. The Lamé constants are material properties that can be related to the Young's modulus (E), Shear modulus (G) and Poisson's Ratio (ν) as [Hull, A., (2005)],

$$\lambda = \frac{E\nu}{(1+\nu)(1-2\nu)} \tag{2a}$$

and

$$\mu = G = \frac{E}{2(1+\nu)} \tag{2b}$$

The Lame constants can also be related to the complex dilatational wavespeed as,

$$c_d = \sqrt{\frac{\lambda + 2\mu}{\rho}} \tag{3a}$$

and complex shear wavespeed as [Hull, A., (2005)],

$$c_s = \sqrt{\frac{\mu}{\rho}} \tag{3b}$$

The fluid provides continuous pressure on the plate and the excitation on the plate is assumed to be a plane wave. The fluid is assumed to have the same acoustic properties on each side of the plate and exhibit no spreading loss. The fluid on both sides is governed in Cartesian coordinates by the wave equation [Hull, A., (2005)]

$$\frac{\partial^2 p_{1,2}(x,z,t)}{\partial z^2} + \frac{\partial^2 p_{1,2}(x,z,t)}{\partial x^2} - \frac{1}{c_f^2}\frac{\partial^2 p_{1,2}(x,z,t)}{\partial t^2} = 0 \tag{4}$$

where $p(x,z,t)$ is the pressure (N/m^2), with subscript 1 and 2 representing the acoustic pressure on the excitation and opposite the excitation sides of the plate respectively. The compressional wavespeed of the fluid is defined as c_f (m/s), and t is time (s). Both boundaries of the plate with the fluid are governed by linear momentum [Hull, A., (2005)]

$$\rho_f \frac{\partial^2 u_z(x,b,t)}{\partial t^2} = -\frac{\partial p_1(x,b,t)}{\partial z} \tag{5}$$

on the excitation side of the plate where $z = b = 0$, and

$$\rho_f \frac{\partial^2 u_z(x,a,t)}{\partial t^2} = -\frac{\partial p_1(x,a,t)}{\partial z} \tag{6}$$

opposite the excitation side where $z = a = -h$. In equations (5) and (6) ρ_f is the density (kg/m^3) of the fluid. Utilizing equations (1), (4), (5), and (6) an equation that explicitly predicts the echo reduction and insertion loss behavior of the plate at any frequency or wavenumber has been

previously developed. Provided the correct material properties, equations (1), (4), (5), and (6) predict the echo reduction [Hull, A., (2005)]

$$ER(k_x,\omega) = \frac{\Delta_d}{\phi_d} \tag{7}$$

with numerator,

$$\begin{aligned}\Delta_d = {} & 8\alpha\beta k_x^2(\beta^2 - k_x^2)^2[1 - cos(\alpha h)\, cos(\beta h)] + \\ & 2i\rho_f(\gamma\rho)^{-1}\alpha(\beta^2 - k_x^2)^2(\beta^2 + k_x^2)^2\, cos(\alpha h)\, sin(\beta h) + \\ & 8i\rho_f(\gamma\rho)^{-1}\alpha^2\beta k_x^2(\beta^2 + k_x^2)^2\, sin(\alpha h)\, cos(\beta h) + \\ & \left[(\beta^2 - k_x^2)^4 + 16\alpha^2\beta^2 k_x^4 + \rho_f^2(\gamma\rho)^{-2}\alpha^2(\beta^2 + k_x^2)^4\right] sin(\alpha h)\, sin(\beta h)\end{aligned} \tag{8}$$

and echo reduction denominator

$$\begin{aligned}\phi_d = {} & 8\alpha\beta k_x^2(\beta^2 - k_x^2)^2[1 - cos(\alpha h)\, cos(\beta h)] + \\ & \left[(\beta^2 - k_x^2)^4 + 16\alpha^2\beta^2 k_x^4 - \rho_f^2(\gamma\rho)^{-2}\alpha^2(\beta^2 + k_x^2)^4\right] sin(\alpha h)\, sin(\beta h)\end{aligned} \tag{9}$$

Equations (1), (4), (5), and (6) predict the insertion loss [Hull, A., (2005)],

$$IL(k_x,\omega) = \frac{\Delta_d}{\psi_d} \tag{10}$$

with insertion loss denominator,

$$\begin{aligned}\psi_d = {} & 2i\rho_f(\gamma\rho)^{-1}\alpha(\beta^2 - k_x^2)^2(\beta^2 + k_x^2)^2\, sin(\beta h) + \\ & 8i\rho_f(\gamma\rho)^{-1}\alpha^2\beta k_x^2(\beta^2 + k_x^2)^2\, sin(\alpha h)\end{aligned} \tag{11}$$

In equations (8), (9) and (11), $i = \sqrt{-1}$, and the modified compressional wave propagation constant of the fluid,

$$\gamma = \sqrt{\left(\frac{\omega}{c_f}\right)^2 - k_x^2} \tag{12}$$

In equations (8), (9) and (11), the modified dilatational wave propagation constant of the plate,

$$\alpha = \sqrt{k_d^2 - k_x^2} \tag{13}$$

where k_x is the spatial wavenumber in the x-direction (rad/m) and the dilatational wavenumber

$$k_d = \frac{\omega}{c_d} \tag{14}$$

where ω is the frequency of the incident wave (rad/s). The wavespeed c_d (m/s) is a function of the material Lamé constants as seen in equation (3a). In equations (8), (9) and (11), the modified shear wave propagation constant of the plate

$$\beta = \sqrt{k_s^2 - k_x^2} \tag{15}$$

with the shear wavenumber,

$$k_s = \frac{\omega}{c_s} \tag{16}$$

The wavespeed c_s (m/s), is a function of the material Lamé constants as seen in equation (3b). The spatial wavenumber (k_x) is dependent on the incoming incident angle (θ) of the sound wave and is determined through geometrical relationships between the plate and the incoming sound wave as seen in Figure 4.

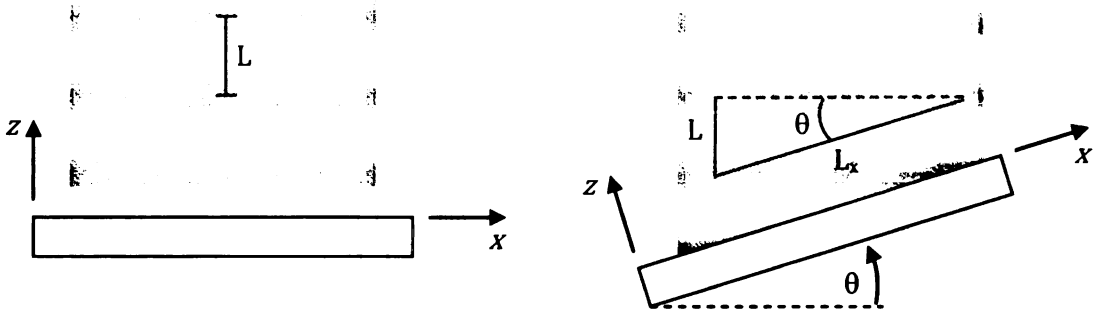

Figure (4) Broadside and Angled Incoming Incident Wave

The wavenumber for a plane wave,

$$k = \frac{2\pi}{L} \tag{17}$$

where L is the wavelength (m). Wave frequency and wavespeed of the fluid are used to determine the wavelength,

$$L = \frac{c_f}{f} = \frac{2\pi c_f}{\omega} \tag{18}$$

The wavenumber in the x direction,

$$k_x = \frac{2\pi}{L_x} \tag{19}$$

where L_x (m) is the length of the wave in the x direction and is calculated using trigonometric identities of the incidence angle (θ) as,

$$L_x = \frac{L}{\sin\theta} \tag{20}$$

Substituting this into the wavenumber equation (19) results in,

$$k_x = \frac{2\pi}{L}\sin\theta \tag{21}$$

and replacing L with its definition from equation (18) results in,

$$k_x = \frac{\omega}{c_f}\sin\theta \tag{22}$$

ACOUSTICAL TEST SETUP

The echo reduction and insertion loss tests were done in Newport, RI at the Naval Undersea Warfare Center's Acoustic Test Facility. It is the world's largest acoustic tank with a modern electronic support system, holding approximately 625,000 gallons of water. The tests were performed on two elastomeric materials, 3140 and EN-6 using a setup that is shown in Figure 5.

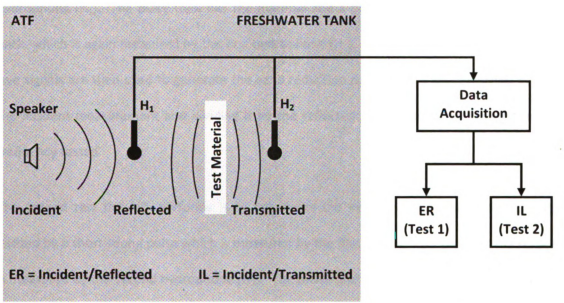

Figure (5) Diagram of Acoustic Test Facility Set-up and Measurements

Both materials were 30 inches by 30 inches, and were 1 inch thick. The ATF produced echo reduction and insertion loss measurements from 25 kHz to 100 kHz in 250 Hz intervals. The two tests were repeated with the plate angle varying from 0 degrees (broadside) to 20 degrees in 5 degree increments. The speaker was positioned 99.2 inches away from the material resulting in an approximate plane wave at the material surface, coinciding with the system model. The first hydrophone was located 69.5 inches from the speaker and 29.7 inches from the thick plate, and the second hydrophone was placed 2.2 inches behind the plate. To account for the spreading loss between the plate and the hydrophones, the ATF adds a correction factor into the data. The correction factor used is for spherical spreading loss, and adjusts the magnitude of the

response to correct for energy loss as the wave expands [Sonar Propagation, (1998)]. This correction was left in the data as the model used assumed plane waves and therefore no loss associated with distance.

The first test determines the echo reduction and is completed by sending a short sound pulse at a specified frequency from the speaker towards the material, which is measured by the first hydrophone (H_1). The pulse then hits the material and a portion of the sound energy reflects back, which is again measured by the first hydrophone (H_1). The phase and magnitude of these two signals are then used to generate the echo reduction data. This is accomplished by taking the incident measurement and dividing it by the reflected. The process is repeated for each frequency tested.

The second test the ATF performs is to determine the insertion loss. The material is again excited by a short sound pulse which is measured by the first hydrophone (H_1), but the response is measured by the second hydrophone (H_2). The phase and magnitude of these two signals are then used to generate the insertion loss data by taking the incident measurement and dividing it by the transmitted one.

MECHANICAL TEST SETUP

A mechanical excitation device was designed and built to provide low frequency mechanical data to compare to the high frequency acoustical data [Appendix A]. There are two test setups designed into the device, as seen in Figures 6 and 7.

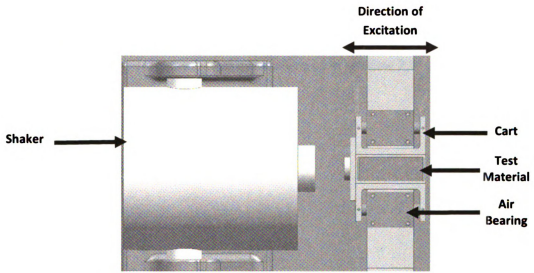

Figure (6) Horizontal Mechanical Test to Excite Shear Response

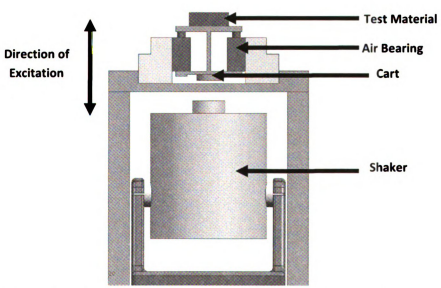

Figure (7) Vertical Mechanical Test to Excite Dilatational Response

The first test excites the material horizontally, producing a shear response in the material. This test utilizes Renishaw RGF0100H125A optical encoders which have a resolution of 0.2μm. The second test excites the material vertically, producing a dilatational response in the material. This test utilizes Baumer Electric OADM 12U6430/S35A laser distance sensors which have a resolution of 4μm. Both these tests use NewWay S301201 commercial air bearings to reduce noise in the system and are excited with a LDS 400 series shaker. The supporting software to acquire the needed data from these tests was developed in LabView 7.1.

INVERSE METHOD

Examination of the echo reduction and insertion loss equations (7) and (10) reveals that they are a function of the modified wave propagation constants described in equations (13) and (15). Therefore, the inverse method was designed to obtain those modified wave propagation constants and use them to calculate the complex dilatational and complex shear wavespeed as

$$c_d = \sqrt{\frac{\omega^2}{\alpha^2 + k_x^2}} \tag{23a}$$

and

$$c_s = \sqrt{\frac{\omega^2}{\beta^2 + k_x^2}} \tag{23b}$$

respectfully. The material Lamé constants are then determined as,

$$\mu = \rho c_s^2 \tag{24a}$$

and

$$\lambda = \rho\left(c_d^2 - 2c_s^2\right) \tag{24b}$$

Poisson's Ratio is then defined in terms of the Lamé constants as,

$$\nu = \frac{\lambda}{2(\mu + \lambda)} \tag{25}$$

The inverse method relies on a Newton-Raphson iteration to calculate these modified wave propagation constants. Two different methods were developed, first a broadside version that simplified the analysis, but only solved for the modified dilatational wave propagation constant. The second version incorporated an incident angle into the calculation allowing for both the modified dilatational and modified shear wave propagation constants to be calculated.

The approach for the inverse method, shown in Figure 8, is the same for both the broadside and incident angle versions. Initial values for the modified wave propagation constants are inserted

into the program, which uses them and the previously developed forward model to predict echo reduction and insertion loss responses. These responses are then compared to the test data received from the ATF and the difference is calculated.

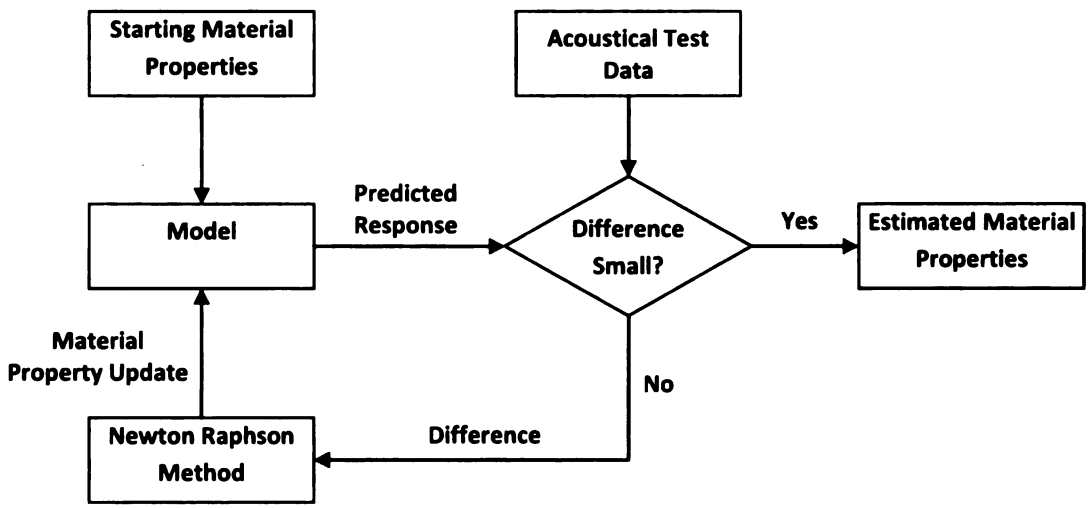

Figure (8) Flow Chart for Inverse Method

If the differences between the predicted responses and the data are zero, the two modified wave propagation constants are correct; if not the initial values are updated through the Newton-Raphson method. The Newton Raphson method utilizes partial derivatives of the echo reduction and insertion loss equations to adjust the modified wave propagation constants. The updated modified wave propagation constants are used to generate another predicted response that is again compared to the test data. The loop repeats itself until the difference is reduced below a set parameter. The acquired modified wave propagation constants are then used as the initial guess at the next frequency. This process continues until the modified wave propagation constants have been determined at all frequencies tested.

Broadside

The broadside version of the inverse method assumes broadside excitation with $\theta = 0$. Applying that assumption to equation (22) results in a spatial wavenumber in the x-direction of zero. Inserting this outcome into equations (7) and (10) results in the broadside echo reduction equation

$$ER^B = \frac{2i\,\rho_f(\gamma\rho)^{-1}\alpha cos(\alpha h) + \left[1 + \rho_f^2(\gamma\rho)^{-2}\alpha^2\right]\sin(\alpha h)}{\left[1 - \rho_f^2(\gamma\rho)^{-2}\alpha^2\right]\sin(\alpha h)} \tag{26}$$

and the broadside insertion loss equation

$$IL^B = \frac{2i\,\rho_f(\gamma\rho)^{-1}\alpha cos(\alpha h) + \left[1 + \rho_f^2(\gamma\rho)^{-2}\alpha^2\right]\sin(\alpha h)}{2i\rho_f(\gamma\rho)^{-1}\alpha} \tag{27}$$

where the superscript B represents broadside. The modified shear wave propagation constants are eliminated out of both equations, allowing for only the modified dilatational wave propagation constant to be solved for. Physically, broadside excitation is representative of there being no shear wave excitation in the plate, supporting the elimination of the shear terms.

Either the broadside echo reduction or broadside insertion loss equation can be utilized to solve for the modified dilatational wave propagation constant. Below the broadside echo reduction equation was chosen to demonstrate the development of the method. The same technique can be used with the broadside insertion loss equation [Appendix B]. To permit both the real and imaginary parts to be acquired, the modified dilatational wave propagation constant was split into real and imaginary parts as,

$$\alpha = \alpha_R + i\alpha_I \tag{28}$$

where α_R is the real part of the modified dilatational wave propagation constant, and α_I is the imaginary part of the modified dilatational wave propagation constant. Substituting equation

(28) into the broadside echo reduction equation (26) and utilizing the complex trigonometric identities [Potter, M., Goldberg, J., (1995)],

$$\sin(h\alpha_R + ih\alpha_I) = \sin(h\alpha_R)\cosh(h\alpha_I) + i\cos(h\alpha_R)\sinh(h\alpha_I) \tag{29a}$$

and

$$\cos(h\alpha_R + ih\alpha_I) = \cos(h\alpha_R)\cosh(h\alpha_I) - i\sin(h\alpha_R)\sinh(h\alpha_I) \tag{29b}$$

resulted in the complex broadside echo reduction equation,

$$ER^B = \frac{2ip_1(\alpha_R + i\alpha_I)\cos(h\alpha_R)\cosh(h\alpha_I) - i\sin(h\alpha_R)\sinh(h\alpha_I)}{[1 - p_2(\alpha_R + i\alpha_I)^2]\sin(h\alpha_R)\cosh(h\alpha_I) + i\cos(h\alpha_R)\sinh(h\alpha_I)} + \frac{[1 + p_2(\alpha_R + i\alpha_I)^2]\sin(h\alpha_R)\cosh(h\alpha_I) + i\cos(h\alpha_R)\sinh(h\alpha_I)}{[1 - p_2(\alpha_R + i\alpha_I)^2]\sin(h\alpha_R)\cosh(h\alpha_I) + i\cos(h\alpha_R)\sinh(h\alpha_I)} \tag{30}$$

with intermediate variables

$$p_1 = \rho_f(\gamma\rho)^{-1} \tag{31a}$$

and

$$p_2 = \rho_f^2(\gamma\rho)^{-2} \tag{31b}$$

Splitting equation (30) into real and imaginary parts resulted in the split broadside echo reduction equation,

$$ER^B = \frac{ER_R^{BN} + iER_I^{BN}}{ER_R^{BD} + iER_I^{BD}} \tag{32}$$

where the N, D superscripts and the R, I subscripts represent numerator, denominator, real, and imaginary respectively. The split broadside echo reduction numerator consisted of the real part,

$$ER_R^{BN} = [2p_1\alpha_R\sin(h\alpha_R)\sinh(h\alpha_I) - 2p_1\alpha_I\cos(h\alpha_R)\cosh(h\alpha_I)] + [(1 + p_2\alpha_R^2 - P_2\alpha_I^2)\sin(h\alpha_R)\cosh(h\alpha_I) - 2p_2\alpha_R\alpha_I\cos(h\alpha_R)\sinh(h\alpha_I)] \tag{33}$$

and the imaginary part,

$$ER_I^{BN} = [2p_1\alpha_R \cos(h\alpha_R)\cosh(h\alpha_I) + 2p_1\alpha_I \sin(h\alpha_R)\sinh(h\alpha_I)] + [(1 + p_2\alpha_R^2 - p_2\alpha_I^2)\cos(h\alpha_R)\sinh(h\alpha_I) + 2p_2\alpha_R\alpha_I \sin(h\alpha_R)\cosh(h\alpha_I)] \quad (34)$$

The split broadside echo reduction denominator consisted of the real part,

$$ER_R^{BD} = [(1 - p_2\alpha_R^2 + p_2\alpha_I^2)\sin(h\alpha_R)\cosh(h\alpha_I) + 2p_2\alpha_R\alpha_I \cos(h\alpha_R)\sinh(h\alpha_I)] \quad (35)$$

and the imaginary part,

$$ER_I^{BD} = [(1 - p_2\alpha_R^2 + p_2\alpha_I^2)\cos(h\alpha_R)\sinh(h\alpha_I) - 2p_2\alpha_R\alpha_I \sin(h\alpha_R)\cosh(h\alpha_I)] \quad (36)$$

Having the numerator and denominator of the split broadside echo equation (32) allows for the separation of the real and imaginary parts as,

$$ER^B = ER_R^B + iER_I^B \quad (37)$$

with the real part being

$$ER_R^B = \frac{(ER_R^{BN})(ER_R^{BD}) + (ER_I^{BN})(ER_I^{BD})}{(ER_R^{BD})^2 + (ER_I^{BD})^2} \quad (38)$$

and the imaginary part being

$$ER_I^B = \frac{(ER_I^{BN})(ER_R^{BD}) - (ER_R^{BN})(ER_I^{BD})}{(ER_R^{BD})^2 + (ER_I^{BD})^2} \quad (39)$$

The split echo reduction equation resulted in two iteration points that were used to solve for both the real and imaginary part of the modified dilatational wave propagation constant. The partial derivatives of the real and imaginary parts of the echo reduction with respect to both the real and imaginary parts of the modified dilatational wave propagation constant were then determined and utilized by the Newton Raphson method [Appendix C].

$$\begin{Bmatrix}\alpha_R \\ \alpha_I\end{Bmatrix}_{j+1} = \begin{Bmatrix}\alpha_R \\ \alpha_I\end{Bmatrix}_j - \begin{bmatrix}\frac{\partial ER_R^B}{\partial \alpha_R} & \frac{\partial ER_R^B}{\partial \alpha_I} \\ \frac{\partial ER_I^B}{\partial \alpha_R} & \frac{\partial ER_I^B}{\partial \alpha_I}\end{bmatrix}_j \begin{Bmatrix}M_{ER_R^B} - D_{ER_R^B} \\ M_{ER_I^B} - D_{ER_I^B}\end{Bmatrix}_j \quad (40)$$

where M represents the model prediction with the current α_R and α_I parameters, D represents the test data, and j is the iteration number. Once all of the modified dilatational wave propagation constants are solved for, the complex dilatational wavespeed is determined using equation (23a).

Incident Angle

To acquire the Lamé constants both the complex dilatational and complex shear wavespeeds need to be calculated. For this reason, an incident angle was included into the calculations to allow for the determination of the complex shear wavespeed. The new method requires both the echo reduction and insertion loss equations to be used simultaneously in the calculation of the complex wavespeeds.

Incorporating an incident angle into the inverse method eliminates the simplification utilized in the broadside case. Shear waves are now excited, and along with the modified dilatational wave propagation constant, the spatial wavenumber in the x-direction and the modified shear wave propagation constant must also be accounted for. To acquire both parts of the complex modified shear wave propagation constant, it was split as,

$$\beta = \beta_R + i\beta_I \tag{41}$$

Solving for both parts of the complex modified wave propagation constants required the simultaneous utilization of insertion loss and echo reduction data. To achieve this, the full echo reduction and insertion loss equations were split into real and imaginary parts as [Appendix D],

$$ER = ER_R + iER_I \tag{42}$$

and

$$IL = IL_R + iIL_I \tag{43}$$

The Newton-Raphson method was then expanded to incorporate both real and imaginary parts of the complex modified wave propagation constants into the iteration as,

$$\begin{Bmatrix} \alpha_R \\ \alpha_I \\ \beta_R \\ \beta_I \end{Bmatrix}_{j+1} = \begin{Bmatrix} \alpha_R \\ \alpha_I \\ \beta_R \\ \beta_I \end{Bmatrix}_j - \begin{bmatrix} \frac{\partial ER_R}{\partial \alpha_R} & \frac{\partial ER_R}{\partial \alpha_I} & \frac{\partial ER_R}{\partial \beta_R} & \frac{\partial ER_R}{\partial \beta_I} \\ \frac{\partial ER_I}{\partial \alpha_R} & \frac{\partial ER_I}{\partial \alpha_I} & \frac{\partial ER_I}{\partial \beta_R} & \frac{\partial ER_I}{\partial \beta_I} \\ \frac{\partial IL_R}{\partial \alpha_R} & \frac{\partial IL_R}{\partial \alpha_I} & \frac{\partial IL_R}{\partial \beta_R} & \frac{\partial IL_R}{\partial \beta_I} \\ \frac{\partial IL_I}{\partial \alpha_R} & \frac{\partial IL_I}{\partial \alpha_I} & \frac{\partial IL_I}{\partial \beta_R} & \frac{\partial IL_I}{\partial \beta_I} \end{bmatrix}_j \begin{Bmatrix} M_{ER_R} - D_{ER_R} \\ M_{ER_I} - D_{ER_I} \\ M_{IL_R} - D_{IL_R} \\ M_{IL_I} - D_{IL_I} \end{Bmatrix}_j \tag{44}$$

where M_{ER} and M_{IL} represent the echo reduction and insertion loss model predictions with the current parameters respectively, D_{ER} and D_{IL} represents the echo reduction and insertion loss test data respectively, and j is the iteration number. Once the complex modified dilatational and complex modified shear wave propagation constants are known the complex dilatational and complex shear wavespeeds can be calculated from equations (23a) and (23b) and the Lamé constants from equations (24a) and (24b).

NUMERICAL TESTING

Numerically testing both the broadside version and the incident angle version of the inverse method was a necessary step in ensuring the correct material properties could be acquired. The numerical tests generated echo reduction and insertion loss data using constant wavespeed parameters. Although the wavespeeds were constant, the modified dilatational and modified shear wave propagation constants vary with frequency. This variance is important in the numerical testing as the inverse method uses the modified wave propagation constants solved for at the current frequency as the initial guess for the next frequency.

Broadside

The following is a numerical example used to demonstrate the broadside version and also as a verification of the equations previously developed. The example is assumes a material density of 1400 (kg/m^3), material thickness of 0.0381 (m) and a complex dilatational wavespeed defined as,

$$c_d = 1500 + 25i \ (^m/_s) \tag{45}$$

The fluid the material is submerged in was assumed to be fresh water with a density of 1000 (kg/m^3), and a compressional wavespeed of 1467.5 (m/s). The assumed values were then inserted into equation (30) to generate an original echo reduction response as shown in Figure 9. The insertion loss equations can also be used to solve for the complex dilatational wavespeed if insertion loss data is available. [Appendix E].

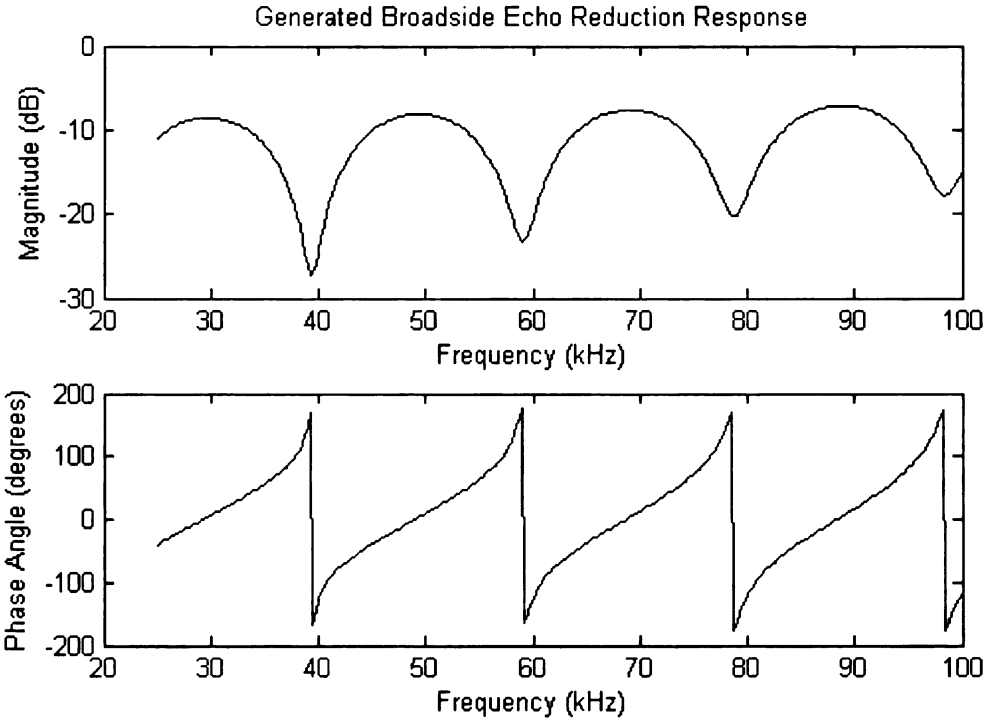

Figure (9) Generated Broadside Echo Reduction Response

The response was then used as the input to the inverse method to estimate the complex dilatational wavespeed. The inverse method recovered the exact complex dilatational wavespeed used to generate the original echo reduction response. The original generated broadside echo reduction and the predicted broadside echo reduction using the calculated complex dilatational wavespeeds are shown in Figure 10, the two graphs match providing evidence that the developed inverse program is running correctly.

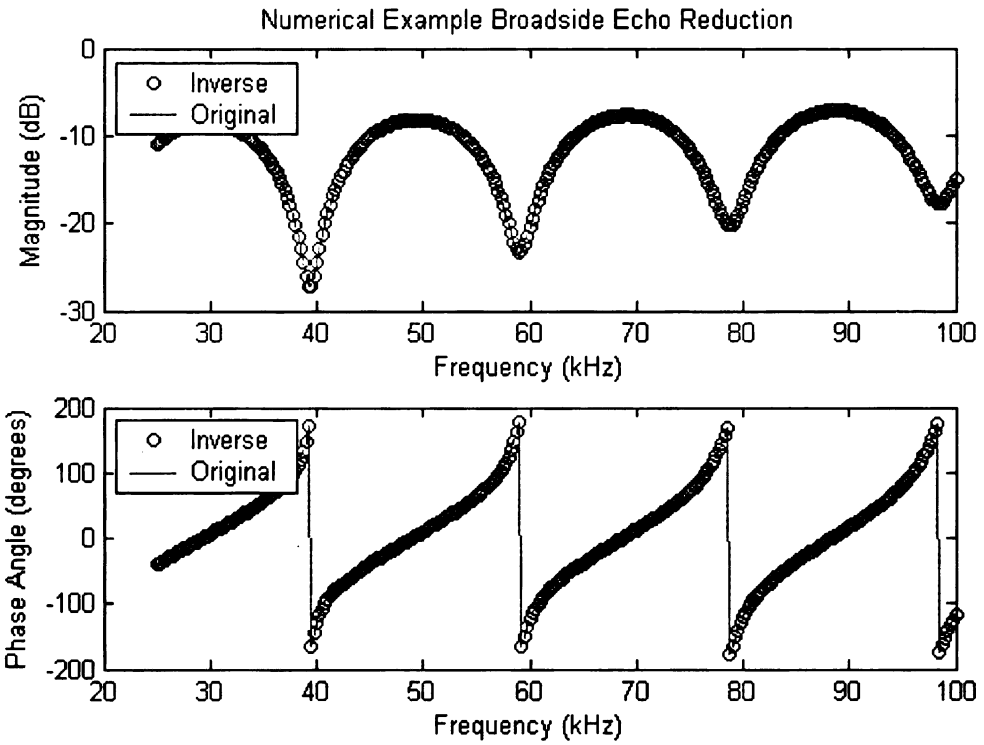

Figure (10) Inverse Predicted and Original Broadside Echo Reduction

Incident Angle

The following is a numerical example used to demonstrate the incident angle inverse method and also as a verification of the equations previously developed. The material in this example is assumed to have a density of 1400 (kg/m^3), be 0.0381 (m) thick and have a complex dilatational and complex shear wavespeed defined as,

$$c_d = 1400 + 10i \ (^m/_s) \tag{46}$$

and

$$c_s = 600 + 15i \ (^m/_s) \tag{47}$$

respectively. The fluid the material is submerged in is assumed to be fresh water with a density of 1000 (kg/m^3), and a compressional wavespeed of 1467.5 (m/s). The incident angle was assumed to be 15 degrees. The values were then inserted into equations (7) and (10) to generate an original echo reduction and insertion loss response as shown in Figures 11 and 12.

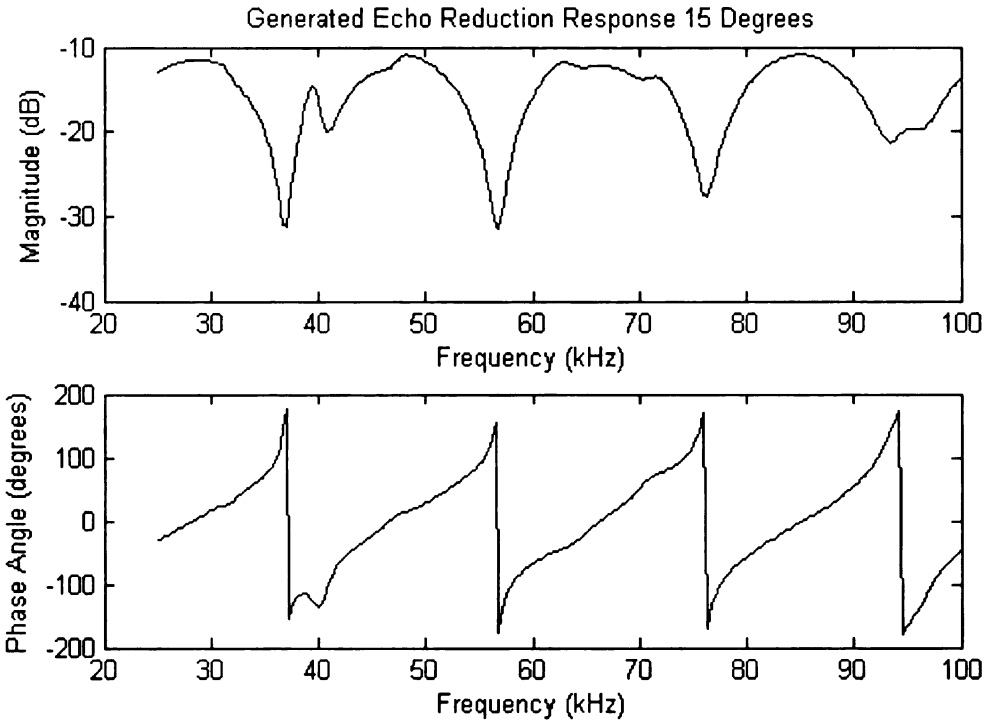

Figure (11) Generated Echo Reduction Response for 15 Degree Incident Angle

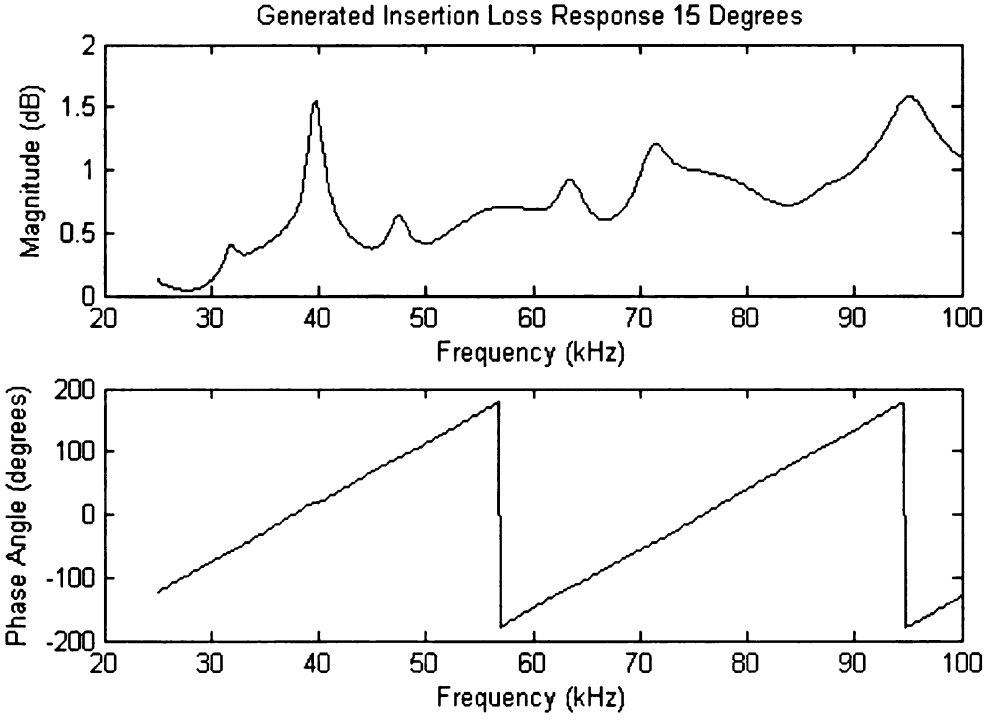

Figure (12) Generated Insertion Loss Response for 15 Degree Incident Angle

The response was then used as the input to the inverse method to estimate the complex dilatational and complex shear wavespeeds. The inverse method recovered the exact complex wavespeeds used to produce the original echo reduction and insertion loss responses. The original responses and the predicted responses are shown in Figures 13 and 14. The two graphs match providing evidence that the inverse program developed is running correctly.

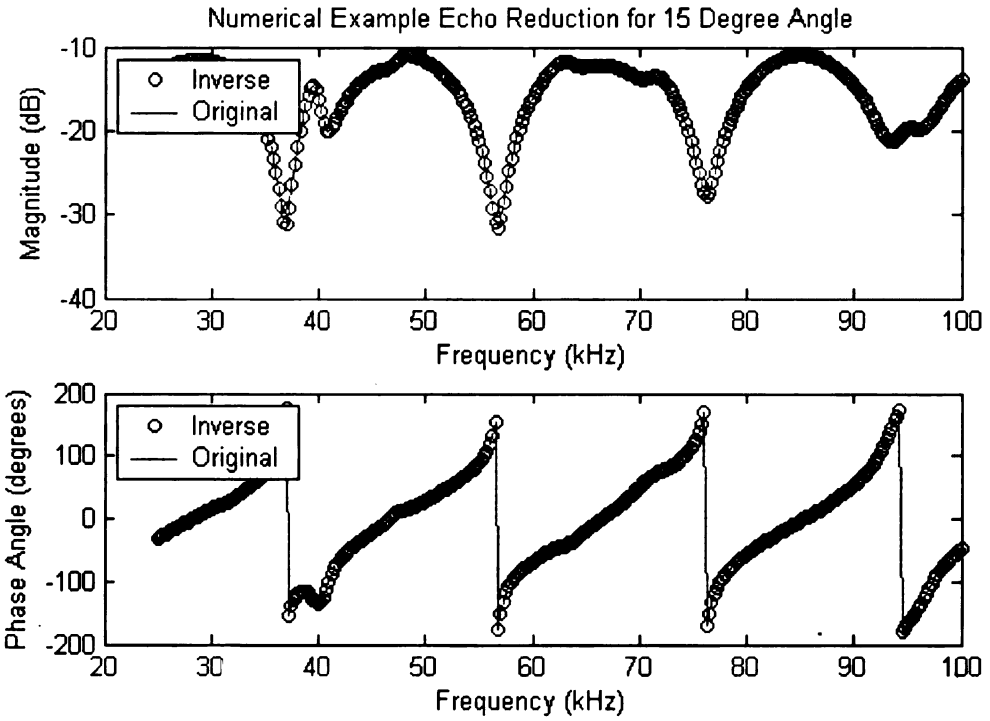

Figure (13) Inverse Predicted and Original ER for 15 Degree Incident Angle

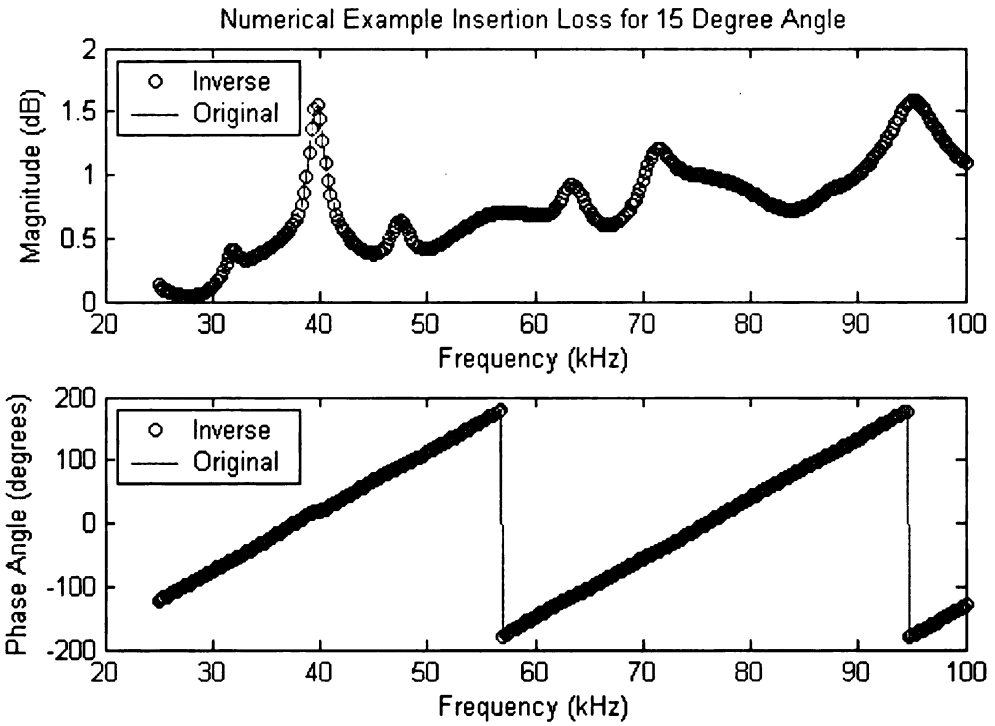

Figure (14) Inverse Predicted and Original IL for 15 Degree Incident Angle

Utilizing equations (24a) and (24b) and the two calculated complex wavespeeds, the numerical material Lamé constants were then determined to be λ = 1.735 GPa and μ = 0.504 GPa. Applying this result to equation (25) produced a Poisson's Ratio of 0.387

PHYSICAL TESTING

The broadside inverse method was applied to two different echo reduction data sets obtained from the ATF and the complex dilatational wavespeed acquired. The results were then compared to complex wavespeeds calculated at specific frequencies with a wavespeed, wavelength method. The incident angle method was not physically tested due to the lack of insertion loss data, but the numerical results imply that both complex wavespeeds can be acquired. Furthermore, mechanical excitation tests of the 3140 material were performed and the complex dilatational and complex shear wavespeeds were calculated at low frequency.

Broadside

The broadside inverse method was applied to two different echo reduction data sets obtained from the ATF. Each data set represented a different material, 3140 and EN-6, and was supplied as a magnitude and phase angle as shown in Figures 15 and 16. The tests were done in fresh water with a density of 1000 (kg/m^3), and a compressional wavespeed of 1467.5 (m/s). The 3140 material had a density of 1185.7 (kg/m^3), and the density of the EN-6 was 1107.1 (kg/m^3). Both samples had a thickness of 0.0254 (m). It should be noted that the data was received as a magnitude and phase angle and was converted to imaginary numbers for calculation purposes.

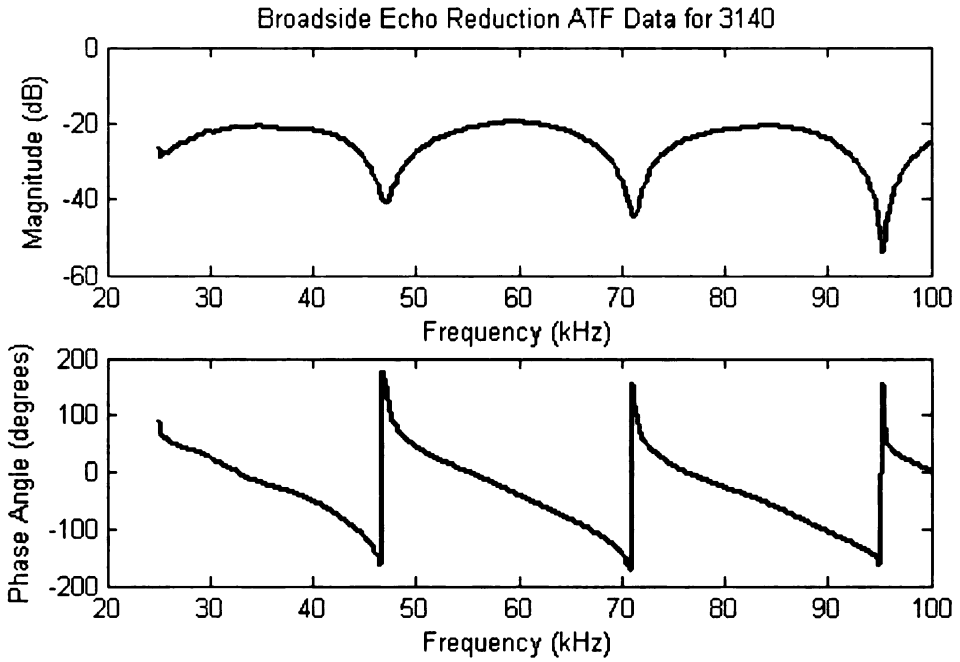

Figure (15) ATF Broadside Echo Reduction Data for 3140

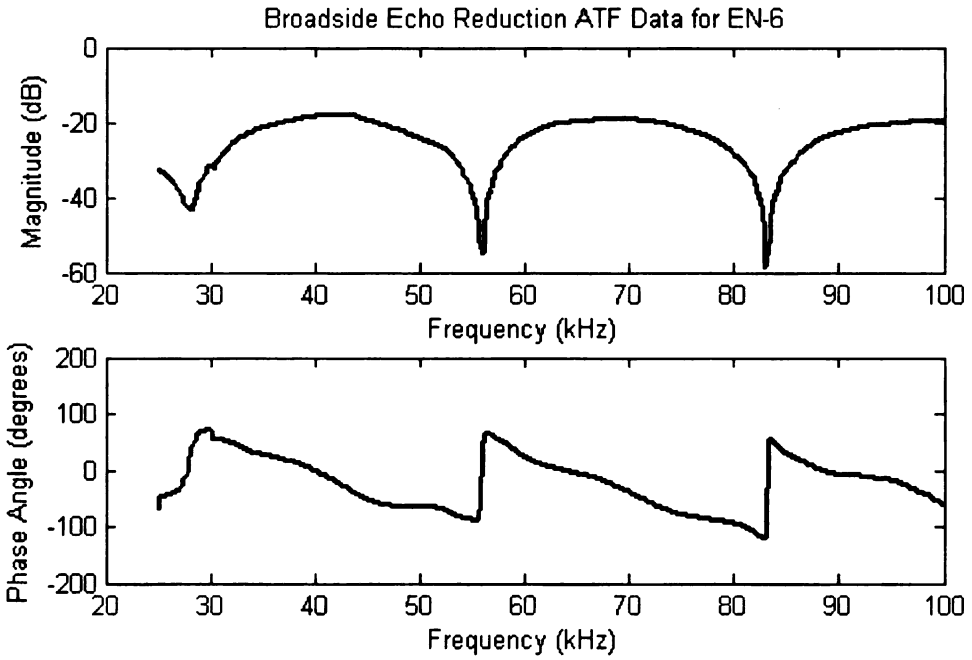

Figure (16) ATF Broadside Echo Reduction Data for EN-6

The nulls in the echo reduction data are of interest in the calculation of the dilatational wavespeed. The dilatational wavespeed at these locations can be calculated using wavelength and wavespeed relationships as [Miklowitz, J. (1984)],

$$c_d = (L * f_1, \quad L * f_2, \quad L * f_3, \quad L * f_4) \tag{48}$$

where L is the wavelength in (m), f is the frequency in (Hz), and the subscripts represent the frequencies where the nulls occur. The nulls in the echo reduction measurements are representative of where the plate thickness is either a half multiple or multiple of the wavelength as,

$$h = \left(\frac{L}{2}, \quad L, \quad \frac{3L}{2}, \quad 2L\right) \tag{49}$$

where h (m) is the plate thickness. With this relationship known the wavespeeds can be calculated at these frequencies as,

$$c_d = \left(2h * f_1, \quad h * f_2, \quad \frac{2h}{3} * f_3, \quad \frac{h}{2} * f_4\right) \tag{50}$$

For the 3140 plate material, these null frequencies were located at 47, 71.25, and 95.25 kHz, corresponding to the 1, 1½, and 2 wavelengths. The ½ wavelength occurs outside of the range of the test data provided. The thickness of the plate was 0.0254 (m), resulting in the material wavespeeds to be calculated as 1194, 1204, and 1210 (m/s), respectively. For the EN-6 plate material the frequencies were found to be 28.25, 56, and 83 kHz, in this case the ½ wavelength is captured in the given data, resulting in the frequencies to correspond to the ½, 1, and 1½ wavelengths. The thickness of the plate was again 0.0254 (m) resulting in wavespeeds being 1435, 1422, and 1406 respectively.

The inverse method was first applied to the 3140 test material at 0 degrees or broadside excitation, and the dilatational wavespeed was determined. The wavespeed was then compared to the previously calculated wavespeeds at the null frequencies as shown in Figure 17.

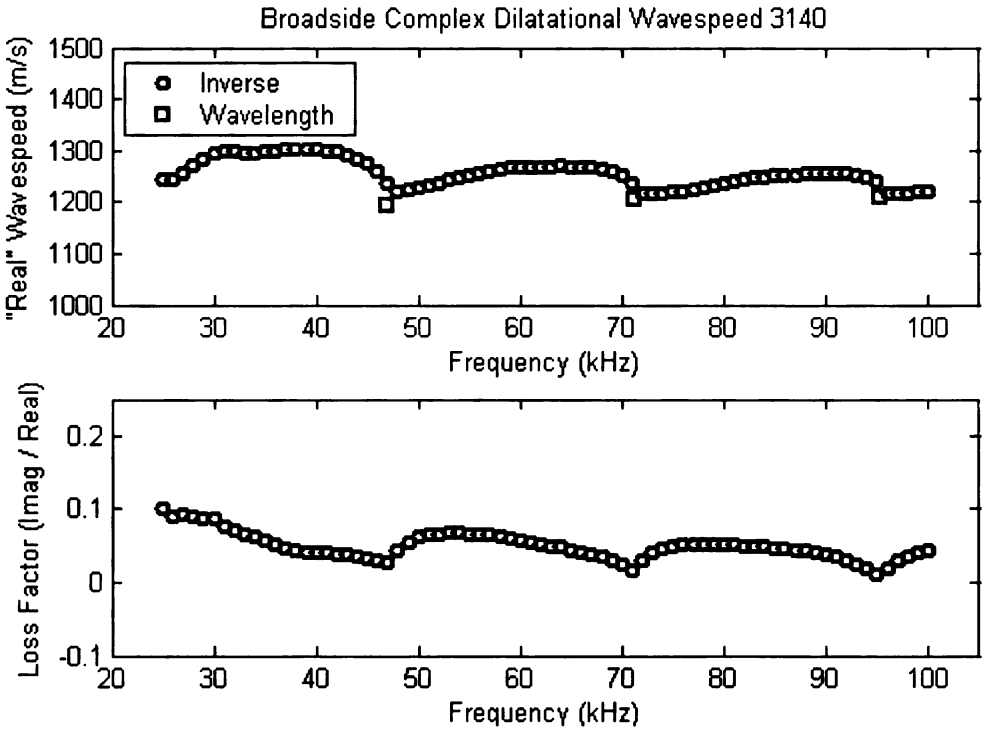

Figure (17) Calculated Complex Dilatational Wavespeed for 3140

In Figure 17, the circles indicate the calculated wavespeed from the inverse method, and the squares represent the wavespeeds calculated at the null frequencies by the wavelength method. The figure shows the inverse method corresponds to the expected values from the null frequency calculations. The bottom graph is the loss factor which represents damping within the system. It can be positive or negative depending on how the wavespeed is defined, but cannot be positive and negative as this would indicate energy being added to the system.

The calculated wavespeeds were then reinserted into the echo reduction model and compared to the test data as seen in Figure 18. This insured the inverse method was working properly and produced realistic results. The circles indicate the echo reduction from the inverse method, and the line for the test data. The two overlie exactly providing further evidence the calculated wavespeeds are accurate. The inverse method was then applied to the EN-6 test material and the determined wavespeed was compared to the calculated wavespeeds at the null frequencies as shown in Figure 19.

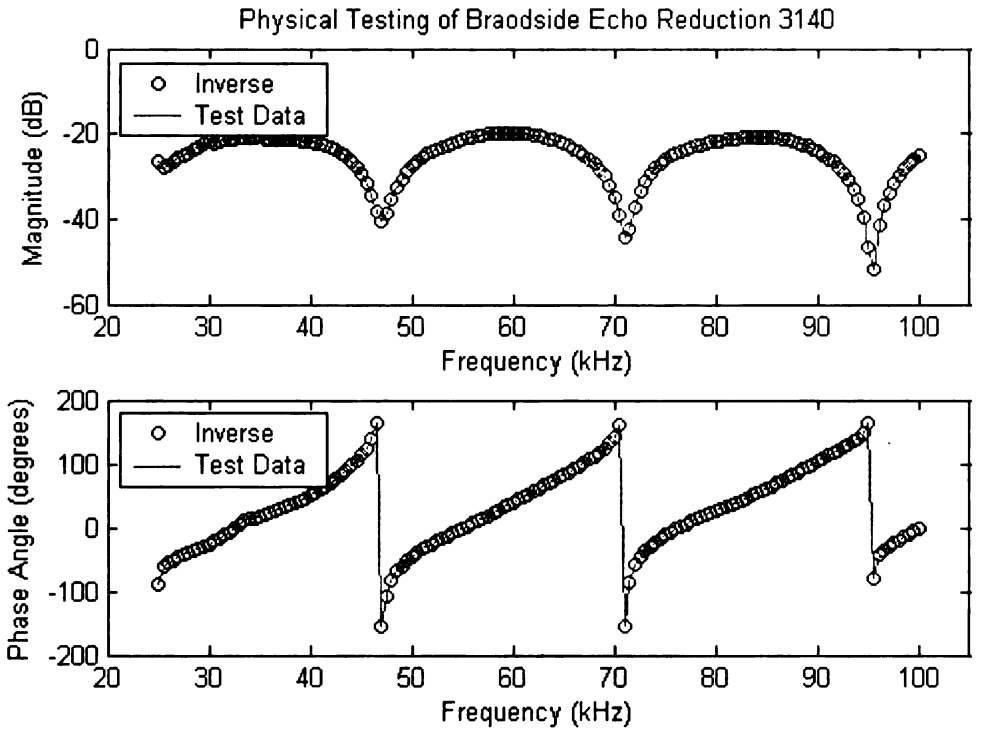

Figure (18) Physical Testing of Broadside Echo Reduction for 3140

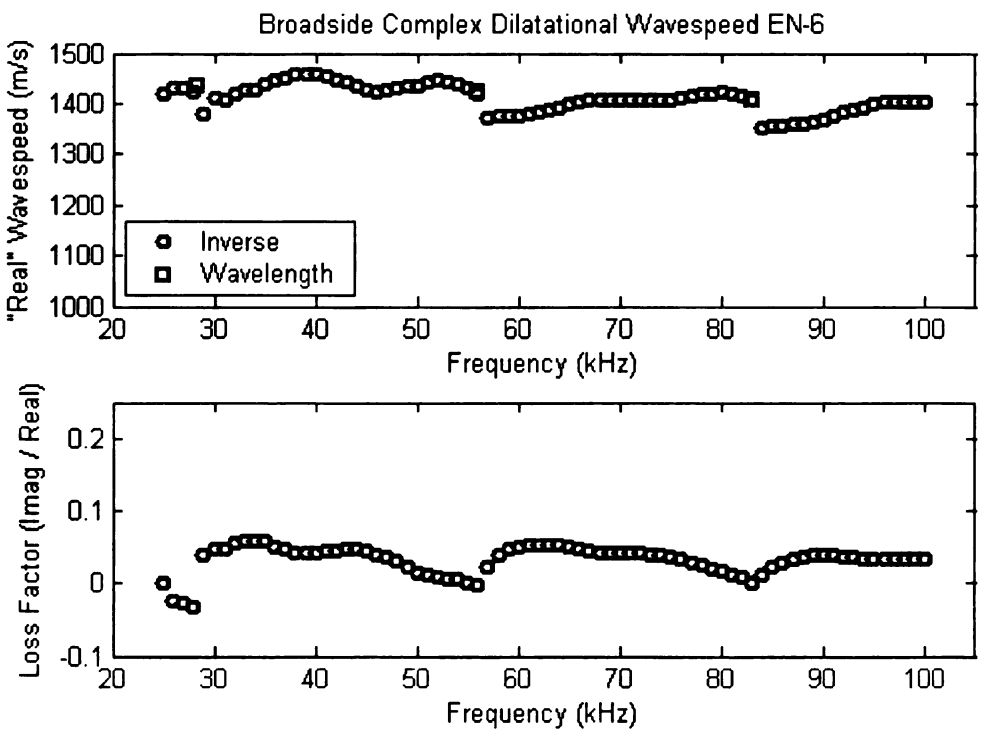

Figure (19) Calculated Complex Dilatational Wavespeed for EN-6

Again, the circles indicate the calculated wavespeed from the inverse method, and the squares represent the wavespeeds calculated at the null frequencies. They show the inverse method corresponds to the expected values from the null frequency calculations. The bottom graph displays the loss factor which represents the system damping. The negative loss factor found in the lower frequencies is thought to be related to the inverse program starting at the edge of a null frequency and not converging to the correct values until after the null. It should be noted that there are multiple solutions that satisfy the echo reduction equations and a check such as the one described here must be done to ensure that the results obtained are physically possible. Again, to insure the inverse method was working properly and produced realistic results, the calculated wavespeeds were reinserted into the echo reduction model and compared to the test data as seen in Figure 20. The circles indicate the echo reduction from the inverse method, and the line for the test data. Again, they show the inverse method exactly overlays the test data values.

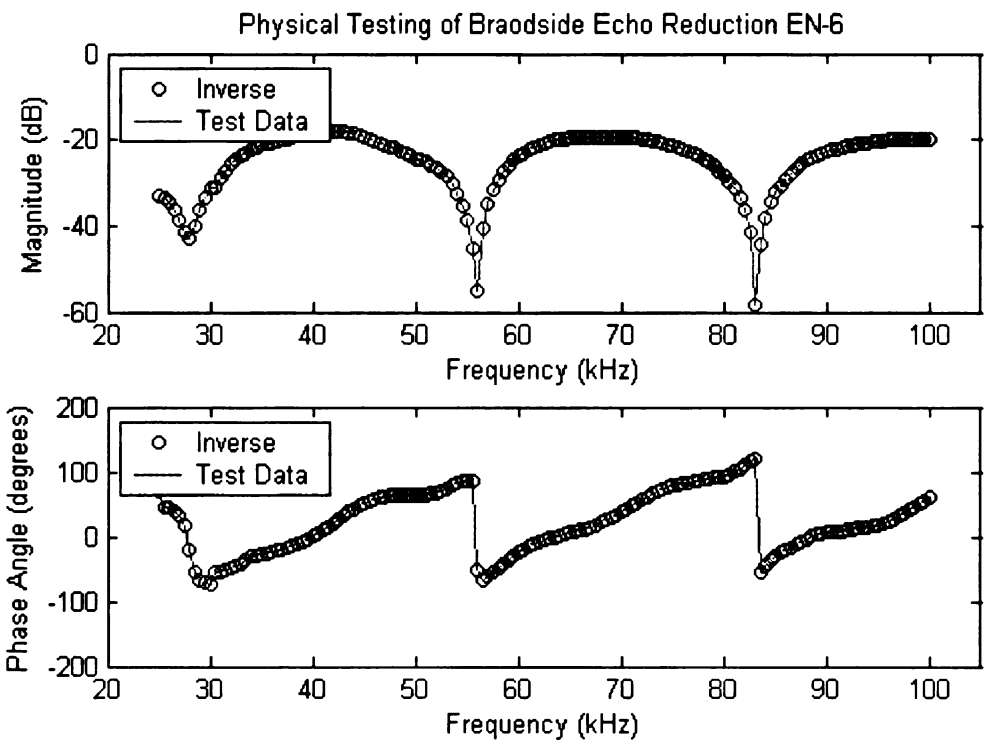

Figure (20) Physical Testing of Broadside Echo Reduction for EN-6

The predicted wavespeeds by the inverse method and the values calculated at the null frequencies were compared and found to be within 3.5 percent of each other. The real wavespeeds for both materials at the null frequencies, along with the associated differences are summarized below in Tables 1 and 2.

Table 1. Inverse Method and Null Frequency Comparison for 3140

3140	Frequency (Hz)	Wavelength	Inverse Method (m/s)	Wavelength Method (m/s)	Percent Difference
	47000	1	1236.1	1193.8	3.5
	71250	1.5	1226.6	1204.4	1.8
	95250	2	1234.6	1209.7	2.1

Table 2. Inverse Method and Null Frequency Comparison for EN-6

EN-6	Frequency (Hz)	Wavelength	Inverse Method (m/s)	Wavelength Method (m/s)	Percent Difference
	28250	0.5	1420.0	1435.1	1.1
	56000	1	1418.0	1422.4	0.31
	83000	1.5	1407.9	1405.5	0.17

Mechanical

The model for the two mechanical test setups has been previously developed [Hull, A., (2003)]. This previous work provides a method to determine the complex shear and complex dilatational wavespeeds from the frequency response functions produced by the two test setups built. The dilatational test was applied to a 1.5 inch diameter 1 inch high round sample of the 3140 material. The vertical test excited the 3140 material sample with noise to a frequency greater than the first resonance peak. The excitation generated a frequency response function for the sample as seen in Figure 21.

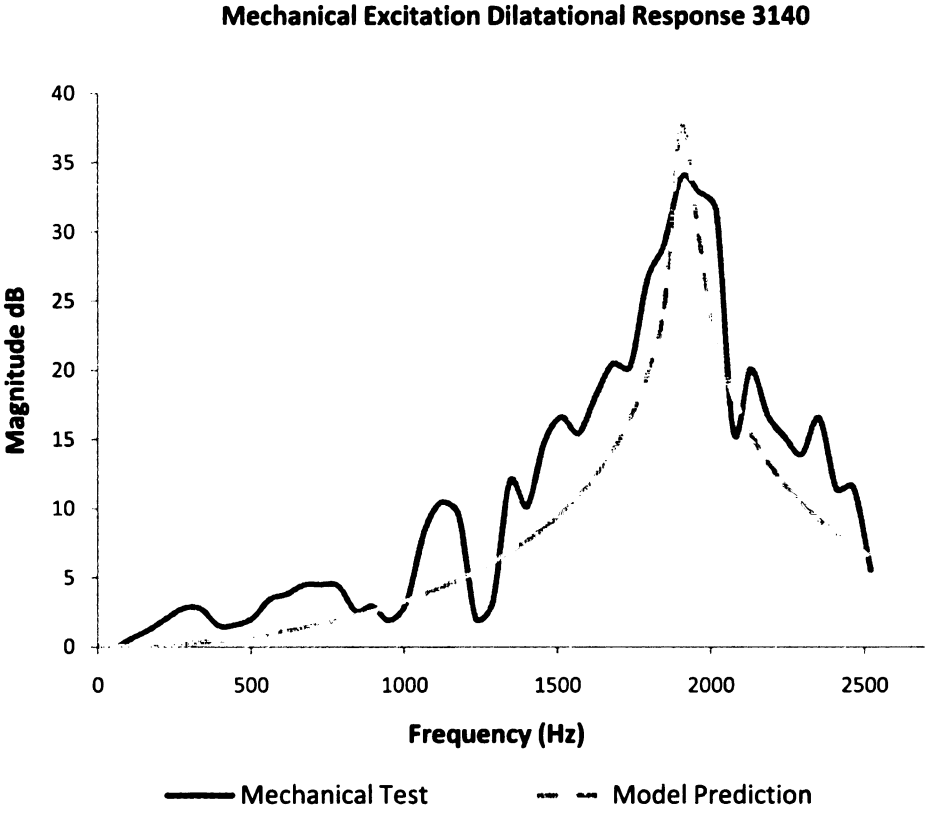

Figure (21) Dilatational Response from Vertical Mechanical Excitation

The dilatational wavespeed from the previously developed model was then adjusted until it produced a frequency response that corresponded with the acquired data. The dilatational wavespeed required for the model to correspond with the data was determined to be 195 (m/s).

The two-dimensional model assumes an infinite length and a specified height. To ensure the infinite length in the x-direction was an accurate model for the shear response in the horizontal test, two samples of different lengths of the 3140 material were tested. The first sample was 3 inches long in the x-direction and 1 inch high, and the second one was 2 inches long in the x-direction and 1 inch high. The horizontal test excited each sample of the 3140 material with noise to a frequency greater than the first resonance peak. The excitation generated a

frequency response function for each of the two samples as seen in Figure 22. The shear wavespeed from the previously developed model was then adjusted until it produced a frequency response that corresponded with the acquired data.

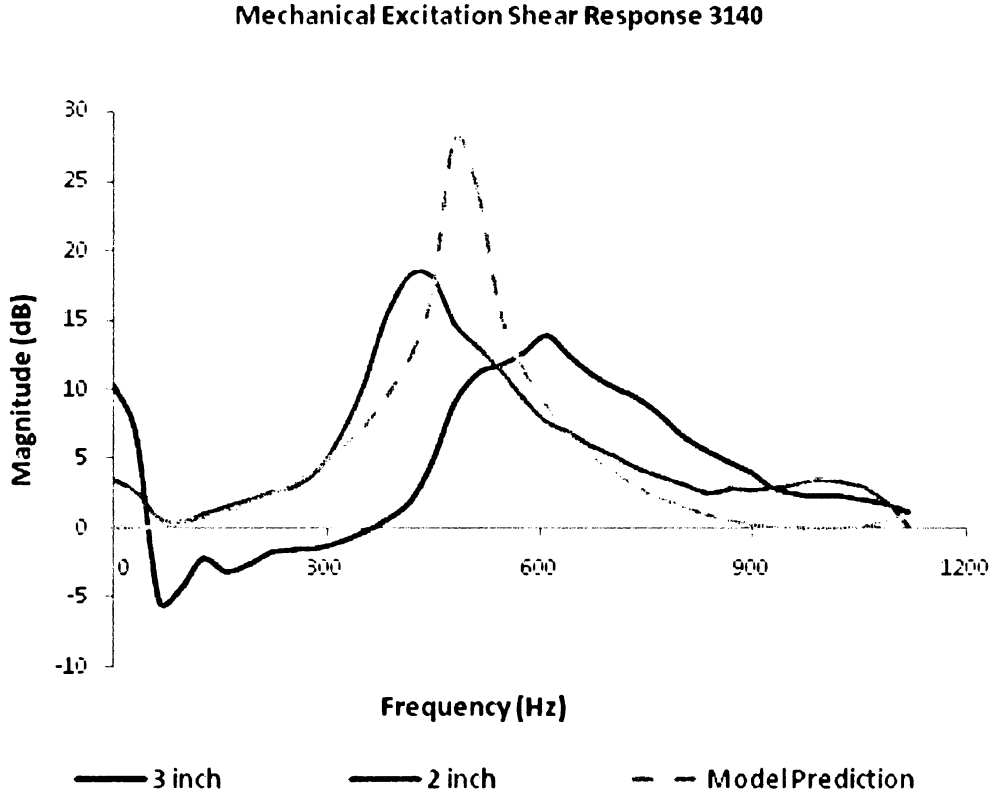

Figure (22) Shear Response from Horizontal Mechanical Excitation

The two different length samples produced different resonance peaks in their frequency responses. This suggests that a longer sample may be required to satisfy the infinite length assumption used in the model. Mindful of this fact, the shear wavespeed was adjusted to correspond with both generated responses and was determined to be 50 (m/s). Using the two determined wavespeeds and equations (24a) and (24b), the material Lamé constants were calculated to be λ = 39.1 (Mpa) and μ = 2.96 (Mpa). Applying the Lamé constants to equation (25) resulted in a Poisson's Ratio of 0.465.

DISCUSSION

The inverse methods above were numerically shown to recover both the complex dilatational and complex shear wavespeeds from generated echo reduction and insertion loss data. Furthermore, the broadside method was applied to physical echo reduction test data and the results show that the predicted dilatational wavespeed matches closely with the wavelength method results. It should be noted that the echo reduction data received was given as incident measurement divided by reflected response. The data was inverted in the inverse method to reflected response over incident measurement to avoid division by zero during nulls in the response. Another benefit of taking this approach is seen if the real and imaginary parts of the echo reduction are examined. Having the response in the denominator results in asymptotes where there are nulls, but inverting the data to have the incident in the denominator results in smooth curves as seen in Figures 23 and 24.

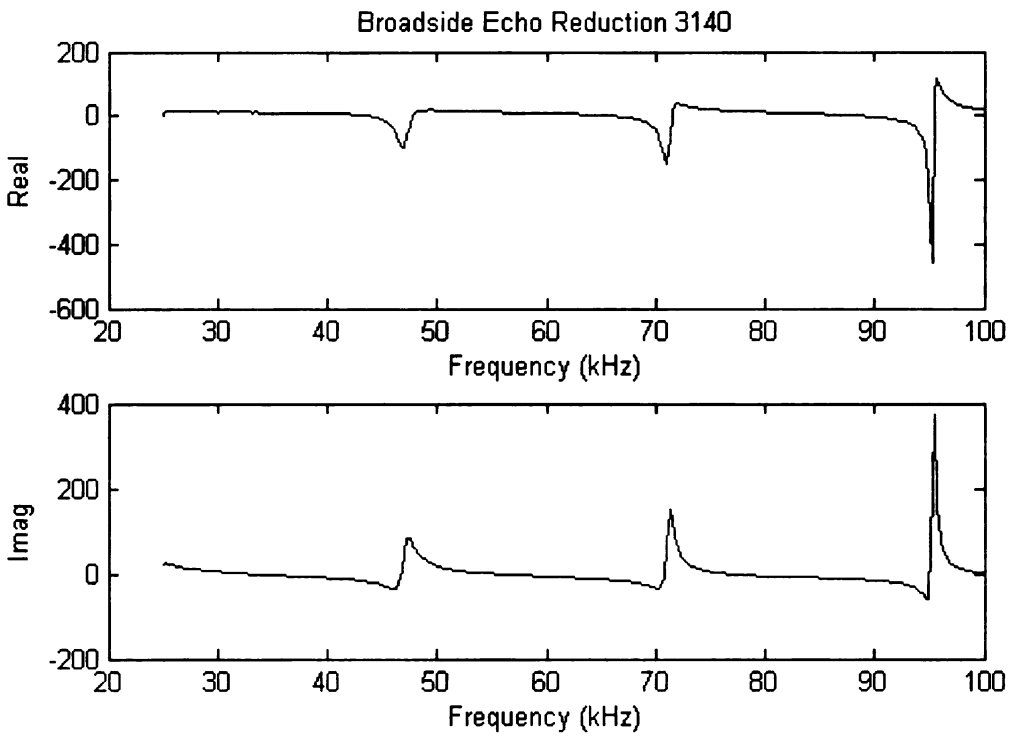

Figure (23) Real and Imag Parts of Original Echo Reduction

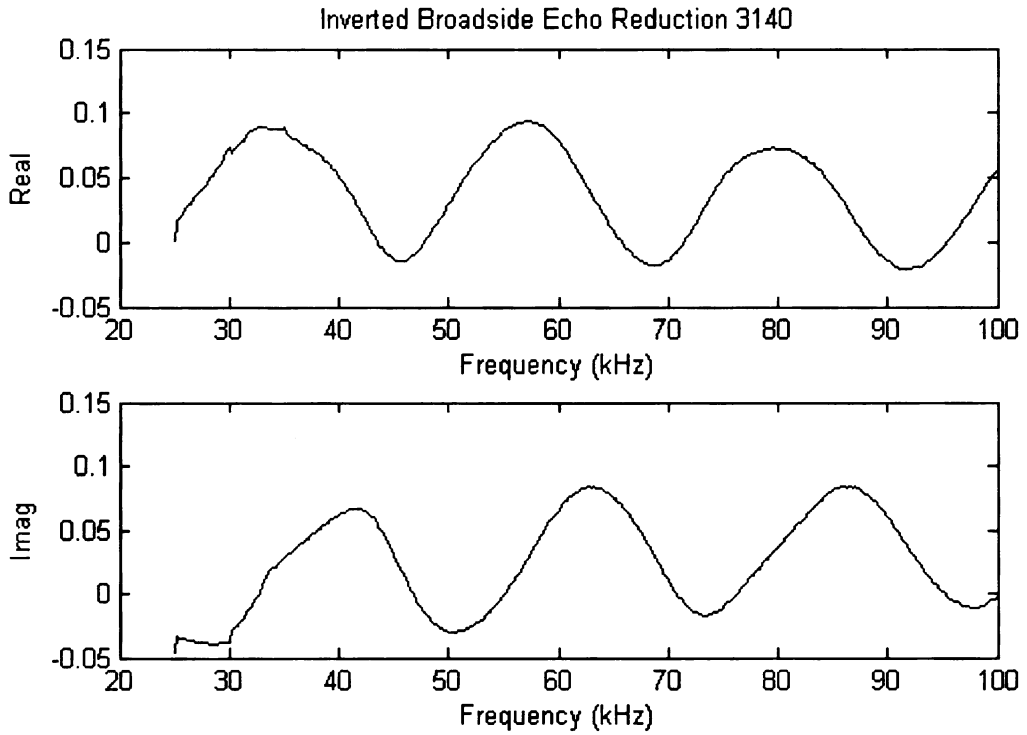

Figure (24) Real and Imag Parts of Inverted Echo Reduction

The Newton-Raphson method relies on partial derivatives of the real and imaginary parts of the echo reduction to calculate the material properties. This is more readily facilitated with a smooth function.

The complex shear wavespeed could not be directly acquired from the acoustical data for comparison with the mechanical results. However, a few observations can be made from observing the echo reduction test data. First, the dilatational resonances increase with the increasing incident angle as seen in Figure 25. The shear resonances are barely noticeable in the 5 degree plot, but become more prominent as the incident angle increases. Notice that the shear resonances do not change frequency with angle but only magnitude. This is also shown in the theoretical dispersion curve, which shows the frequency at which the various free waves can propagate.

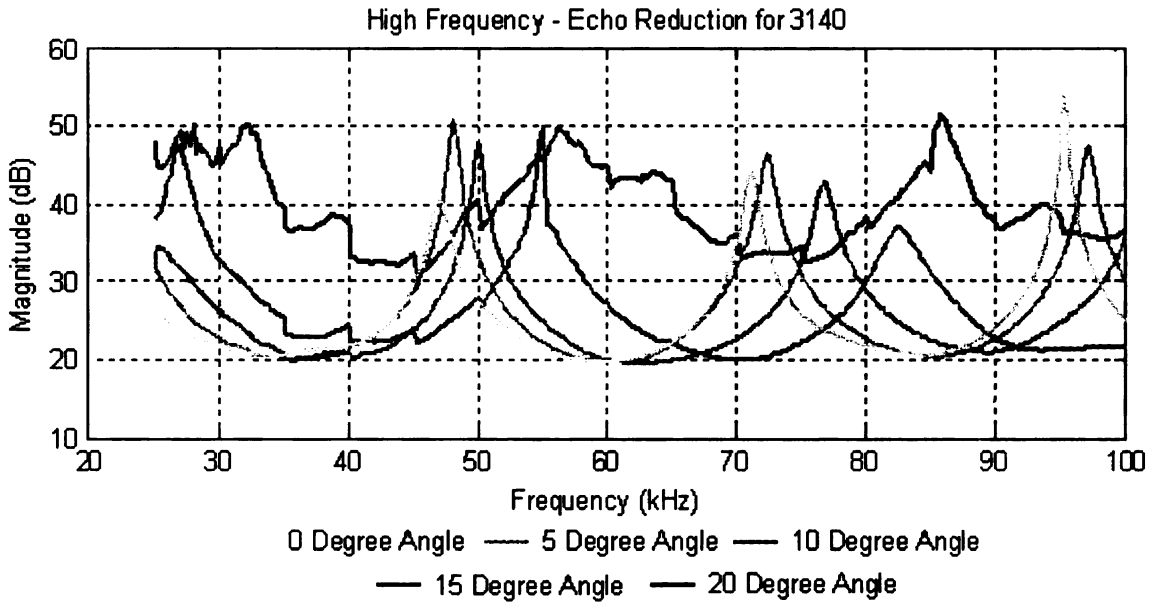

Figure (25) Physical Testing of Echo Reduction at Varying Angles for 3140

The dilatational and shear wavespeeds can then be adjusted so that the theoretical dispersion curve matches the experimental data. This was done for the 3140 material and zoomed in on where the ATF acquired data. The values of 1200 (m/s) for the dilatational wavespeed and 255 (m/s) for the shear wavespeed were estimated and superimposed on the dispersion curve as seen in Figure 26. Using the two determined wavespeeds and equations (24a) and (24b), the material Lamé constants were calculated to be 77.1 (Mpa) and 1.55 (Gpa). The material Lamé constants resulted in a Poisson's Ratio of 0.476. In the dispersion curve, the dilatational wavespeed is held constant, where in the experimental data it is believed to be increasing with incident angle. This would account for the deviation of the dilatational wavespeed from the theoretical dispersion cure and suggests that the material is essentially becoming stiffer with increasing angle.

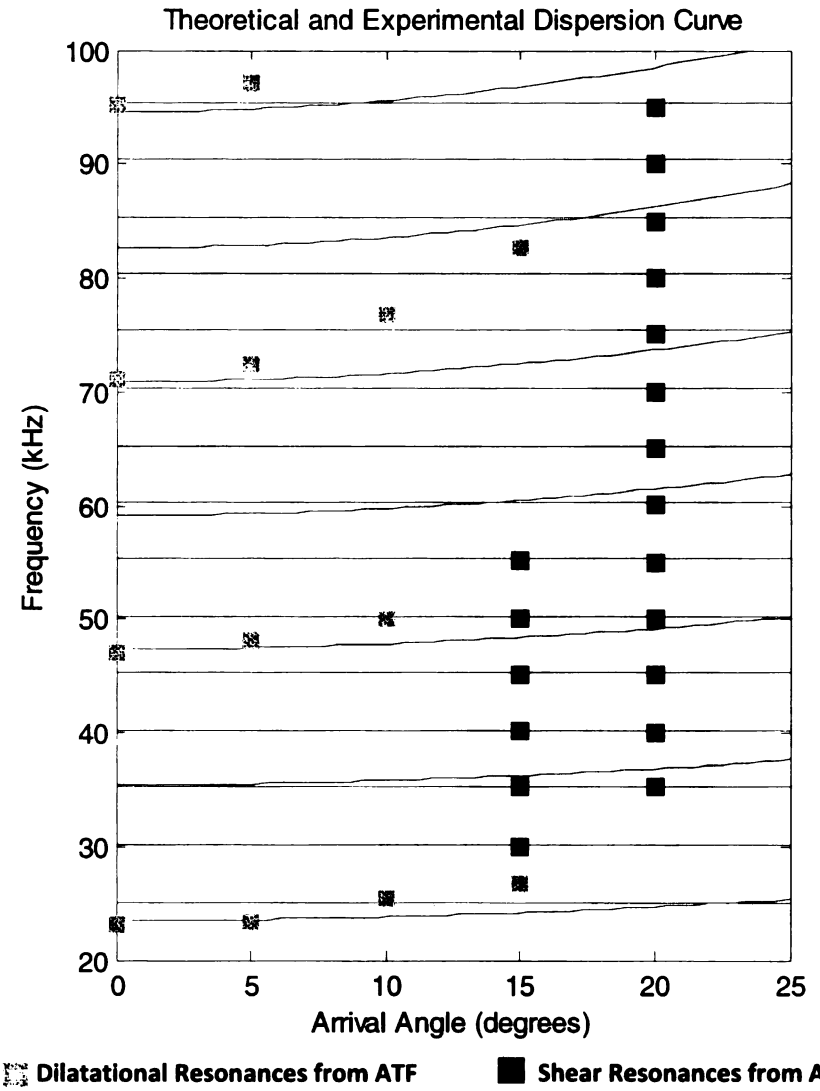

Figure (26) Theoretical Dispersion Curve and Physical Test Data from 3140

The wavespeeds determined from the mechanical tests are much lower than the ones used to generate the dispersion curve. This suggests that the wavespeeds are also increasing with frequency. It should be noted however that the Poisson's Ratio was only 2% different between the low frequency and high frequency. Further testing is required to try and quantify the relationships between the wavespeeds and the frequency, and the wavespeeds and incident angle.

CONCLUSION

This paper has derived an inverse method for accurately predicting the complex dilatational and complex shear wavespeeds of a thick plate material from echo reduction and insertion loss test data. The broadside method, used to calculate dilatational wavespeed only, was applied to a numerical example which demonstrated that the method can accurately predict the complex dilatational wavespeed using echo reduction data. Furthermore, it was applied to experimental data from two different materials and predicted wavespeeds to within 3.5% of values calculated at the resonance frequencies through a wavelength, wavespeed method.

An inverse method to acquire both the complex dilatational and complex shear wavespeeds was also developed. Both of these wavespeeds are required to calculate the material Lamé constants. This method was numerically tested and was demonstrated to accurately recover the defined wavespeeds. The calculation of the Lamé constants and Poisson's Ratio was then demonstrated. The method was not physically tested as insertion loss data was not available.

A mechanical shaking device was also developed. It excited the 3140 material at lower frequencies and used a previously developed method to determine the dilatational and shear wavespeeds. The results suggest that the wavespeeds are frequency dependent as they were lower than the wavespeeds estimated from the dispersion curves. It was also observed that although the wavespeeds varied the Poisson's ratio remained relatively constant.

Future work should involve acquiring more precise insertion loss data and applying it along with the echo reduction data in the incident angle method. This would provide a basis for the study of the angle dependant, complex dilatational wavespeed and also allow for the acquisition of the high frequency complex shear wavespeed. Alternatively, if higher precision insertion loss

measurements are not feasible the materials could be tested in a different fluid that would provide larger insertion loss data. In addition, different size materials should be tested with the mechanical shaking device to quantify the divergence from the infinite assumption taken in the model. Methods to increase the frequency range of the mechanical tests should also be examined. One area of exploration is the use of a piezo-actuator to excite the material. This would allow for higher frequency measurements which would facilitate a better connection between the mechanical and acoustical tests. Studies on the sensitivity of the inverse method to parameter changes should also be examined in order to quantify experimental uncertainties in the results.

APPENDICIES

APPENDIX A: Mechanical Device Specifications

Mechanical Device

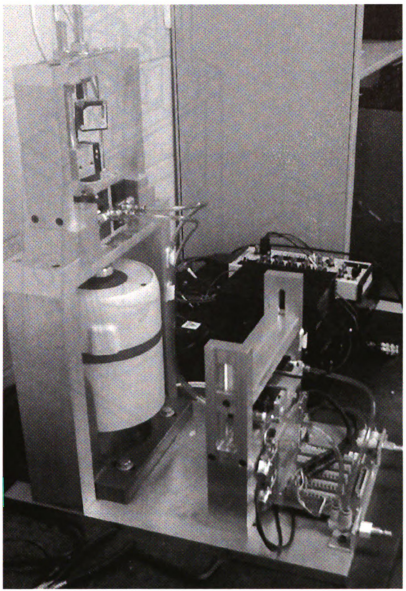

Figure (27) Horizontal and Vertical Mechanical Device

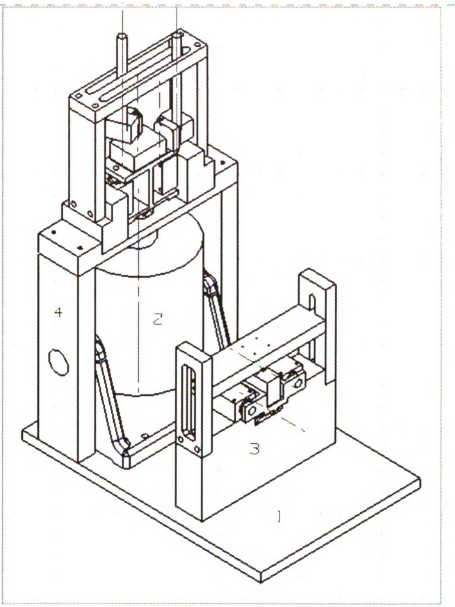

Parts List

PC NO	PART NAME	QTY
4	V_ASSEMBLY	1
3	H_ASSEMBLY	1
2	SHAKER	1
1	BASE_PLATE	1

Figure (28) Horizontal and Vertical Mechanical Device Setup Drawing

Procured Equipment

1. Ling Dynamic System 400 Series Mechanical Shaker with 196 N of force with adequate cooling

Horizontal Shear Test

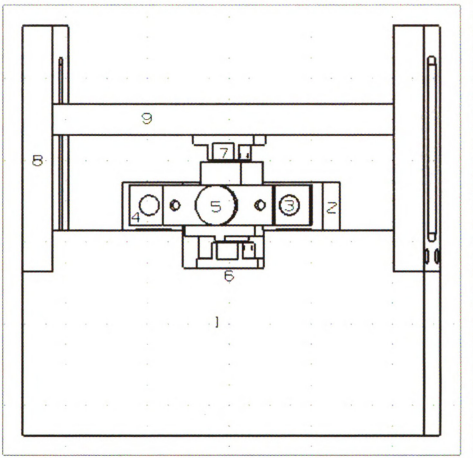

PARTS LIST

9	E_CROSS	1
8	E_VERTICAL	2
7	ENCODER	2
6	E_BRACKET	2
5	SHAKER_ADAPTER	1
4	CART	1
3	SHAFT	2
2	BEARING_ASSEM	2
1	H_BEARING_SUPPORT	1
PC NO	PART NAME	QTY

Figure (29) Horizontal Mechanical Shear Test Assembly

Procured Equipment

1. Bearing assemblies are NewWay S301201 commercial air bearings including bushings and pillow blocks. Recommended air supply is 60 psi.

2. Encoders are Renishaw RGF0100H125A with a resolution of 0.2μm. Include encoder reader and RGF0100H125A Interface cards. A and B positive channels are wired to National Instrument PCI-6601 card.

Manufactured Parts

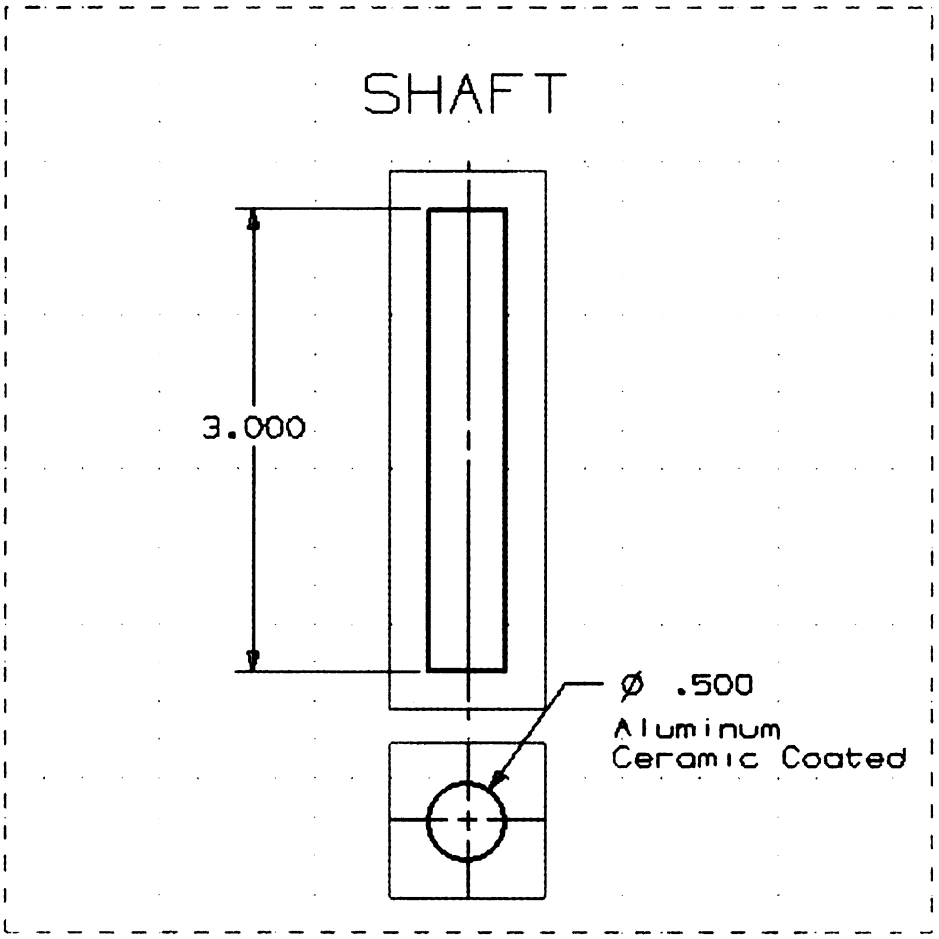

Figure (30) Specifications for Horizontal Material Cart Shaft

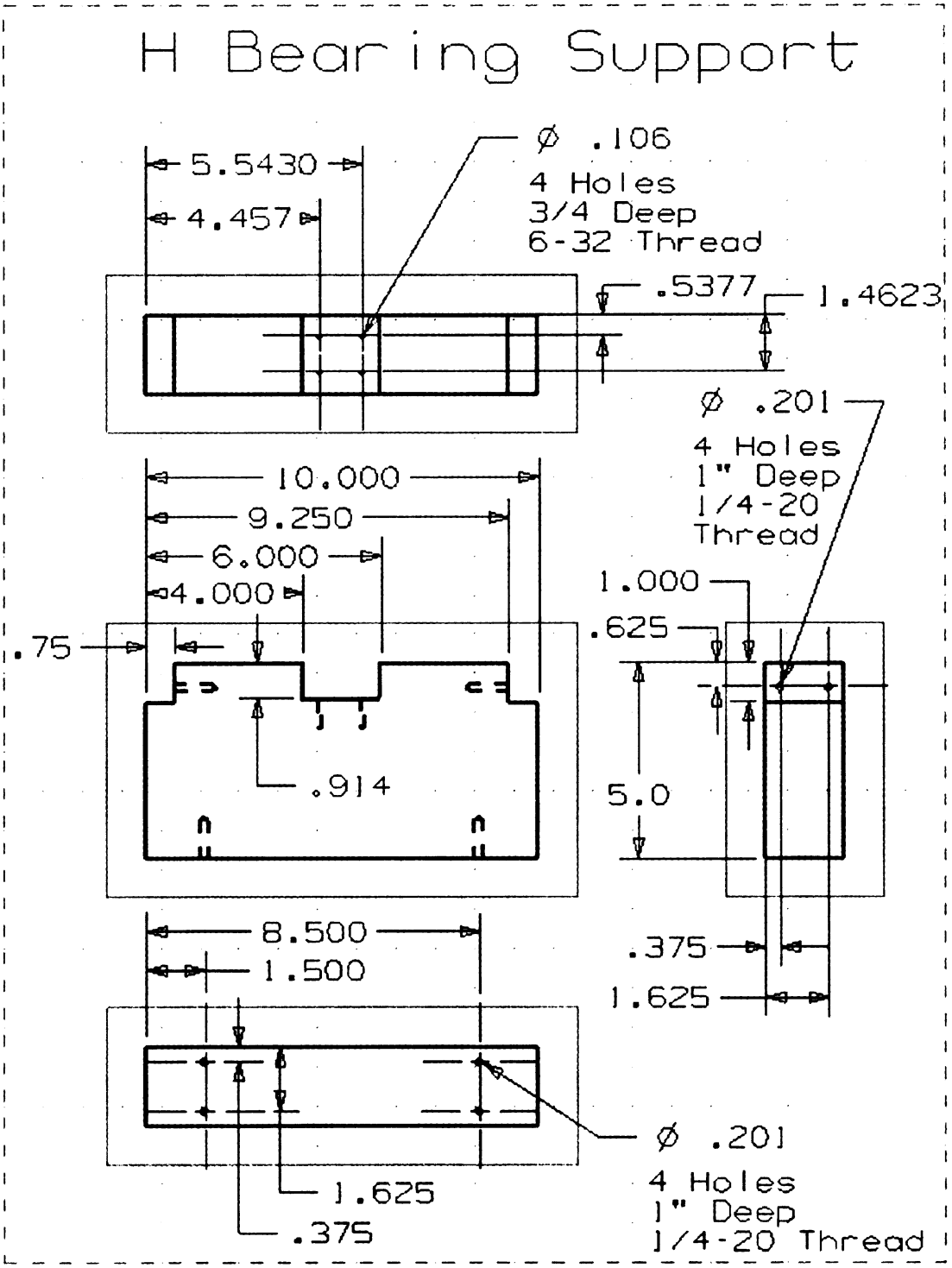

Figure (31) Specifications for Horizontal Bearing Support

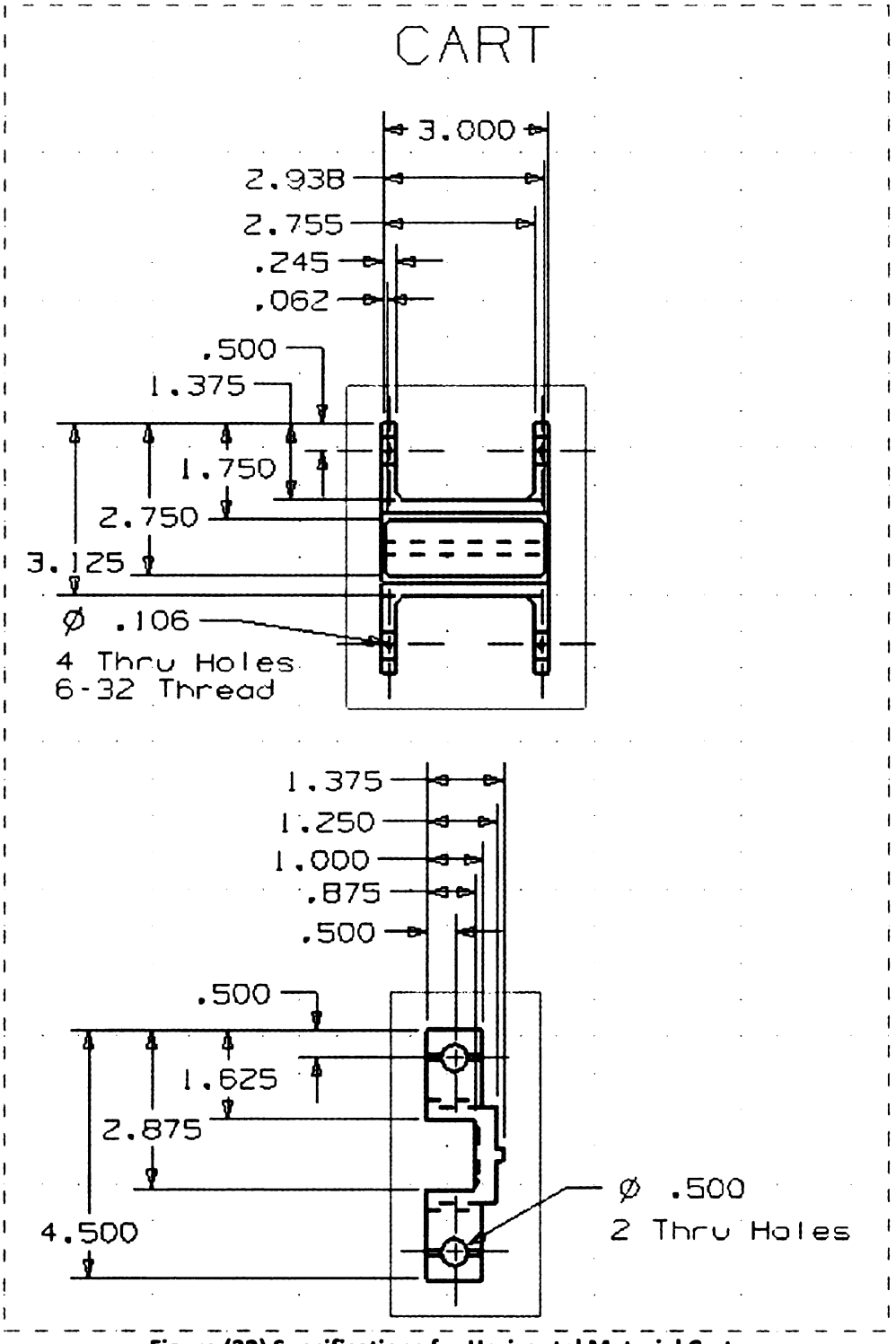

Figure (32) Specifications for Horizontal Material Cart

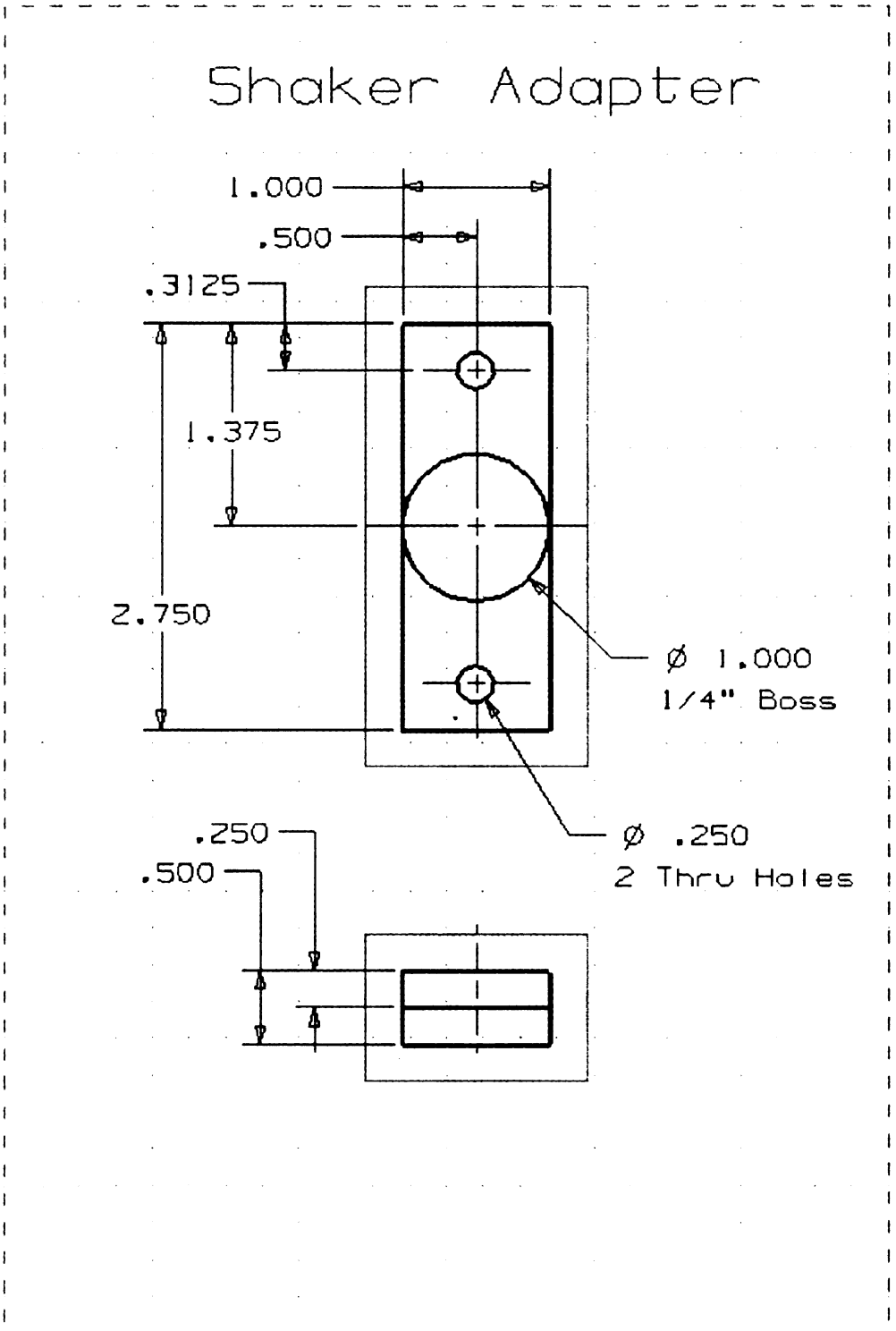

Figure (33) Specifications for Mechanical Shaker Adapter

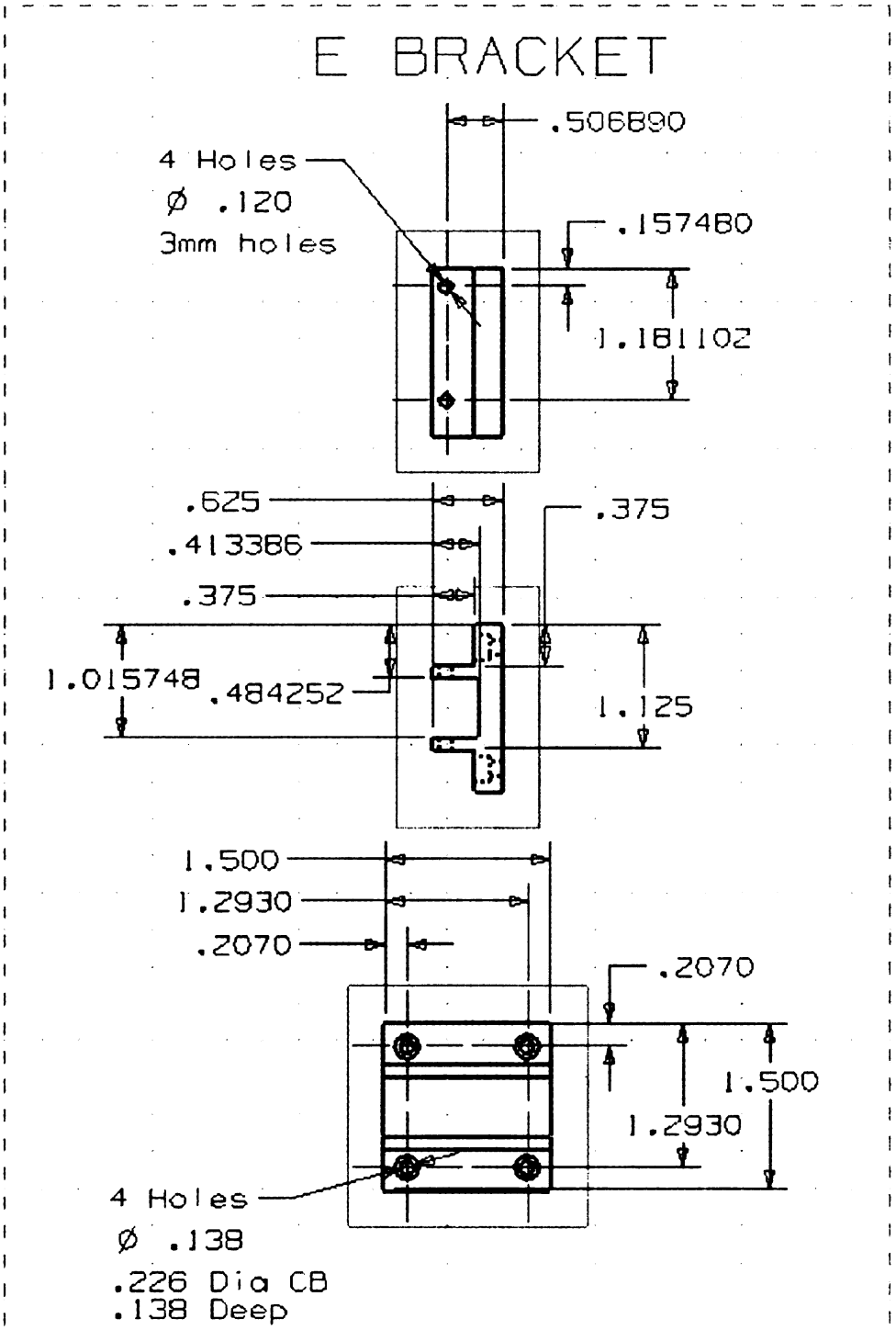

Figure (34) Specifications for Encoder Bracket

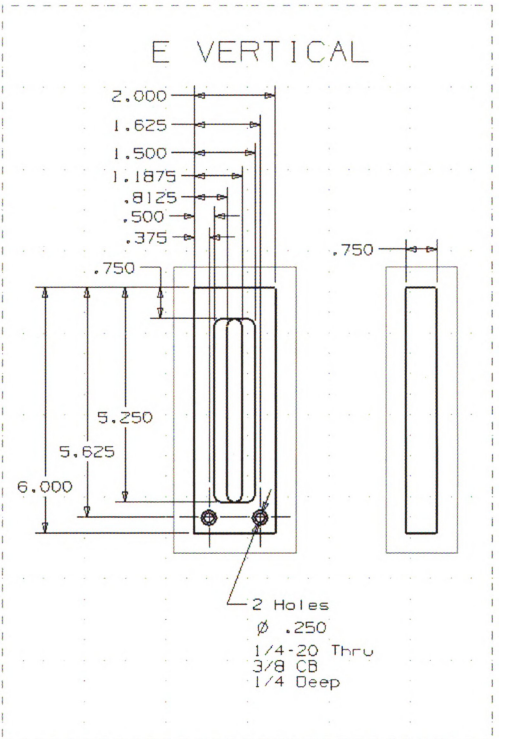

Figure (35) Specifications for Vertical Support of Encoder Mount

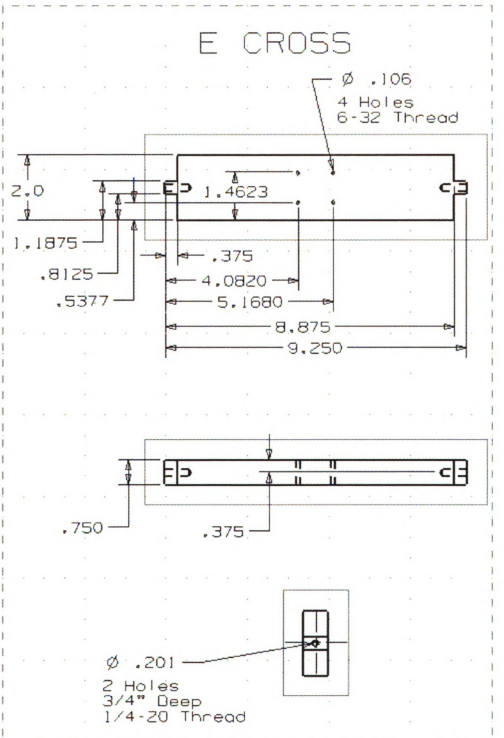

Figure (36) Specifications for Cross Support of Encoder Mount

Software Developed in LabView 7.1

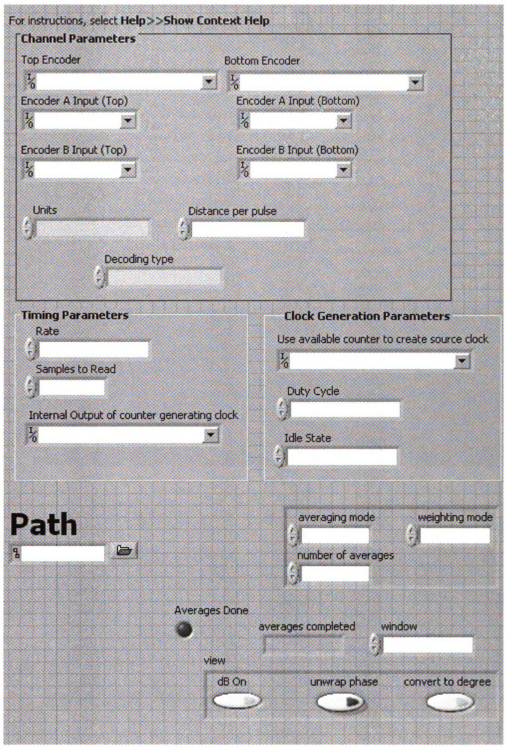

Figure (37) LabView Front Panel Inputs for Horizontal Shear Test

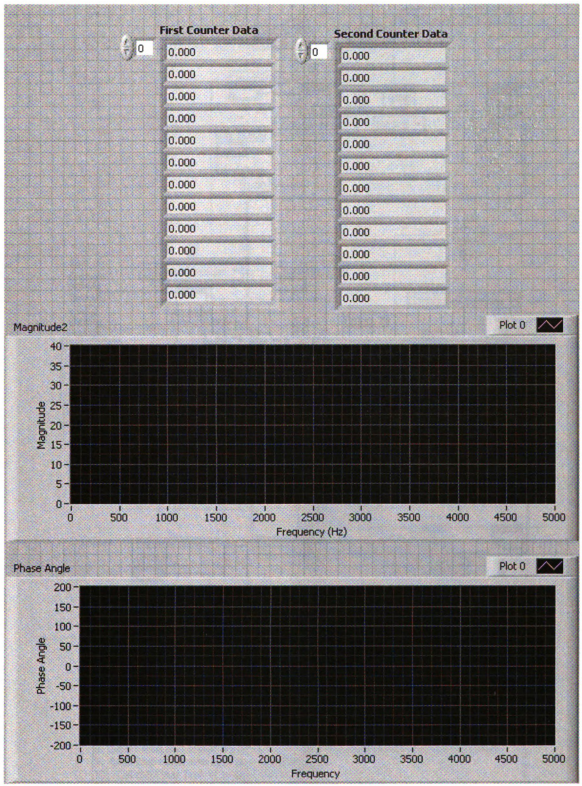

Figure (38) LabView Front Panel Outputs for Horizontal Shear Test

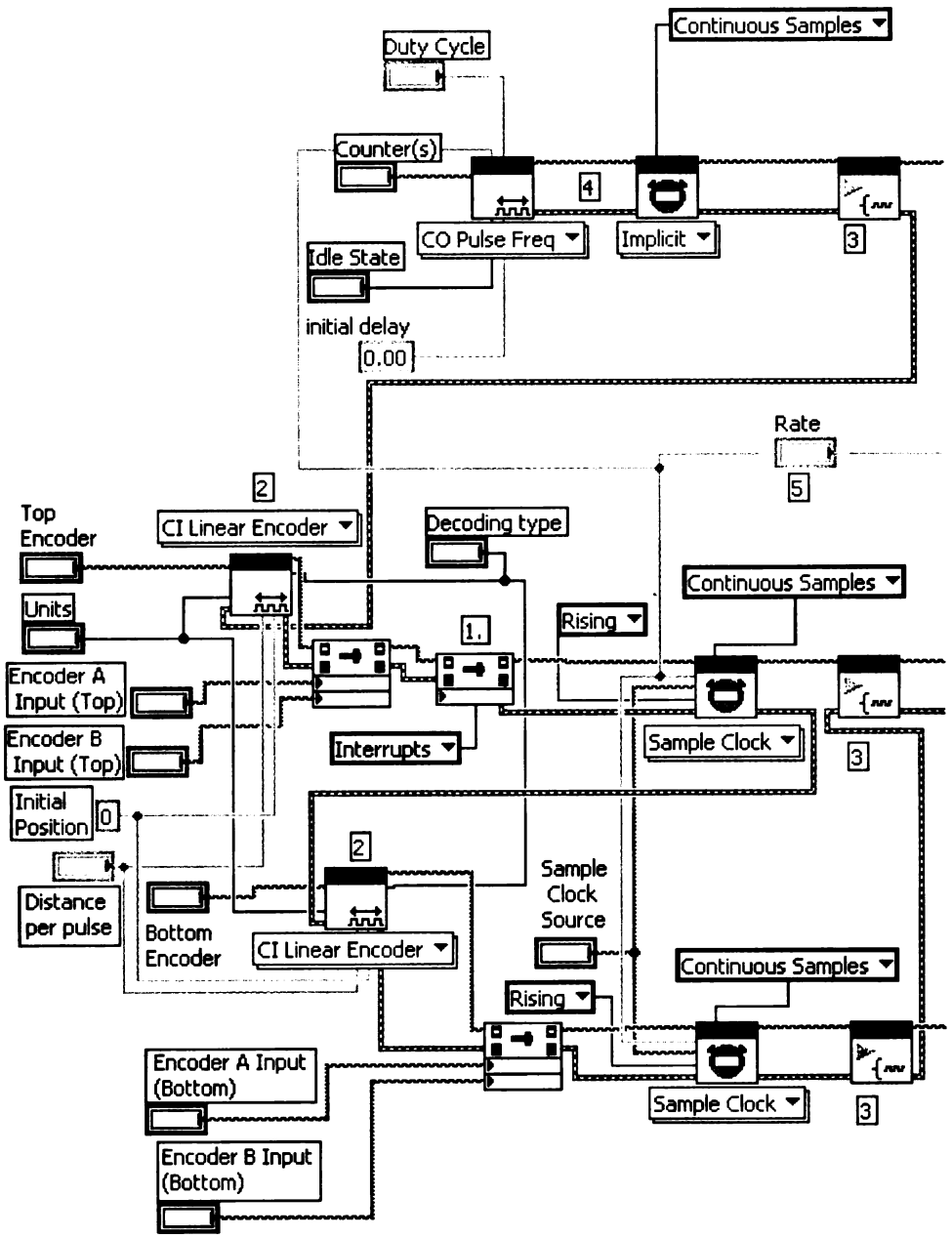

Steps:
1. Uses Interrupt (only 1 channel of DMA)
2. Define Encoder parameters
3. Call the Start VI to start the acquisition.
4. Generates a clock
5. Sets rate to take samples
6. Generates the Magnitude and Phase on Front Panel
7. Generates Real and Imaginary parts of Response function to Export to Excel
8. Saves Real and Imaginary Parts to .txt file path specified by Path on Front Panel
9. Ends loop when averages are completed
10. Call the Clear Task VI to clear the Task.
11. Use the popup dialog box to display an error if any.

Figure (39) LabView Block Diagram Inputs for Horizontal Shear Test

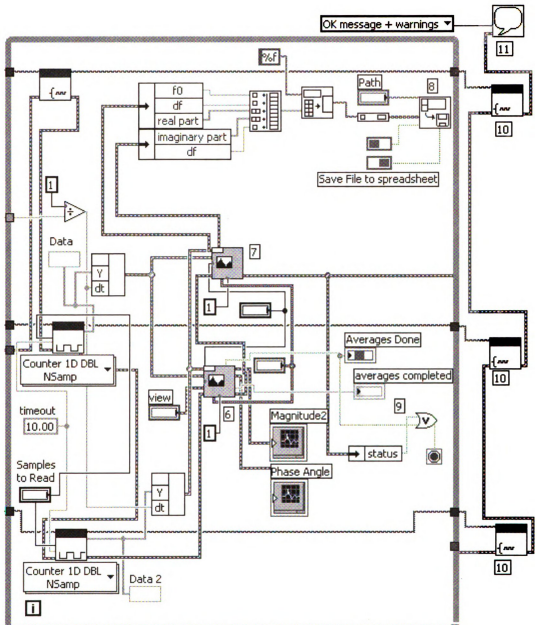

Figure (40) LabView Block Diagram Outputs for Horizontal Shear Test

Vertical Dilatational Test

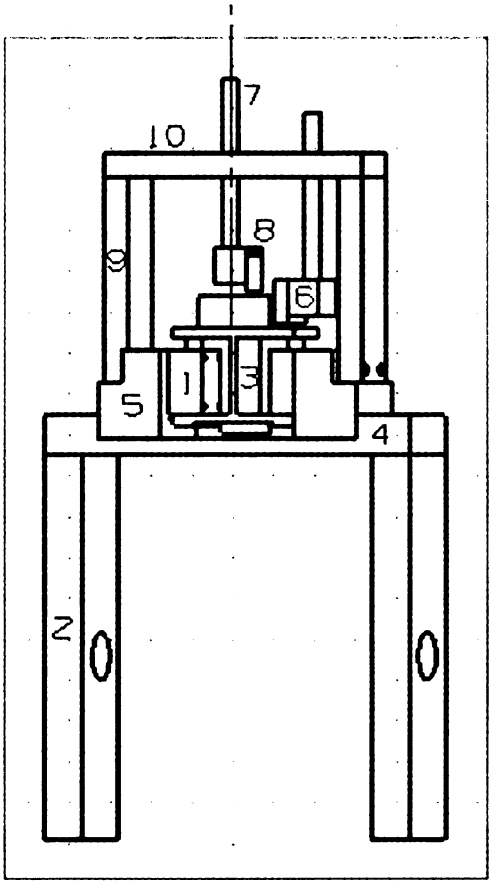

PC NO	PART NAME	QTY
10	CROSS_BAR	1
9	SUPPORT	2
8	LASER	2
7	LASER_SHAFT	2
6	L_BRACKET	2
5	V_BEARING_BLOCK	2
4	V_BEARING_SUPPORT	1
3	V_CART	1
2	LEG	2
1	BEARING_ASSEM	2

Figure (41) Vertical Mechanical Dilatational Test Assembly

Procured Equipment

1. Bearing assemblies are NewWay S301201 commercial air bearings including bushings and pillow blocks. Recommended air supply is 60 psi.

2. Laser distance sensors are Baumer electric OADM 12U6430/S35A with a resolution of up to 2μm. Connected to a National Instrument BNC-2120 board and PCI-6221 card.

Manufactured Parts

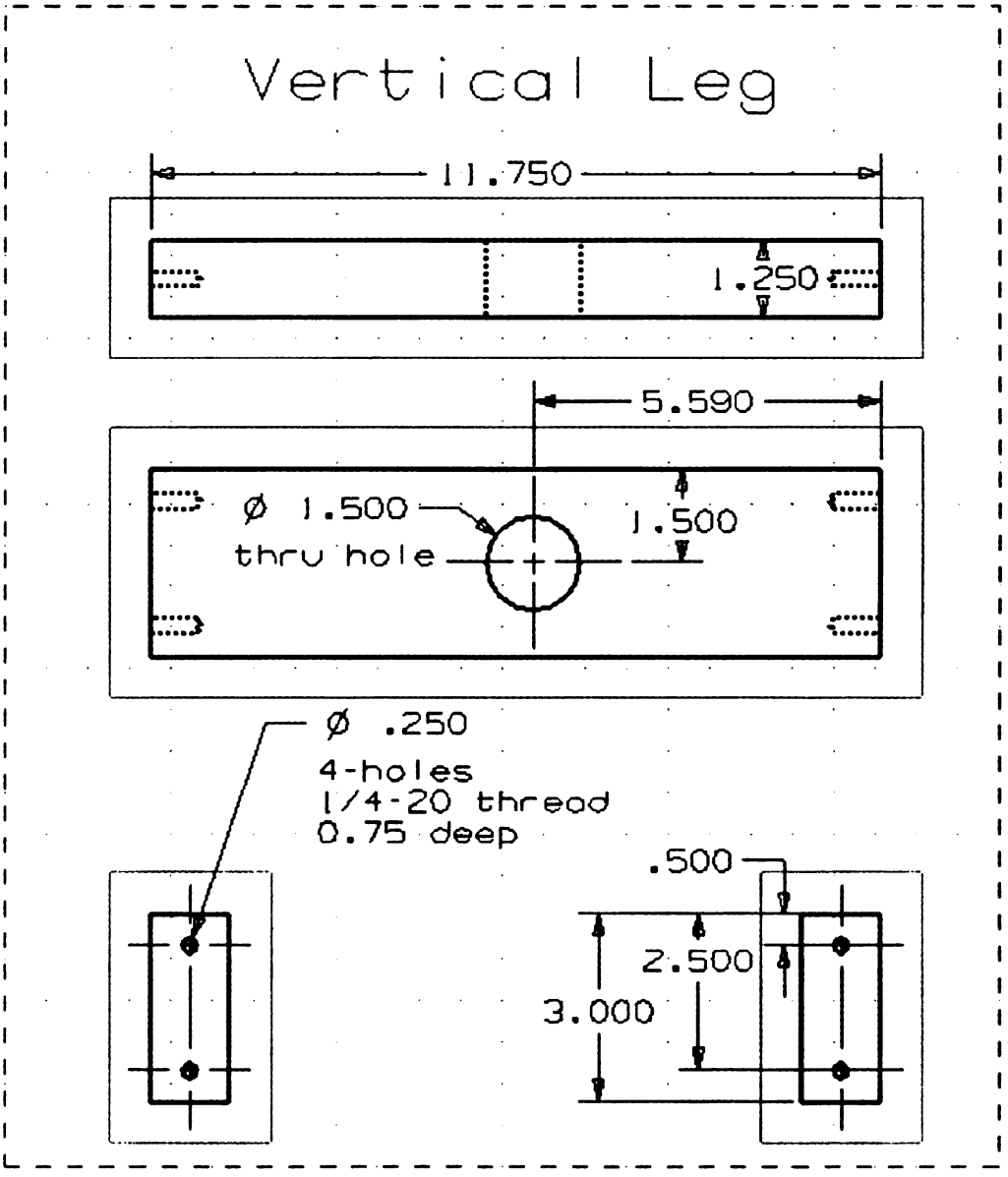

Figure (42) Specifications for Vertical Test Support Leg

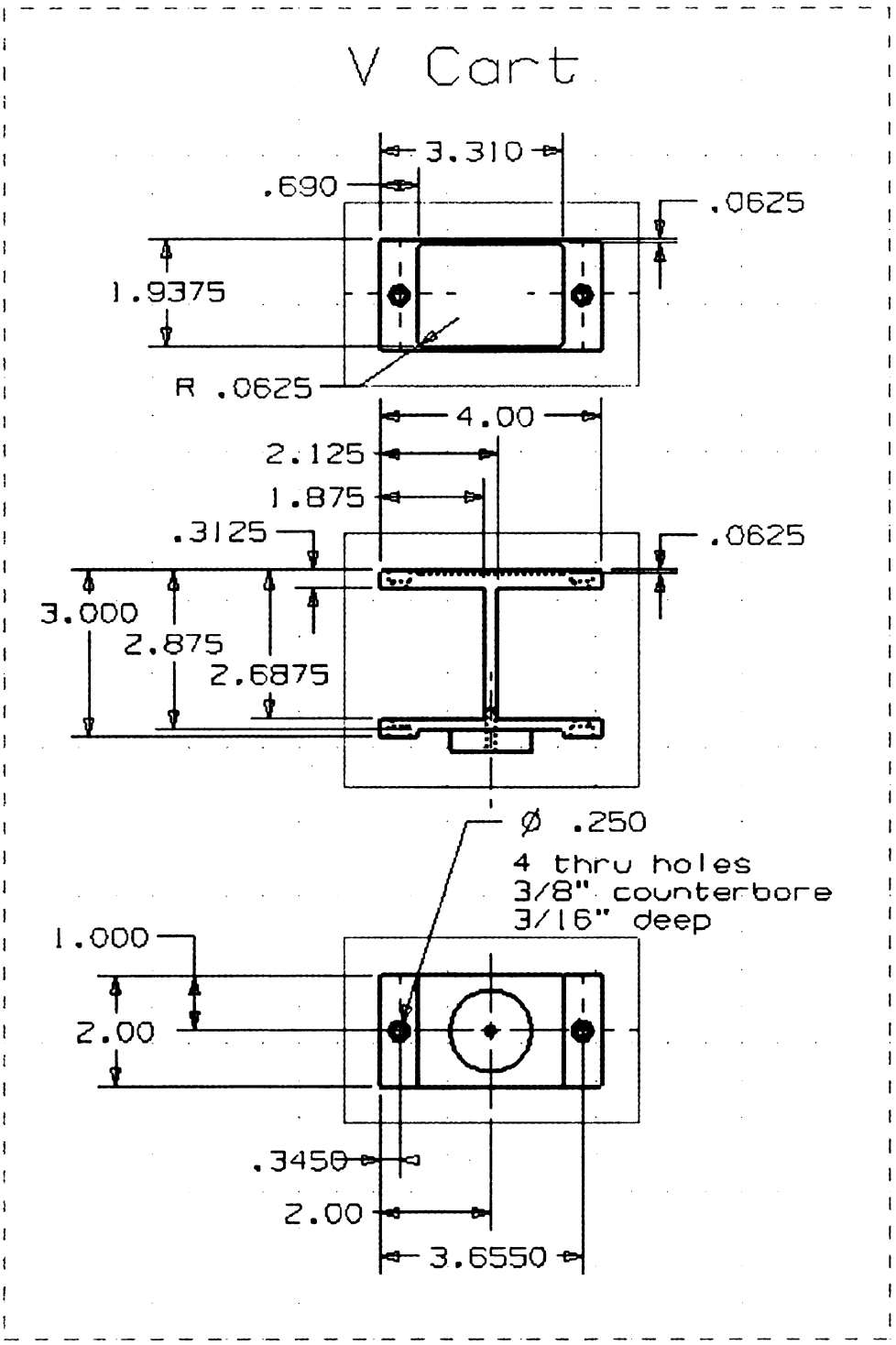

Figure (43) Specifications for Vertical Material Cart

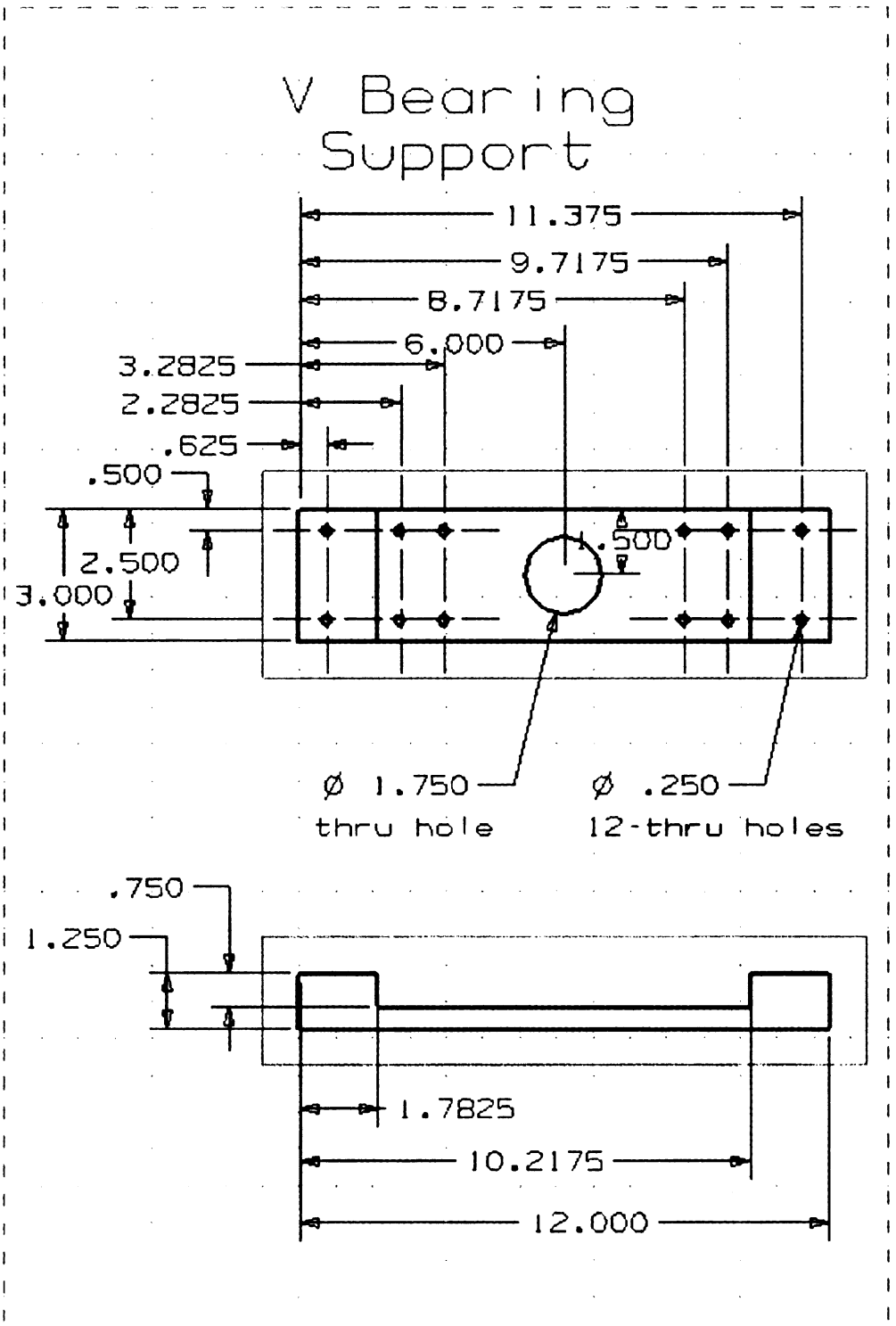

Figure (44) Specifications for Vertical Bearing Support

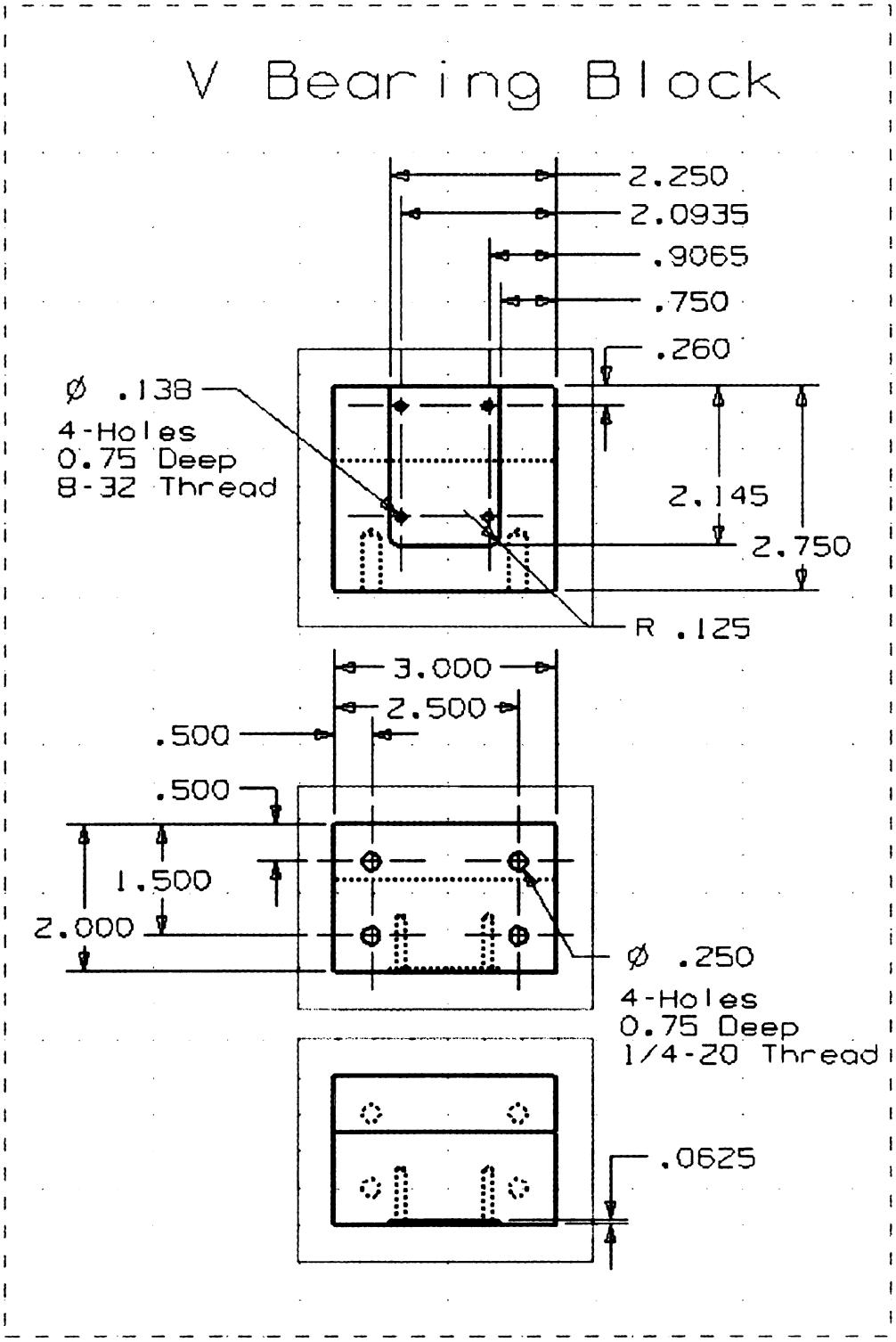

Figure (45) Specifications for Vertical Bearing Block

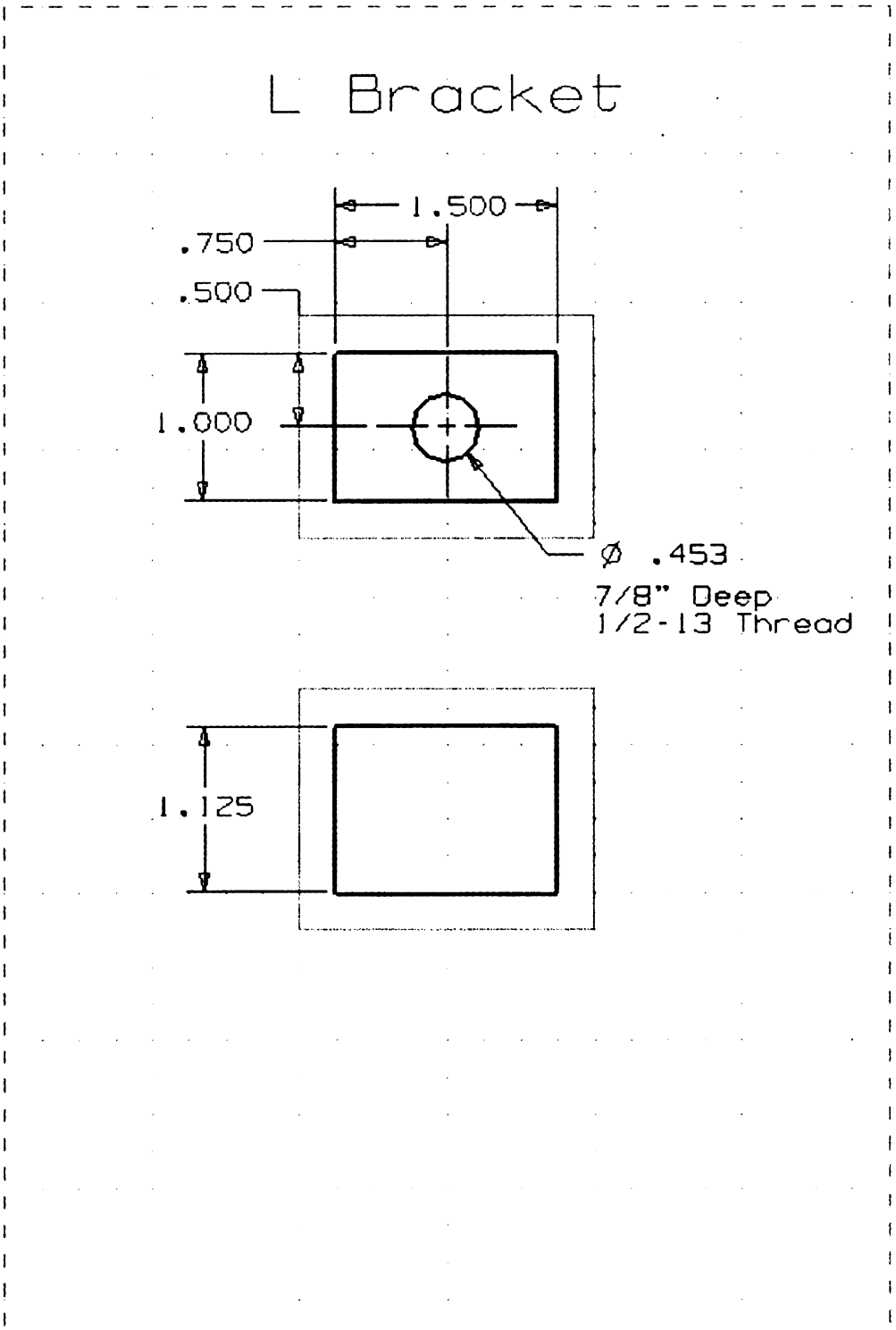

Figure (46) Specifications for Laser Bracket

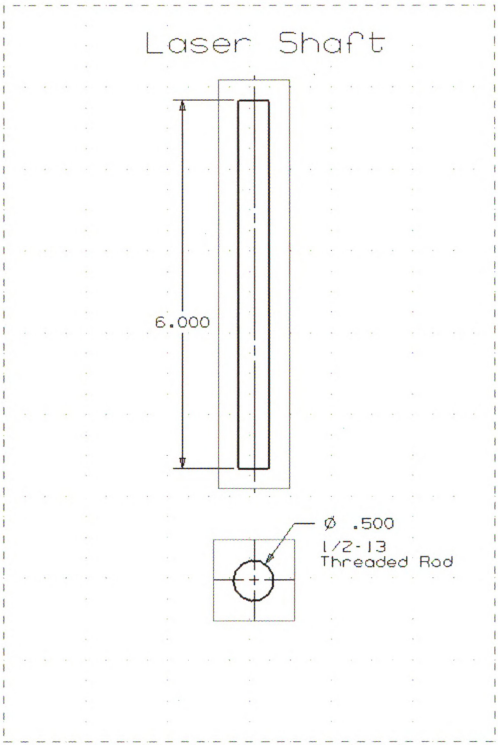

Figure (47) Specifications for Laser Adjustment Shaft

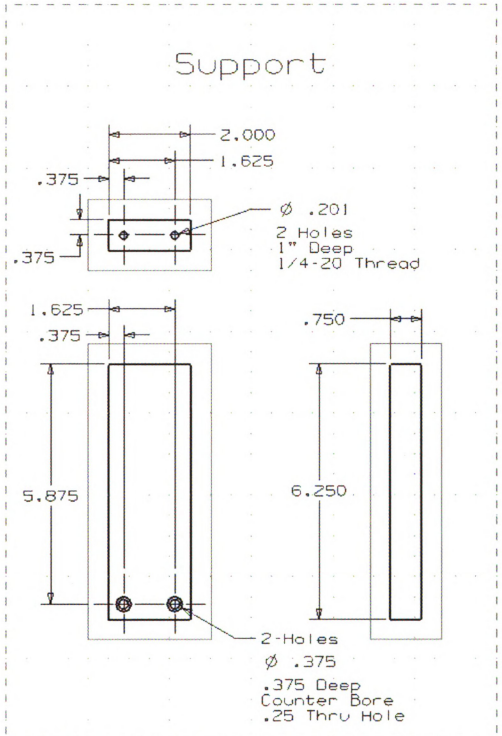

Figure (48) Specifications for Laser Measurement Vertical Support

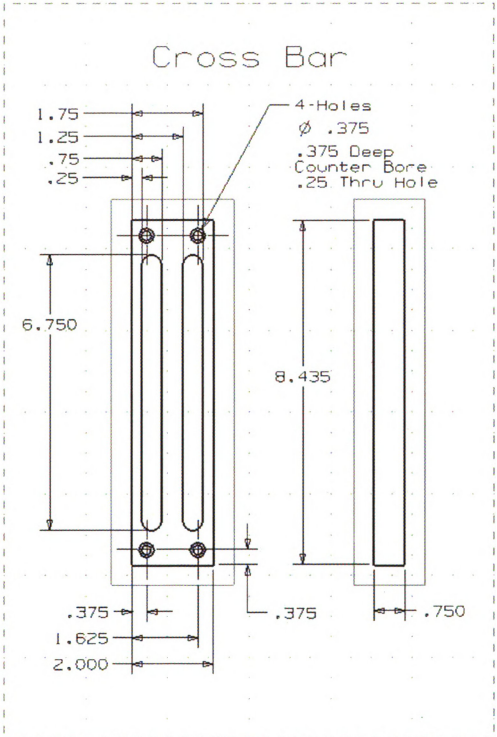

Figure (49) Specifications for Laser Measurement Horizontal Support

Software Developed in LabView 7.1

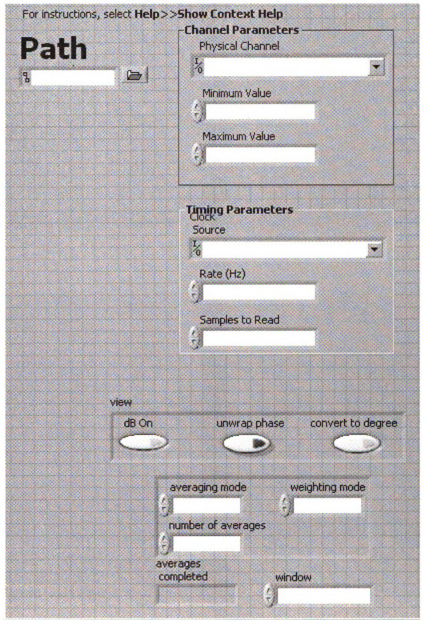

Figure (50) LabView Front Panel Inputs for Vertical Dilatational Test

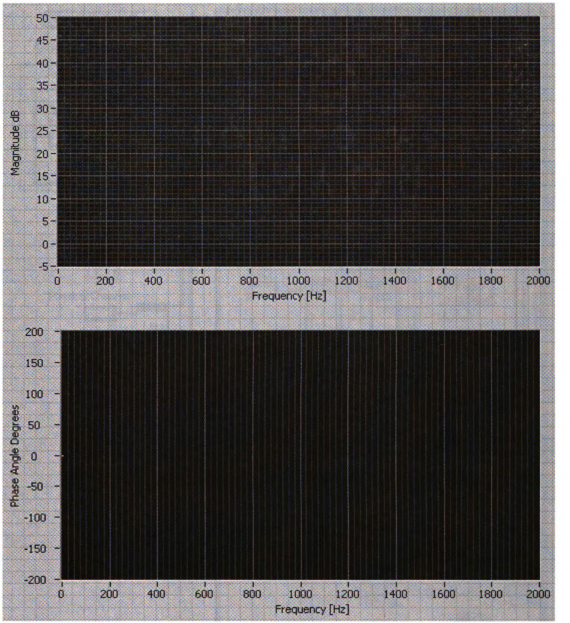

Figure (51) LabView Front Panel Outputs for Vertical Dilatational Test

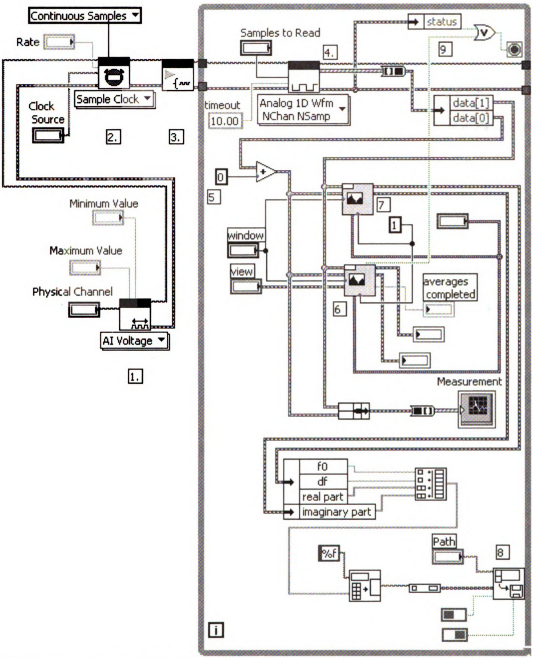

Steps:
1. Create an analog input voltage channel.
2. Define the parameters for an External Clock Source. Additionally, define the sample mode to be continuous.
3. Call the Start VI to start the acquisition.
4. Read the waveform data in a loop until the user hits the stop button or an error occurs.
5. Adjustment for voltage difference between lasers
6. Generates the Magnitude and Phase on Front Panel
7. Generates Real and Imaginary parts of Response function to Export to Excel
8. Saves Real and Imaginary Parts to .txt file path specified by Path on Front Panel
9. Ends loop when averages are completed
10. Call the Clear Task VI to clear the Task.
11. Use the popup dialog box to display an error if any.

Figure (52) LabView Block Diagram for Vertical Dilatational Test

APPENDIX B: Insertion Loss Broadside Equations

$$IL^B = \frac{2i\,\rho_f(\gamma\rho)^{-1}\alpha\cos(\alpha h) + \left[1 + \rho_f^2(\gamma\rho)^{-2}\alpha^2\right]\sin(\alpha h)}{2i\rho_f(\gamma\rho)^{-1}\alpha} \tag{B1}$$

To permit both the real and imaginary parts to be acquired, the modified dilatational wave propagation constant was split into real and imaginary parts as,

$$\alpha = \alpha_R + i\alpha_I \tag{B2}$$

where α_R is the real part of the modified dilatational wave propagation constant, and α_I is the imaginary part of the modified dilatational wave propagation constant. Substituting equation (B2) into the broadside insertion loss equation (B1) and utilizing the complex trigonometric identities [Potter, M., Goldberg, J., (1995)],

$$\sin(h\alpha_R + ih\alpha_I) = \sin(h\alpha_R)\cosh(h\alpha_I) + i\cos(h\alpha_R)\sinh(h\alpha_I) \tag{B3}$$

and

$$\cos(h\alpha_R + ih\alpha_I) = \cos(h\alpha_R)\cosh(h\alpha_I) - i\sin(h\alpha_R)\sinh(h\alpha_I) \tag{B4}$$

resulted in the complex broadside insertion loss equation,

$$\begin{aligned} IL(0,\omega) = {} & \frac{[2ip_1(\alpha_R + i\alpha_I)][\cos(h\alpha_R)\cosh(h\alpha_I) - i\sin(h\alpha_R)\sinh(h\alpha_I)]}{2ip_1(\alpha_R + i\alpha_I)} \\ & + \frac{[1 + p_2(\alpha_R + i\alpha_I)^2][\sin(h\alpha_R)\cosh(h\alpha_I) + i\cos(h\alpha_R)\sinh(h\alpha_I)]}{2ip_1(\alpha_R + i\alpha_I)} \end{aligned} \tag{B5}$$

with intermediate variables

$$p_1 = \rho_f(\gamma\rho)^{-1} \tag{B6}$$

and

$$p_2 = \rho_f^2(\gamma\rho)^{-2} \tag{B7}$$

Splitting equation (B5) into real and imaginary parts resulted in the split broadside insertion loss equation,

$$IL^B = \frac{IL_R^{BN} + iIL_I^{BN}}{IL_R^{BD} + iIL_I^{BD}} \tag{B8}$$

where the N, D, R, and I superscripts represent the numerator, denominator, real, and imaginary respectively. The split broadside insertion loss numerator consisted of the real part,

$$\begin{aligned} IL_R^{BN} = {} & [2p_1\alpha_R \sin(h\alpha_R)\sinh(h\alpha_I) - 2p_1\alpha_I \cos(h\alpha_R)\cosh(h\alpha_I)] \\ & + [(1 + p_2\alpha_R^2 - P_2\alpha_I^2)\sin(h\alpha_R)\cosh(h\alpha_I) \\ & - 2p_2\alpha_R\alpha_I \cos(h\alpha_R)\sinh(h\alpha_I)] \end{aligned} \tag{B9}$$

$$\begin{aligned} IL_I^{BN} = {} & [2p_1\alpha_R \cos(h\alpha_R)\cosh(h\alpha_I) + 2p_1\alpha_I \sin(h\alpha_R)\sinh(h\alpha_I)] \\ & + [(1 + p_2\alpha_R^2 - p_2\alpha_I^2)\cos(h\alpha_R)\sinh(h\alpha_I) \\ & + 2p_2\alpha_R\alpha_I \sin(h\alpha_R)\cosh(h\alpha_I)] \end{aligned} \tag{B10}$$

The split broadside insertion loss denominator consisted of the real part,

$$IL_R^D = -2p_1\alpha_I \tag{B11}$$

and the imaginary part,

$$IL_I^D = 2p_1\alpha_R \tag{B12}$$

Having the numerator and denominator of the split broadside insertion loss equation (B8) allows for the separation of the real and imaginary parts as,

$$IL^B = IL_R^B + iIL_I^B \tag{B13}$$

with the real part being

$$IL_R^B = \frac{(IL_R^{BN})(IL_R^{BD}) + (IL_I^{BN})(IL_I^{BD})}{(IL_R^{BD})^2 + (IL_I^{BD})^2} \tag{B14}$$

and the imaginary part being

$$IL_I^B = \frac{(IL_I^{BN})(IL_R^{BD}) - (IL_R^{BN})(IL_I^{BD})}{(IL_R^{BD})^2 + (IL_I^{BD})^2} \tag{B15}$$

APPENDIX C: Newton-Raphson Partial Derivatives for Broadside Excitation

Insertion loss

$$\frac{\partial IL_R}{\partial \alpha_R} = \frac{(-2p_1\alpha_R f_1)(c*ch) - (\alpha_R^2 f_2)(c*sh) - (\alpha_I \alpha_R f_3)(s*ch)}{p_1(f_1)^2}$$

$$+ \frac{(4p_1\alpha_R + \alpha_I h f_3)(c*ch) + (2\alpha_I\alpha_R p_2 - 2hp_1 f_1)(s*ch)}{2p_1 f_1} \quad \text{(C-1)}$$

$$+ \frac{+(2p_2\alpha_R^2 + f_2)(c*sh) - \alpha_R h f_2 (s*sh)}{2p_1 f_1}$$

$$\frac{\partial IL_R}{\partial \alpha_I} = \frac{(-2p_1\alpha_I f_1)(c*ch) - (\alpha_I \alpha_R f_2)(c*sh) - (\alpha_I^2 f_3)(s*ch)}{p_1(f_1)^2}$$

$$+ \frac{(4p_1\alpha_I + \alpha_R h f_2)(c*ch) + (2p_2\alpha_I^2 + f_3)(s*ch)}{2p_1 f_1} \quad \text{(C-2)}$$

$$+ \frac{+(2\alpha_I\alpha_R p_2 + 2hp_1 f_1)(c*sh) - \alpha_I h f_2 (s*sh)}{2p_1 f_1}$$

$$\frac{\partial IL_I}{\partial \alpha_R} = -\frac{\partial IL_R}{\partial \alpha_I} \quad \text{(C-3)}$$

$$\frac{\partial IL_I}{\partial \alpha_I} = \frac{\partial IL_R}{\partial \alpha_R} \quad \text{(C-4)}$$

Echo Reduction

$$\frac{\partial ER_R}{\partial \alpha_R} = \frac{4p_2\alpha_R f_3[f_2 f_3(c_2 - ch_2) - 2p_1\alpha_I f_2(s_2) - 2p_1\alpha_R f_3(sh_2)]}{(c_2 - ch_2)f_2^4}$$

$$+ \frac{+(4\alpha_I\alpha_R p_1 p_2 + 4hf_3)(s_2) + 2p_1(f_3 + 2p_2\alpha_R^2)(sh_2)}{(c_2 - ch_2)f_2^2} \quad \text{(C-5)}$$

$$+ \frac{4p_1\alpha_I h f_2(c_2) + (4p_2^2\alpha_R f_1)(ch_2 - c_2)}{(c_2 - ch_2)f_2^2}$$

$$+ \frac{4hp_1[\alpha_I f_2(s_2^2) + \alpha_R f_3(s_2 * sh_2)]}{(c_2 - ch_2)^2 f_2^2}$$

$$\frac{\partial ER_R}{\partial \alpha_I} = \frac{4p_2\alpha_I f_2[f_2 f_3(c_2 - ch_2) - 2p_1\alpha_I f_2(s_2) - 2p_1\alpha_R f_3(sh_2)]}{(c_2 - ch_2)f_2^4}$$

$$+\frac{4p_1\alpha_R h f_3(ch_2) - (4p_2^2\alpha_I f_1)(c_2 + ch_2) + (4\alpha_I\alpha_R p_1 p_2)(sh_2)}{(c - ch)f_2^2} \quad \text{(C-6)}$$

$$+\frac{+2p_1(f_2 + 2p_2\alpha_I^2)(s_2)}{(c - ch)f_2^2} + \frac{4hp_1[\alpha_R f_3(sh_2^2) + \alpha_I f_2(s_2 * sh_2)]}{(c - ch)^2 f_2^2}$$

$$\frac{\partial ER_I}{\partial \alpha_R} = -\frac{\partial ER_R}{\partial \alpha_I} \quad \text{(C-7)}$$

$$\frac{\partial ER_I}{\partial \alpha_I} = \frac{\partial ER_R}{\partial \alpha_R} \quad \text{(C-8)}$$

$$p_1 = \rho_f(\gamma\rho)^{-1} \quad \text{(C-9)}$$

$$p_2 = \rho_f(\gamma\rho)^{-2} \quad \text{(C-10)}$$

$$f_1 = \alpha_I^2 + \alpha_R^2 \quad \text{(C-11)}$$

$$f_2 = p_2(\alpha_I^2 + \alpha_R^2) + 1 \quad \text{(C-12)}$$

$$f_3 = p_2(\alpha_I^2 + \alpha_R^2) - 1 \quad \text{(C-13)}$$

$$c = \cos(\alpha_R h) \quad \text{(C-14)}$$

$$ch = \cosh(\alpha_I h) \quad \text{(C-15)}$$

$$s = \sin(\alpha_R h) \quad \text{(C-16)}$$

$$sh = \sinh(\alpha_I h) \quad \text{(C-17)}$$

$$c_2 = \cos(2\alpha_R h) \quad \text{(C-18)}$$

$$ch_2 = \cosh(2\alpha_I h) \quad \text{(C-19)}$$

$$s_2 = \sin(2\alpha_R h) \quad \text{(C-20)}$$

$$sh_2 = \sinh(2\alpha_I h) \quad \text{(C-21)}$$

APPENDIX D: Real and Imaginary Parts for Echo Reduction and Insertion Loss

Real and imaginary parts of the full echo reduction and insertion loss equations were calculated using Matlab and are shown below. The partial derivatives of both parts with respect to aR, bR, aI, and bI were used in the Newton Raphson method.

Full Echo Reduction = ((8*aR+8*i*aI)*(bR+i*bI)*kx^2*((bR+i*bI)^2-kx^2)^2*(1-cos((aR+i*aI)*h)*cos((bR+i*bI)*h))+(((bR+i*bI)^2-kx^2)^4+16*(aR+i*aI)^2*(bR+i*bI)^2*kx^4-p2*(aR+i*aI)^2*((bR+i*bI)^2+kx^2)^4)*sin((aR+i*aI)*h)*sin((bR+i*bI)*h))/((8*aR+8*i*aI)*(bR+i*bI)*kx^2*((bR+i*bI)^2-kx^2)^2*(1-cos((aR+i*aI)*h)*cos((bR+i*bI)*h))+2*i*p1*(aR+i*aI)*((bR+i*bI)^2-kx^2)^2*((bR+i*bI)^2+kx^2)^2*cos((aR+i*aI)*h)*sin((bR+i*bI)*h)+8*i*p1*(aR+i*aI)^2*(bR+i*bI)*kx^2*((bR+i*bI)^2+kx^2)^2*sin((aR+i*aI)*h)*cos((bR+i*bI)*h)+(((bR+i*bI)^2-kx^2)^4+16*(aR+i*aI)^2*(bR+i*bI)^2*kx^4+p2*(aR+i*aI)^2*((bR+i*bI)^2+kx^2)^4)*sin((aR+i*aI)*h)*sin((bR+i*bI)*h))

Real Part of Echo Reduction = 1/2*((8*aR+8*i*aI)*(bR+i*bI)*kx^2*((bR+i*bI)^2-kx^2)^2*(1-cos((aR+i*aI)*h)*cos((bR+i*bI)*h))+(((bR+i*bI)^2-kx^2)^4+16*(aR+i*aI)^2*(bR+i*bI)^2*kx^4-p2*(aR+i*aI)^2*((bR+i*bI)^2+kx^2)^4)*sin((aR+i*aI)*h)*sin((bR+i*bI)*h))/((8*aR+8*i*aI)*(bR+i*bI)*kx^2*((bR+i*bI)^2-kx^2)^2*(1-cos((aR+i*aI)*h)*cos((bR+i*bI)*h))+2*i*p1*(aR+i*aI)*((bR+i*bI)^2-kx^2)^2*((bR+i*bI)^2+kx^2)^2*cos((aR+i*aI)*h)*sin((bR+i*bI)*h)+8*i*p1*(aR+i*aI)^2*(bR+i*bI)*kx^2*((bR+i*bI)^2+kx^2)^2*sin((aR+i*aI)*h)*cos((bR+i*bI)*h)+(((bR+i*bI)^2-kx^2)^4+16*(aR+i*aI)^2*(bR+i*bI)^2*kx^4+p2*(aR+i*aI)^2*((bR+i*bI)^2+kx^2)^4)*sin((aR+i*aI)*h)*sin((bR+i*bI)*h))+1/2*((8*aR-8*i*aI)*(bR-i*bI)*kx^2*((bR-i*bI)^2-kx^2)^2*(1-cos((aR-i*aI)*h)*cos((bR-i*bI)*h))+(((bR-i*bI)^2-kx^2)^4+16*(aR-i*aI)^2*(bR-i*bI)^2*kx^4-p2*(aR-i*aI)^2*((bR-i*bI)^2+kx^2)^4)*sin((aR-i*aI)*h)*sin((bR-i*bI)*h))/((8*aR-8*i*aI)*(bR-i*bI)*kx^2*((bR-i*bI)^2-kx^2)^2*(1-cos((aR-i*aI)*h)*cos((bR-i*bI)*h))-2*i*p1*(aR-i*aI)*((bR-i*bI)^2-kx^2)^2*((bR-i*bI)^2+kx^2)^2*cos((aR-i*aI)*h)*sin((bR-i*bI)*h)-8*i*p1*(aR-i*aI)^2*(bR-i*bI)*kx^2*((bR-i*bI)^2+kx^2)^2*sin((aR-i*aI)*h)*cos((bR-i*bI)*h)+(((bR-i*bI)^2-kx^2)^4+16*(aR-i*aI)^2*(bR-i*bI)^2*kx^4+p2*(aR-i*aI)^2*((bR-i*bI)^2+kx^2)^4)*sin((aR-i*aI)*h)*sin((bR-i*bI)*h))

Imaginary Part of Echo Reduction = -1/2*i*(((8*aR+8*i*aI)*(bR+i*bI)*kx^2*((bR+i*bI)^2-kx^2)^2*(1-cos((aR+i*aI)*h)*cos((bR+i*bI)*h))+(((bR+i*bI)^2-kx^2)^4+16*(aR+i*aI)^2*(bR+i*bI)^2*kx^4-p2*(aR+i*aI)^2*((bR+i*bI)^2+kx^2)^4)*sin((aR+i*aI)*h)*sin((bR+i*bI)*h))/((8*aR+8*i*aI)*(bR+i*bI)*kx^2*((bR+i*bI)^2-kx^2)^2*(1-cos((aR+i*aI)*h)*cos((bR+i*bI)*h))+2*i*p1*(aR+i*aI)*((bR+i*bI)^2-kx^2)^2*((bR+i*bI)^2+kx^2)^2*cos((aR+i*aI)*h)*sin((bR+i*bI)*h)+8*i*p1*(aR+i*aI)^2*(bR+i*bI)*kx^2*((bR+i*bI)^2+kx^2)^2*sin((aR+i*aI)*h)*cos((bR+i*bI)*h)+(((bR+i*bI)^2-kx^2)^4+16*(aR+i*aI)^2*(bR+i*bI)^2*kx^4+p2*(aR+i*aI)^2*((bR+i*bI)^2+kx^2)^4)*sin((aR+i*aI)*h)*sin((bR+i*bI)*h))-((8*aR-8*i*aI)*(bR-i*bI)*kx^2*((bR-i*bI)^2-kx^2)^2*(1-cos((aR-i*aI)*h)*cos((bR-i*bI)*h))+(((bR-i*bI)^2-kx^2)^4+16*(aR-i*aI)^2*(bR-i*bI)^2*kx^4-p2*(aR-i*aI)^2*((bR-i*bI)^2+kx^2)^4)*sin((aR-i*aI)*h)*sin((bR-i*bI)*h))/((8*aR-8*i*aI)*(bR-i*bI)*kx^2*((bR-i*bI)^2-kx^2)^2*(1-cos((aR-i*aI)*h)*cos((bR-i*bI)*h))-2*i*p1*(aR-i*aI)*((bR-i*bI)^2-kx^2)^2*((bR-i*bI)^2+kx^2)^2*cos((aR-i*aI)*h)*sin((bR-i*bI)*h)-8*i*p1*(aR-i*aI)^2*(bR-i*bI)*kx^2*((bR-i*bI)^2+kx^2)^2*sin((aR-i*aI)*h)*cos((bR-i*bI)*h)+(((bR-i*bI)^2-kx^2)^4+16*(aR-i*aI)^2*(bR-i*bI)^2*kx^4+p2*(aR-i*aI)^2*((bR-i*bI)^2+kx^2)^4)*sin((aR-i*aI)*h)*sin((bR-i*bI)*h)))

Full Insertion Loss = (8*i*p1*(aR+i*aI)^2*(bR+i*bI)*kx^2*((bR+i*bI)^2+kx^2)^2*sin((aR+i*aI)*h)+2*i*p1*(aR+i*aI)*((bR+i*bI)^2-kx^2)^2*((bR+i*bI)^2+kx^2)^2*sin((bR+i*bI)*h))/((8*aR+8*i*aI)*(bR+i*bI)*kx^2*((bR+i*bI)^2-kx^2)^2*(1-cos((aR+i*aI)*h)*cos((bR+i*bI)*h))+2*i*p1*(aR+i*aI)*((bR+i*bI)^2-kx^2)^2*((bR+i*bI)^2+kx^2)^2*cos((aR+i*aI)*h)*sin((bR+i*bI)*h)+8*i*p1*(aR+i*aI)^2*(bR+i*bI)*kx^2*((bR+i*bI)^2+kx^2)^2*sin((aR+i*aI)*h)*cos((bR+i*bI)*h)+(((bR+i*bI)^2-kx^2)^4+16*(aR+i*aI)^2*(bR+i*bI)^2*kx^4+p2*(aR+i*aI)^2*((bR+i*bI)^2+kx^2)^4)*sin((aR+i*aI)*h)*sin((bR+i*bI)*h))

Real Part of Insertion Loss = 1/2*(8*i*p1*(aR+i*aI)^2*(bR+i*bI)*kx^2*((bR+i*bI)^2+kx^2)^2*sin((aR+i*aI)*h)+2*i*p1*(aR+i*aI)*((bR+i*bI)^2-kx^2)^2*((bR+i*bI)^2+kx^2)^2*sin((bR+i*bI)*h))/((8*aR+8*i*aI)*(bR+i*bI)*kx^2*((bR+i*bI)^2-kx^2)^2*(1-cos((aR+i*aI)*h)*cos((bR+i*bI)*h))+2*i*p1*(aR+i*aI)*((bR+i*bI)^2-kx^2)^2*((bR+i*bI)^2+kx^2)^2*cos((aR+i*aI)*h)*sin((bR+i*bI)*h)+8*i*p1*(aR+i*aI)^2*(bR+i*bI)*kx^2*((bR+i*bI)^2+kx^2)^2*sin((aR+i*aI)*h)*cos((bR+i*bI)*h)+(((bR+i*bI)^2-kx^2)^4+16*(aR+i*aI)^2*(bR+i*bI)^2*kx^4+p2*(aR+i*aI)^2*((bR+i*bI)^2+kx^2)^4)*sin((aR+i*aI)*h)*sin((bR+i*bI)*h))+1/2*(-8*i*p1*(aR-i*aI)^2*(bR-i*bI)*kx^2*((bR-i*bI)^2+kx^2)^2*sin((aR-i*aI)*h)-2*i*p1*(aR-i*aI)*((bR-i*bI)^2-

kx^2)^2*((bR-i*bI)^2+kx^2)^2*sin((bR-i*bI)*h))/((8*aR-8*i*aI)*(bR-i*bI)*kx^2*((bR-i*bI)^2-kx^2)^2*(1-cos((aR-i*aI)*h)*cos((bR-i*bI)*h))-2*i*p1*(aR-i*aI)*((bR-i*bI)^2-kx^2)^2*((bR-i*bI)^2+kx^2)^2*cos((aR-i*aI)*h)*sin((bR-i*bI)*h)-8*i*p1*(aR-i*aI)^2*(bR-i*bI)*kx^2*((bR-i*bI)^2+kx^2)^2*sin((aR-i*aI)*h)*cos((bR-i*bI)*h)+(((bR-i*bI)^2-kx^2)^4+16*(aR-i*aI)^2*(bR-i*bI)^2*kx^4+p2*(aR-i*aI)^2*((bR-i*bI)^2+kx^2)^4)*sin((aR-i*aI)*h)*sin((bR-i*bI)*h))

Imaginary Part of Insertion Loss = -1/2*i*((8*i*p1*(aR+i*aI)^2*(bR+i*bI)*kx^2*((bR+i*bI)^2+kx^2)^2*sin((aR+i*aI)*h)+2*i*p1*(aR+i*aI)*((bR+i*bI)^2-kx^2)^2*((bR+i*bI)^2+kx^2)^2*sin((bR+i*bI)*h))/((8*aR+8*i*aI)*(bR+i*bI)*kx^2*((bR+i*bI)^2-kx^2)^2*(1-cos((aR+i*aI)*h)*cos((bR+i*bI)*h))+2*i*p1*(aR+i*aI)*((bR+i*bI)^2-kx^2)^2*((bR+i*bI)^2+kx^2)^2*cos((aR+i*aI)*h)*sin((bR+i*bI)*h)+8*i*p1*(aR+i*aI)^2*(bR+i*bI)*kx^2*((bR+i*bI)^2+kx^2)^2*sin((aR+i*aI)*h)*cos((bR+i*bI)*h)+(((bR+i*bI)^2-kx^2)^4+16*(aR+i*aI)^2*(bR+i*bI)^2*kx^4+p2*(aR+i*aI)^2*((bR+i*bI)^2+kx^2)^4)*sin((aR+i*aI)*h)*sin((bR+i*bI)*h))-(-8*i*p1*(aR-i*aI)^2*(bR-i*bI)*kx^2*((bR-i*bI)^2+kx^2)^2*sin((aR-i*aI)*h)-2*i*p1*(aR-i*aI)*((bR-i*bI)^2-kx^2)^2*((bR-i*bI)^2+kx^2)^2*sin((bR-i*bI)*h))/((8*aR-8*i*aI)*(bR-i*bI)*kx^2*((bR-i*bI)^2-kx^2)^2*(1-cos((aR-i*aI)*h)*cos((bR-i*bI)*h))-2*i*p1*(aR-i*aI)*((bR-i*bI)^2-kx^2)^2*((bR-i*bI)^2+kx^2)^2*cos((aR-i*aI)*h)*sin((bR-i*bI)*h)-8*i*p1*(aR-i*aI)^2*(bR-i*bI)*kx^2*((bR-i*bI)^2+kx^2)^2*sin((aR-i*aI)*h)*cos((bR-i*bI)*h)+(((bR-i*bI)^2-kx^2)^4+16*(aR-i*aI)^2*(bR-i*bI)^2*kx^4+p2*(aR-i*aI)^2*((bR-i*bI)^2+kx^2)^4)*sin((aR-i*aI)*h)*sin((bR-i*bI)*h)))

APPENDIX E: Numerical Example for Broadside Insertion Loss

The following is a numerical example used to demonstrate the broadside method using the insertion loss equations. The material in this example is assumed to have a density of 1400 (kg/m^3), be 0.0381 (m) thick and have a complex dilatational wavespeed in (m/s) defined as,

$$c_d = 1500 + 25i \ (^m/_s) \qquad \textbf{(E-1)}$$

The fluid the material is submerged in is assumed to be fresh water with a density of 1000 (kg/m^3), and a compressional wavespeed of 1467.5 (m/s). The assumed values were then inserted into the forward model to generate an original insertion loss response as shown in Figure 53.

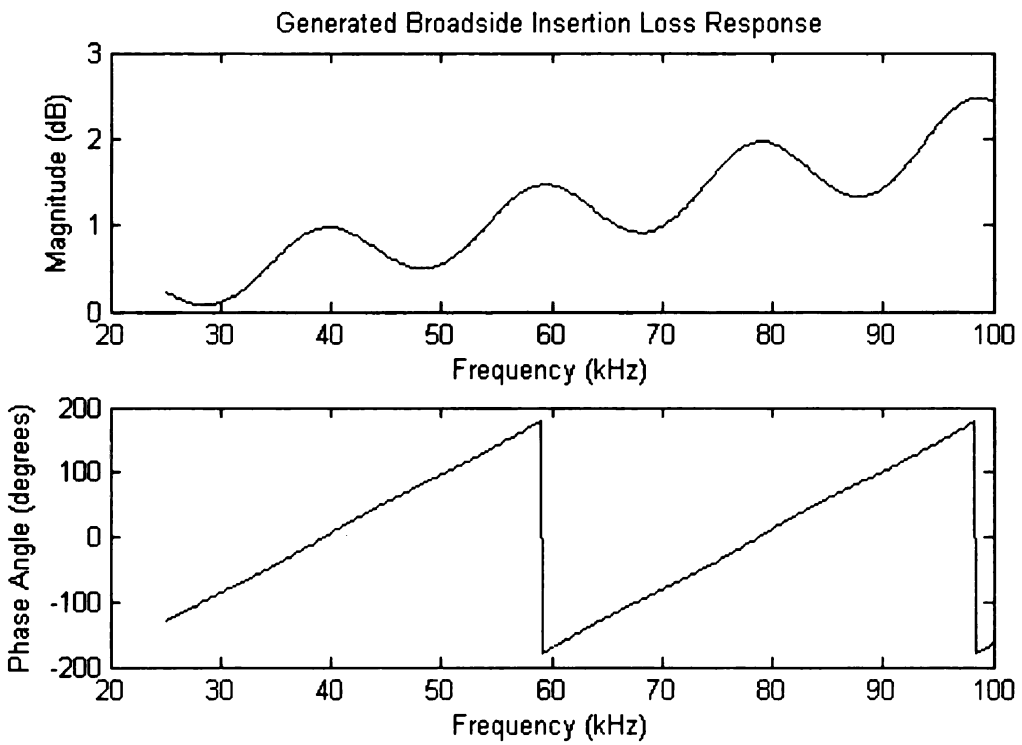

Figure (53) Generated Broadside Insertion Loss Response

The response was then used as the input to the inverse method to estimate the complex dilatational wavespeed. The inverse method recovered the complex dilatational wavespeed used to produce the original insertion loss response. The original broadside insertion loss and

the predicted broadside insertion loss using the calculated complex dilatational wavespeeds are shown in Fig. 7, the two graphs match providing evidence that the developed inverse program is running correctly. To strengthen that statement the predicted complex dilatational wavespeeds were plotted and then compared to the defined wavespeeds used to generate the original insertion loss as shown in Figure 54.

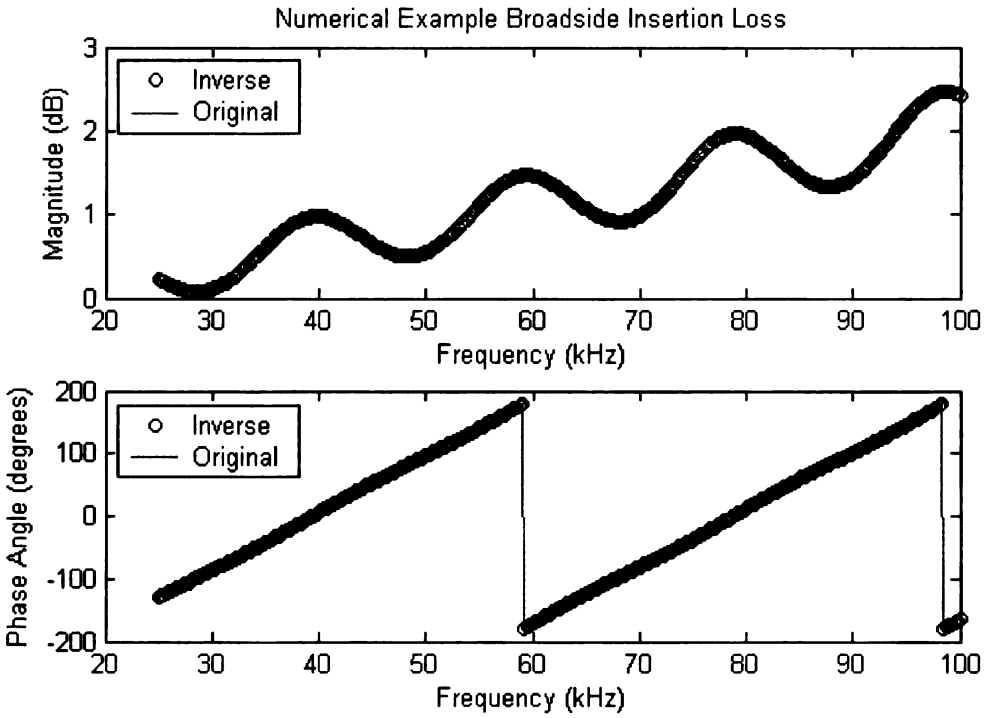

Figure (54) Inverse Predicted and Original Broadside Insertion Loss

APPENDIX F: Matlab Code and ATF Data

Table 3. Broadside Echo Reduction ATF Data (3140)

Frequency	Echo Reduction
25000	0.0004898 + 0.046771i
25250	0.015574 + 0.032798i
25500	0.018476 + 0.034748i
25750	0.021648 + 0.03451i
26000	0.024317 + 0.035648i
26250	0.027891 + 0.036879i
26500	0.030287 + 0.036351i
26750	0.03386 + 0.036951i
27000	0.036544 + 0.038509i
27250	0.038814 + 0.038009i
27500	0.041051 + 0.037485i
27750	0.043429 + 0.037752i
28000	0.045764 + 0.038129i
28250	0.049584 + 0.039019i
28500	0.051428 + 0.039036i
28750	0.054904 + 0.039452i
29000	0.058088 + 0.039033i
29250	0.061166 + 0.038817i
29500	0.065226 + 0.038729i
29750	0.069741 + 0.038024i
30000	0.073132 + 0.037585i
30250	0.069281 + 0.028697i
30500	0.07197 + 0.026623i
30750	0.075328 + 0.025204i
31000	0.077162 + 0.022418i
31250	0.079004 + 0.019113i
31500	0.082508 + 0.016487i
31750	0.084157 + 0.012728i
32000	0.086554 + 0.0097085i
32250	0.087833 + 0.0069126i
32500	0.088051 + 0.0030748i
32750	0.089123 - 0.00062221i
33000	0.088949 - 0.0055962i
33250	0.089595 - 0.01005i
33500	0.087825 - 0.01517i
33750	0.087177 - 0.01853i
34000	0.087666 - 0.021047i
34250	0.087592 - 0.021353i
34500	0.087969 - 0.024066i
34750	0.088412 - 0.026357i
35000	0.088606 - 0.029303i
35250	0.084116 - 0.029457i
35500	0.082087 - 0.032004i
35750	0.08035 - 0.033611i
36000	0.079442 - 0.035703i
36250	0.078546 - 0.037633i
36500	0.076715 - 0.039088i
36750	0.074941 - 0.040351i
37000	0.074863 - 0.042528i
37250	0.07197 - 0.043587i
37500	0.071624 - 0.045982i
37750	0.070145 - 0.048209i
38000	0.068157 - 0.049337i
38250	0.066752 - 0.051221i
38500	0.065111 - 0.053292i
38750	0.062964 - 0.054349i
39000	0.061226 - 0.0563i
39250	0.059529 - 0.058092i
39500	0.056054 - 0.058863i
39750	0.053966 - 0.060783i
40000	0.051002 - 0.062091i
40250	0.047915 - 0.063354i
40500	0.045487 - 0.064007i
40750	0.042277 - 0.065102i
41000	0.0386 - 0.066321i
41250	0.03509 - 0.066273i
41500	0.030971 - 0.066416i
41750	0.027372 - 0.067073i
42000	0.023476 - 0.065929i
42250	0.01931 - 0.065609i
42500	0.015579 - 0.063428i
42750	0.011607 - 0.062019i
43000	0.0077607 - 0.059754i
43250	0.0041619 - 0.058061i
43500	0.00028444 - 0.054324i

Table 3. (cont'd)

43750	-0.0031309 - 0.05119i
44000	-0.0058167 - 0.048067i
44250	-0.0082934 - 0.043892i
44500	-0.010338 - 0.039405i
44750	-0.011973 - 0.035171i
45000	-0.013571 - 0.030624i
45250	-0.014428 - 0.026136i
45500	-0.014765 - 0.021403i
45750	-0.014314 - 0.016879i
46000	-0.014402 - 0.012476i
46250	-0.013262 - 0.0080002i
46500	-0.011957 - 0.0034512i
46750	-0.010213 + 0.00064253i
47000	-0.0082778 + 0.0040732i
47250	-0.0059741 + 0.0075918i
47500	-0.0038388 + 0.010962i
47750	-0.0005236 + 0.014279i
48000	0.0023655 + 0.016621i
48250	0.0056963 + 0.019607i
48500	0.0086677 + 0.021781i
48750	0.011914 + 0.023791i
49000	0.015062 + 0.025776i
49250	0.018514 + 0.02654i
49500	0.022392 + 0.02805i
49750	0.026083 + 0.028866i
50000	0.029426 + 0.029529i
50250	0.033299 + 0.029773i
50500	0.036092 + 0.029752i
50750	0.039516 + 0.029886i
51000	0.043061 + 0.028936i
51250	0.046451 + 0.029365i
51500	0.050133 + 0.028249i
51750	0.053215 + 0.026764i
52000	0.055882 + 0.026058i
52250	0.059694 + 0.024604i
52500	0.061966 + 0.022922i
52750	0.064781 + 0.021927i
53000	0.066997 + 0.020228i
53250	0.070884 + 0.018596i
53500	0.072346 + 0.016171i
53750	0.076325 + 0.014146i
54000	0.077641 + 0.011742i
54250	0.078874 + 0.0094052i
54500	0.081936 + 0.0068803i
54750	0.08307 + 0.0042081i
55000	0.086089 + 0.0013524i
55250	0.08708 - 0.001672i
55500	0.088995 - 0.0048198i
55750	0.0898 - 0.0080145i
56000	0.090502 - 0.011273i
56250	0.092151 - 0.01476i
56500	0.092734 - 0.01769i
56750	0.092023 - 0.021076i
57000	0.094438 - 0.025128i
57250	0.093553 - 0.028245i
57500	0.093692 - 0.031531i
57750	0.093295 - 0.036i
58000	0.093047 - 0.039688i
58250	0.091605 - 0.042911i
58500	0.091095 - 0.046616i
58750	0.089238 - 0.050078i
59000	0.08826 - 0.054086i
59250	0.086219 - 0.057284i
59500	0.0831 - 0.059713i
59750	0.080965 - 0.062577i
60000	0.078389 - 0.065776i
60250	0.076926 - 0.069265i
60500	0.073361 - 0.07134i
60750	0.06976 - 0.073256i
61000	0.067029 - 0.075763i
61250	0.06288 - 0.076279i
61500	0.059905 - 0.078637i
61750	0.056331 - 0.079854i
62000	0.052615 - 0.08102i
62250	0.048756 - 0.082115i
62500	0.045336 - 0.082808i
62750	0.041642 - 0.08352i
63000	0.037385 - 0.083186i
63250	0.034356 - 0.083354i
63500	0.030567 - 0.082633i

Table 3. (cont'd)

63750	0.027203 - 0.082739i
64000	0.023461 - 0.081817i
64250	0.019334 - 0.079919i
64500	0.016066 - 0.079679i
64750	0.01269 - 0.077491i
65000	0.0095075 - 0.07526i
65250	0.0065898 - 0.073838i
65500	0.0034983 - 0.071529i
65750	0.00060373 - 0.06918i
66000	-0.0019827 - 0.066805i
66250	-0.0046163 - 0.0644i
66500	-0.0068731 - 0.061275i
66750	-0.0089054 - 0.057525i
67000	-0.011019 - 0.055144i
67250	-0.012483 - 0.0516i
67500	-0.01423 - 0.048661i
67750	-0.015662 - 0.045228i
68000	-0.016733 - 0.041416i
68250	-0.017155 - 0.037469i
68500	-0.017732 - 0.033631i
68750	-0.018222 - 0.02997i
69000	-0.017866 - 0.026092i
69250	-0.017352 - 0.022209i
69500	-0.016457 - 0.018213i
69750	-0.015254 - 0.014628i
70000	-0.014089 - 0.01085i
70250	-0.01235 - 0.0071876i
70500	-0.010456 - 0.0037025i
70750	-0.0078292 - 0.00060243i
71000	-0.0055465 + 0.0025277i
71250	-0.0026578 + 0.0053308i
71500	0.00045509 + 0.0076601i
71750	0.003725 + 0.010179i
72000	0.007296 + 0.011906i
72250	0.010675 + 0.013713i
72500	0.01454 + 0.015004i
72750	0.018342 + 0.015888i
73000	0.02183 + 0.016272i
73250	0.025829 + 0.016966i
73500	0.029315 + 0.016993i
73750	0.033279 + 0.01652i
74000	0.036536 + 0.015811i
74250	0.039983 + 0.014869i
74500	0.043641 + 0.013593i
74750	0.046832 + 0.012286i
75000	0.049591 + 0.010541i
75250	0.052376 + 0.0086707i
75500	0.055152 + 0.0069673i
75750	0.056686 + 0.00476i
76000	0.059518 + 0.0023905i
76250	0.06166 +5.4687e-018i
76500	0.063061 - 0.002092i
76750	0.064384 - 0.004841i
77000	0.066443 - 0.0072181i
77250	0.0669 - 0.0097597i
77500	0.06809 - 0.012251i
77750	0.069273 - 0.014598i
78000	0.069636 - 0.016718i
78250	0.070651 - 0.019461i
78500	0.070854 - 0.021798i
78750	0.071725 - 0.024697i
79000	0.071735 - 0.02725i
79250	0.071819 - 0.029455i
79500	0.072845 - 0.031674i
79750	0.072705 - 0.034212i
80000	0.071848 - 0.035979i
80250	0.072465 - 0.038855i
80500	0.071351 - 0.040863i
80750	0.071664 - 0.044088i
81000	0.071301 - 0.046481i
81250	0.069721 - 0.048819i
81500	0.070283 - 0.05144i
81750	0.06882 - 0.053382i
82000	0.068082 - 0.055923i
82250	0.066393 - 0.057918i
82500	0.065182 - 0.060783i
82750	0.063021 - 0.063021i
83000	0.061717 - 0.065722i
83250	0.060432 - 0.068306i
83500	0.058379 - 0.070068i

Table 3. (cont'd)

83750	0.056274 - 0.071769i
84000	0.053992 - 0.073502i
84250	0.051263 - 0.075431i
84500	0.048599 - 0.077174i
84750	0.045876 - 0.078823i
85000	0.042957 - 0.080451i
85250	0.040123 - 0.081901i
85500	0.037244 - 0.082105i
85750	0.034211 - 0.083414i
86000	0.030775 - 0.083643i
86250	0.027203 - 0.082739i
86500	0.023861 - 0.083764i
86750	0.020447 - 0.082621i
87000	0.016969 - 0.083405i
87250	0.013728 - 0.082036i
87500	0.010732 - 0.081521i
87750	0.0074222 - 0.080009i
88000	0.0046569 - 0.078385i
88250	0.0014731 - 0.076722i
88500	-0.0015705 - 0.074973i
88750	-0.0042184 - 0.073161i
89000	-0.0071127 - 0.07126i
89250	-0.0093892 - 0.068543i
89500	-0.011376 - 0.065859i
89750	-0.013314 - 0.063178i
90000	-0.015301 - 0.060468i
90250	-0.016519 - 0.05723i
90500	-0.01805 - 0.053946i
90750	-0.019734 - 0.050614i
91000	-0.020121 - 0.047174i
91250	-0.020931 - 0.04428i
91500	-0.021135 - 0.041125i
91750	-0.021628 - 0.037917i
92000	-0.02086 - 0.033908i
92250	-0.020452 - 0.031018i
92500	-0.02005 - 0.027801i
92750	-0.019246 - 0.024634i
93000	-0.018516 - 0.021679i
93250	-0.017264 - 0.018644i
93500	-0.015703 - 0.015594i
93750	-0.014422 - 0.013123i
94000	-0.012806 - 0.010556i
94250	-0.010678 - 0.0079881i
94500	-0.0088314 - 0.0056262i
94750	-0.0066854 - 0.0032031i
95000	-0.0044535 - 0.0012434i
95250	-0.0018366 + 0.00077961i
95500	0.0004703 + 0.0025879i
95750	0.0030362 + 0.0041333i
96000	0.0060233 + 0.0055972i
96250	0.0088827 + 0.0070656i
96500	0.011762 + 0.0081139i
96750	0.014753 + 0.0091832i
97000	0.017943 + 0.0097423i
97250	0.02107 + 0.010276i
97500	0.023991 + 0.010782i
97750	0.027719 + 0.011087i
98000	0.030894 + 0.010819i
98250	0.033913 + 0.010433i
98500	0.037149 + 0.009954i
98750	0.040186 + 0.00913i
99000	0.043906 + 0.0082168i
99250	0.04626 + 0.0069136i
99500	0.049835 + 0.0053258i
99750	0.052917 + 0.0042576i
100000	0.056189 + 0.0022568i

Broadside Symbolic Manipulation

```
clear all
clc

% SYMBOLIC PARAMETERS

% p1 = rhof*(rho*g)^-1
% p2 = rhof^2*(rho*g)^-2

% g = (w/cf)
% w = 2*pi*f

% f = frequency of excitation (Hz)
% cf = wavespeed of fluid

% rhof = fluid density (kg/m3)
% rho = plate density (kg/m3)

% h = thickness of plate in meters

syms p1 p2 aR al h real;

% Complex Dilatational Wave Propagation Constant of the Plate

a = aR + i*al;

% Numerator for ER Model
ERNR = 2*p1*aR*sin(aR*h)*sinh(al*h) - 2*p1*al*cos(aR*h)*cosh(al*h)...
     + (1 + p2*aR^2 - p2*al^2)*sin(aR*h)*cosh(al*h)...
     - 2*p2*aR*al*cos(aR*h)*sinh(al*h);

ERNI = 2*p1*aR*cos(aR*h)*cosh(al*h) + 2*p1*al*sin(aR*h)*sinh(al*h)...
     + (1 + p2*aR^2 - p2*al^2)*cos(aR*h)*sinh(al*h)...
     + 2*p2*aR*al*sin(aR*h)*cosh(al*h);


% Denominator for ER Model
ERDR = 2*p2*aR*al*cos(aR*h)*sinh(al*h)...
     + (1 - p2*aR^2 + p2*al^2)*sin(aR*h)*cosh(al*h);

ERDI = -2*p2*aR*al*sin(aR*h)*cosh(al*h)...
     + (1 - p2*aR^2 + p2*al^2)*cos(aR*h)*sinh(al*h);

% Numerator for IL Model
ILNR = ERNR;
ILNI = ERNI;

% Denominator for IL Model
```

```
ILDR = -2*p1*aI;
ILDI = 2*p1*aR;

ERNUM = ERNR + i*ERNI;
ERDEN = ERDR + i*ERDI;
ILNUM = ILNR + i*ILNI;
ILDEN = ILDR + i*ILDI;



ER = ERDEN / ERNUM;
IL = ILDEN / ILNUM;

% Real and Imaginary Parts for ER and IL
ERr = real(ER);
ERi = imag(ER);
ILr = real(IL);
ILi = imag(IL);


% Newton Raphson Parameters for Iteration Matrix (M)
MER = [diff(ERr,aR),diff(ERr,aI);
       diff(ERi,aR),diff(ERi,aI)];

MIL = [diff(ILr,aR),diff(ILr,aI);
       diff(ILi,aR),diff(ILi,aI)];
```

Broadside Echo Reduction Inverse Method

```
clear all; clc

% Material Parameters
h   = 0.0254; % meters
rho  = 1185.7; % kg/m^3

% Fluid Parameters
rhof = 1000;   % kg/m^3
cf   = 1467.5; % m/s

% ATF Physical Test Data
load ER3140HF00
ER3140HF00 = conj(ER3140HF00);
NumFreqs = size(ER3140HF00,2);
FreqVec = FreqVecER3140HF00;
NUM = size(FreqVec,2);


% Initial Guess for alpha real/imag (m/s)
```

```
A(1,1) =120 ;
A(2,1) =  -12;

% Loop to Evaluate each Frequency
freq = [1:NUM];
for F = freq
  % Test Data for Current Frequency
  DATAr = real(ER3140HF00(F));
  DATAi = imag(ER3140HF00(F));

  % Model Parameters for Current Frequency
  w = 2*pi*FreqVec(F);
  g = (w/cf);
  p1 = rhof*(rho*g)^-1;
  p2 = rhof^2*(rho*g)^-2;

  % Iteration to Estimate Complex Wavespeed of Plate

  % Difference between Model and ATF Data
  di = 1;

  % Checking Difference between Model and ATF Data
  while (abs(di(1)) > .00000001 | abs(di(2)) > .000000001)

    % Current Alpha Parameters
    aR = A(1,1);
    aI = A(2,1);

    % Newton Raphson Partial Derivative Matrix
    %%M(1,1) = Obtain from "Broadside Echo Reduction Symbolic Manipulation"
    %%M(1,2) = Obtain from "Broadside Echo Reduction Symbolic Manipulation"
    M(2,1) = -M(1,2)
    M(2,2) = M(1,1)
    M = real(M);
    mi = inv(M);

    % Model Predicted ER Response
    ER = Obtain from "Broadside Echo Reduction Symbolic Manipulation"
    ERr = Obtain from "Broadside Echo Reduction Symbolic Manipulation"
    ERi = Obtain from "Broadside Echo Reduction Symbolic Manipulation"

    % Difference between Model and ATF Data (real and imag)
    d1 = ERr - DATAr;
    d2 = ERi - DATAi;
    di = [d1;d2];


% Updating Alpha Parameters
```

```
    b = A(:,1) - (mi*di) ./ 1;
    A(1,1) = b(1);
    A(2,1) = b(2);
  end

  % Stores Data for each Frequency in a Vector
  AR(F) = (A(1,1));
  AI(F) = (A(2,1));
  G(F) = g;
  W(F) = w;
  CD(F) = W(F) / (AR(F) + i*AI(F));
  CdR(F) = real(CD(F));
  CdI(F) = imag(CD(F));
  Freq(F) = FreqVec(F) / 1000;
  Echo(F) = ERr + ERi*i;
  eRr(F) = ERr;
  eRi(F) = ERi;
end


% Convert Real and Imag to Mag and Phase (Model Predicted and ATF Data)
dB = 20*log10(abs(Echo));
ph = 180/pi*angle(Echo);

DATAdB = 20*log10(abs(ER3140HF00));
DATAph = 180/pi * angle((ER3140HF00));
% Plot Echo Reduction Mag & Phase (Model & ATF Data)
figure(1)
grid on
hold on
subplot(2,1,1)
plot(Freq(1:2:NUM),dB(1:2:NUM),'o',Freq(1:2:NUM),DATAdB(1:2:NUM),'-',...
  'LineWidth',1,'MarkerSize',5)
grid off
hold on
title('Physical Testing of Braodside Echo Reduction 3140')
xlim([20 105])
legend('Inverse','Test Data',2)
xlabel('Frequency (kHz)')
ylabel('Magnitude (dB)')

subplot(2,1,2)
plot(Freq(1:2:NUM),ph(1:2:NUM),'o',Freq(1:2:NUM),DATAph(1:2:NUM),'-',...
  'LineWidth',1,'MarkerSize',5)
grid off
hold on
xlim([20 105])
ylim([-200 200])
```

```
legend('Inverse','Test Data',2)
xlabel('Frequency (kHz)')
ylabel('Phase Angle (degrees)')

% Plot Wavesppeed (real) and Loss Factor
figure(2)
subplot(2,1,1)
plot(Freq(1:4:NUM),CdR(1:4:NUM),'o',47,1194,'rs',71.25,1204,'rs',95.25,1210,'rs',...
   'LineWidth',2,'MarkerSize',5)
xlim([20 105])
ylim([1000 1500])
grid off
hold on
title('Broadside Complex Dilatational Wavespeed 3140')
legend('Inverse','Wavelength',2)
xlabel('Frequency (kHz)')
ylabel('"Real" Wavespeed (m/s)')

subplot(2,1,2)
plot(Freq(1:4:NUM),(CdI(1:4:NUM) ./ CdR(1:4:NUM)),'o', 'LineWidth',2,'MarkerSize',5)
xlim([20 105])
ylim([-.1 .25])
grid off
hold on
xlabel('Frequency (kHz)')
ylabel('Loss Factor (Imag / Real)')
```

Incident Angle Symbolic Manipulation

```
clear all
clc

% SYMBOLIC PARAMETERS

% p1 = rhof*(rho*g)^-1
% p2 = rhof^2*(rho*g)^-2
%  g = sqrt((w/cf)^2 - kx^2)
% w = 2*pi*f
% kx = (w/cf)*sin(theta)
% theta = 15*pi/180; %rad

% f = frequency of excitation (Hz)
% cf = wavespeed of fluid

% rhof = fluid density (kg/m3)
% rho = plate density (kg/m3)
% h = thickness of plate in meters
syms p1 p2 aR aI bR bI h kx real ;
```

```
% Complex Wave Propagation constants of the Plate
a = aR + i*aI;
b = bR + i*bI;

% Numerator for ER Model
ERNUM = 8*a*b*kx^2*(b^2 - kx^2)^2 * (1-cos(a*h)*cos(b*h)) + ...
    2*i*p1*a*(b^2 - kx^2)^2*(b^2 + kx^2)^2*cos(a*h)*sin(b*h) + ...
    8*i*p1*a^2*b*kx^2*(b^2 + kx^2)^2*sin(a*h)*cos(b*h) + ...
    ((b^2 - kx^2)^4 +16*a^2*b^2*kx^4 + p2*a^2*(b^2 + kx^2)^4)*sin(a*h)*sin(b*h);


% Denominator for ER Model
ERDEN = 8*a*b*kx^2*(b^2 - kx^2)^2 * (1-cos(a*h)*cos(b*h)) + ...
    ((b^2 - kx^2)^4 +16*a^2*b^2*kx^4-p2*a^2*(b^2 + kx^2)^4)*sin(a*h)*sin(b*h);

% Numerator for IL Model
ILNUM = ERNUM;

% Denominator for IL Model
ILDEN = 8*i*p1*a^2*b*kx^2*(b^2 + kx^2)^2*sin(a*h) + ...
      2*i*p1*a*(b^2 - kx^2)^2*(b^2 + kx^2)^2*sin(b*h);



ER = ERDEN / ERNUM;
IL = ILDEN / ILNUM;

% Real and Imaginary Parts for ER and IL
ERr = real(ER);
ERi = imag(ER);
ILr = real(IL);
ILi = imag(IL);


% Newton Raphson Parameters for Iteration
M = [diff(ERr,aR),diff(ERr,aI),diff(ERr,bR),diff(ERr,bI);
    diff(ERi,aR),diff(ERi,aI),diff(ERi,bR),diff(ERi,bI);
    diff(ILr,aR),diff(ILr,aI),diff(ILr,bR),diff(ILr,bI);
    diff(ILi,aR),diff(ILi,aI),diff(ILi,bR),diff(ILi,bI);];
```

Incident Angle Inverse Method

```
clear all; clc

% Material Parameters
h   = 0.0254;  % meters
rho  = 1185.7;  % kg/m^3

% Fluid Parameters
rhof = 1000;   % kg/m^3
cf   = 1467.5;  % m/s
theta = 10*pi/180; %rad

% ATF Physical Test Data
load ER3140HF10
load IL314HF10
ER3140HF00 = (ER3140HF10);
IL3140HF00 = (IL3140HF10);

NUM = size(ER3140HF00,2);

FreqVec = FreqVecER3140HF10;

% Initial Guess (m/s)
A(1,1) = 216.9 ;
A(2,1) =  -66.8;
A(3,1) = 247 ;
A(4,1) =  -60.4;

% Loop to Evaluate each Frequency
for F = 1:NUM

   ERDATAr = real(ER3140HF00(F));
   ERDATAi = imag(ER3140HF00(F));
   ILDATAr = real(IL3140HF00(F));
   ILDATAi = imag(IL3140HF00(F));

   w = 2*pi*FreqVec(F);
   kx = (w/cf)*sin(theta);
   g = sqrt((w/cf)^2 - kx^2);


   p1 = rhof*(rho*g)^-1;
   p2 = rhof^2*(rho*g)^-2;

   e = .0001;
   di = 1;


%Iteration to Estimate Complex Wave Speed of Plate
```

```
while (abs(di(1)) > e | abs(di(2)) > e | abs(di(3)) > e | abs(di(4)) > e)
  di;
  aR = A(1,1);
  aI = A(2,1);
  bR = A(3,1);
  bI = A(4,1);

 M(1,1) = Obtain from "Incident Angle Symbolic Manipulation"
  M(1,2) = Obtain from "Incident Angle Symbolic Manipulation"
  M(1,3) = Obtain from "Incident Angle Symbolic Manipulation"
  M(1,4) = Obtain from "Incident Angle Symbolic Manipulation"
  M(2,1) = Obtain from "Incident Angle Symbolic Manipulation"
  M(2,2) = Obtain from "Incident Angle Symbolic Manipulation"
  M(2,3) = Obtain from "Incident Angle Symbolic Manipulation"
  M(2,4) = Obtain from "Incident Angle Symbolic Manipulation"
  M(3,1) = Obtain from "Incident Angle Symbolic Manipulation"
  M(3,2) = Obtain from "Incident Angle Symbolic Manipulation"
  M(3,3) = Obtain from "Incident Angle Symbolic Manipulation"
  M(3,4) = Obtain from "Incident Angle Symbolic Manipulation"
  M(4,1) = Obtain from "Incident Angle Symbolic Manipulation"
  M(4,2) = Obtain from "Incident Angle Symbolic Manipulation"
  M(4,3) = Obtain from "Incident Angle Symbolic Manipulation"
  M(4,4) = Obtain from "Incident Angle Symbolic Manipulation"


  M = real(M);
  mi = inv(M);

  ER = Obtain from "Incident Angle Symbolic Manipulation"
  Err = Obtain from "Incident Angle Symbolic Manipulation"
  ERi = Obtain from "Incident Angle Symbolic Manipulation"
  IL = Obtain from "Incident Angle Symbolic Manipulation"
  ILr = Obtain from "Incident Angle Symbolic Manipulation"
  ILi = Obtain from "Incident Angle Symbolic Manipulation"

  d1 = ERr - ERDATAr;
  d2 = ERi - ERDATAi;
  d3 = ILr - ILDATAr;
  d4 = ILi - ILDATAi;
  di = [d1;d2;d3;d4];

  updt = A(:,1) - (mi*di);
  A(1,1) = updt(1);
  A(2,1) = updt(2);
  A(3,1) = updt(3);
  A(4,1) = updt(4);
end
```

```
  AR(F) = (A(1,1));
  AI(F) = (A(2,1));
  BR(F) = (A(3,1));
  BI(F) = (A(4,1));
  G(F) = g;
  W(F) = w;
  KX(F)=kx;
  CD(F) = sqrt((W(F)^2) / ((AR(F) + i*AI(F))^2+KX(F)^2));
  CdR(F) = real(CD(F));
  CdI(F) = imag(CD(F));
  CS(F) = sqrt((W(F)^2) / ((BR(F) + i*BI(F))^2+KX(F)^2));
  CsR(F) = real(CS(F));
  CsI(F) = imag(CS(F));
  Freq(F) = FreqVec(F) / 1000;
  Echo(F) = ERr + ERi*i;
  Loss(F) = ILr + ILi*i;
  eRr(F) = ERr;
  eRi(F) = ERi;
  iLr(F) = ILr;
  iLi(F) = ILi;
end


ERdB = 20*log10(abs(Echo));
ERph = 180/pi*angle(Echo);
ILdB = 20*log10(abs(Loss));
ILph = 180/pi*angle(Loss);

ERDATAdB = 20*log10(abs(ER3140HF00));
ERDATAph = 180/pi * angle((ER3140HF00));
ILDATAdB = 20*log10(abs(IL3140HF00));
ILDATAph = 180/pi * angle((IL3140HF00));
%
% Plot Echo Reduction Mag & Phase (Model & Experimental)
figure(1)
grid on
hold on
subplot(2,1,1)
plot(Freq(1:2:NUM),ERdB(1:2:NUM),'x',Freq(1:2:NUM),ERDATAdB(1:2:NUM),'o',...
  'LineWidth',1,'MarkerSize',3)
grid on
hold on
title('Numerical Example Echo Reduction')
xlim([20 100])
legend('Inverse','Original',2)
xlabel('Frequency (kHz)')
ylabel('Magnitude (dB)')
```

```
subplot(2,1,2)
plot(Freq(1:2:NUM),ERph(1:2:NUM),'x',Freq(1:2:NUM),ERDATAph(1:2:NUM),'o',...
   'LineWidth',1,'MarkerSize',3)
grid on
hold on
xlim([20 100])
ylim([-200 200])
legend('Inverse','Original',2)
xlabel('Frequency (kHz)')
ylabel('Phase Angle (degrees)')

% Plot Insertion Loss Mag & Phase (Model & Experimental)
figure(2)
grid on
hold on
subplot(2,1,1)
plot(Freq(1:2:NUM),ILdB(1:2:NUM),'x',Freq(1:2:NUM),ILDATAdB(1:2:NUM),'o',...
   'LineWidth',1,'MarkerSize',3)
grid on
hold on
title('Numerical Example Insertion Loss')
xlim([20 100])
legend('Inverse','Original',2)
xlabel('Frequency (kHz)')
ylabel('Magnitude (dB)')

subplot(2,1,2)
plot(Freq(1:2:NUM),ILph(1:2:NUM),'x',Freq(1:2:NUM),ILDATAph(1:2:NUM),'o',...
   'LineWidth',1,'MarkerSize',3)
grid on
hold on
xlim([20 100])
ylim([-200 200])
legend('Inverse','Original',2)
xlabel('Frequency (kHz)')
ylabel('Phase Angle (degrees)')


% Plot Wavespeed (real) and Loss Factor
figure(3)
subplot(2,1,1)
plot(Freq(1:4:NUM),CdR(1:4:NUM),'x',Freq(1:4:NUM),CsR(1:4:NUM),'x',...
   'LineWidth',1,'MarkerSize',3)
title('Calculated Complex Wavespeeds')
legend('Inverse','Original',2)
xlabel('Frequency (kHz)')
ylabel('"Real" Wavespeed (m/s)')
% xlim([20 100])
```

```
% ylim([0 1600])

subplot(2,1,2)
plot(Freq(1:4:NUM),Cdl(1:4:NUM),'x',Freq(1:4:NUM),Csl(1:4:NUM),'x',...
   'LineWidth',1,'MarkerSize',3)
xlabel('Frequency (kHz)')
ylabel('"Imag" Wavespeed (m/s)')
% xlim([20 100])
% ylim([0 50])
```

REFERENCES

REFERENCES

1. Acoustic Test Facility, (2004). Naval Undersea Warfare Center Division Newport RI. http://www.npt.nuwc.navy.mil/ATF8211/index.html

2. Goldberg, Jack and Potter, Merle, C., (1995). Mathematical Methods. Okemos, MI: Great Lakes Press.

3. Hull, Andrew, J., (2005). "Analysis of a Fluid-Loaded Thick Plate", *Journal of Sound and Vibration*, Vol. 279, pp. 497-507.

4. Hull, Andrew, J., (2003). "A Method for Estimating the Mechanical Properties of a Solid Material Subjected to Significant Compressional Forces", *Naval Undersea Warfare Center Technical Report 11,412*, Newport, RI.

5. Milklowitz, Julius, (1984). The theory of elastic waves and waveguides. New York: North – Holland.

6. Piquette, Jean, C., (2003). "Phase change measurement, and speed of sound attenuation determination, from underwater acoustic panel tests" *The Journal of the Acoustical Society of America,* Vol. 113, pp. 1518-1525.

7. Piquette, Jean, C., (2004). "Shear material property determination from underwater acoustic panel tests" *The Journal of the Acoustical Society of America,* Vol. 115, pp. 2110-2121.

8. "Sonar Propagation, (1998)."Introduction to Naval Weapons Engineering. Federation of American Scientists. http://www.fas.org/man/dod-101/navy/docs/es310/SNR_PROP/snr_prop.htm